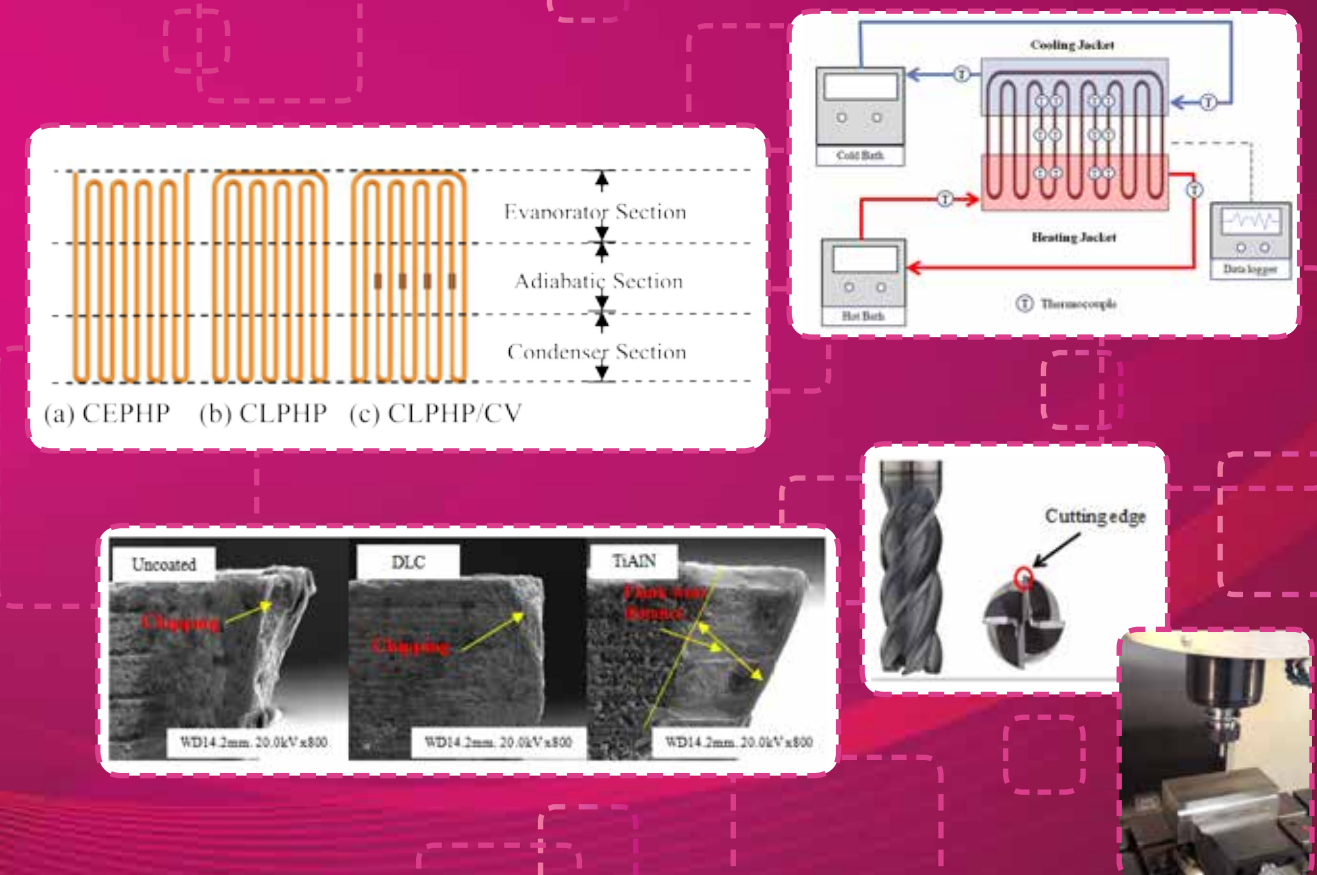




SCIENCE and TECHNOLOGY

MAHASARAKHAM UNIVERSITY

www.journal.msu.ac.th



Aim and Scope:

The MSU Journal of Science and Technology is published quarterly and dedicated to the promotion and dissemination of scientific knowledge in the disciplines of Bioscience, Physical Science and Engineering Articles and research papers to be published in the Journal of Science and Technology Maharakham University will be subject to verification of academic luminaries both from within and outside the University to assure journal quality standards.

Ownership

Maharakham University
Editorial Office
Division of Research Support and Development,
Khamriang Sub-district, Kantharawichai District,
Maha Sarakham Province 44150
Tel & Fax: 0 4375 4238 ext. 1754

Advisors

President of Maharakham University
Professor Dr. Reon Somanan
Professor Dr. Visut Baimai
Professor Dr. Vichai Boonsaeng

Editor-in-Chief

Professor Dr. Preecha Prathepha
Maharakham University

Assistant Editors

Associate Professor Dr. Worapol Aengwanich
Maharakham University

Editorial Board

Professor Dr. Thaweesakdi Boonkerd
Chulalongkorn University
Professor Dr. La-orsri Sanoamuang
Khon Kaen University
Professor Dr. Supanee Promthet
Khon Kaen University
Professor Dr. Pranee Anprung
Chulalongkorn University
Professor Dr. Sampan Ritthidech
Maharakham University
Associate Professor Dr. Natchaporn Pichainanong
Maharakham University
Associate Professor Dr. Sunan Saikrasun
Maharakham University
Associate Professor Dr. Pairoi Pramual
Maharakham University
Associate Professor Dr. Sirithon Siriamornpun
Maharakham University
Associate Professor Dr. Ampon Dhamacharoen
Burapha University
Associate Professor Dr. Suwanna Boonyaleepun
Khon Kaen University
Associate Professor Dr. Kwanjai Kanokmedhakul
Khon Kaen University
Associate Professor Dr. Chantana Aromdee
Khon Kaen University

Associate Professor Dr. Niwat Sonoamuang
Khon Kaen University
Associate Professor Dr. Boonchong Chawsithiwong
National Institute of Development Administration
Associate Professor Dr. Porntep Tanonkeo
Khon Kaen University
Associate Professor Dr. Narumon Sangpradub
Khon Kaen University
Associate Professor Dr. Terdsak Khammeng
Khon Kaen University
Associate Professor Dr. Yuen Poovarawan
Kasetsart University
Associate Professor Dr. Vallaya Sutthikhum
Maharakham University
Assistant Professor Dr. Chawalit Boonpok
Maharakham University
Assistant Professor Dr. Buavaroon Srichaikul
Maharakham University
Assistant Professor Dr. Bungon Kumphon
Maharakham University
Assistant Professor Dr. Sirikasem Sirilak
Naresuan University
Assistant Professor Dr. Supattra Porasuphatana
Khon Kaen University
Assistant Professor Dr. Napparat Buddhakala
Rajamangala University of Technology Thanyaburi
Assistant Professor Dr. Anucha Pranchana
Ubon Ratchathani Rajabhat University
Dr. Seckson Sukhasena
Naresuan University
Dr. Rakjinda Wattanalai
Siam University
Dr. Somnuk Puangpronpitag
Maharakham University
Paul Duffer
Maharakham University
Chaweewan Akkasesthang
Maharakham University

Secretary

Pichaya Chowtivanakul

Assistant secretary

Jirarat Puseerit
Phakwilai Rungwisai

Six issues per year

Number 1 January - February
Number 2 March - April
Number 3 May - June
Number 4 July - August
Number 5 September - October
Number 6 November - December

The articles and opinions expressed in the Journal of Science and Technology are those of the authors. Readers are invited to make argumentative comments to any article appearing in the journal. All articles in the Journal of Science and Technology are protected by the copyright laws of Thailand, and publishing or dissemination of any article requires written permission of approval from the editorial board.

Editor-in-Chief's message

As Editor-in-Chief, I would like to welcome again all of you who took the time to read our very first English language issue of the Mahasarakham University Journal of Science and Technology some ten years ago. To start with, let me share with you that our journal has enjoyed positive developments over those past ten years including being accepted as a quality journal by the TCI (Thailand Citation Index). I believe these positive developments will continue to accelerate the journal's ranking among the community of journals.

It has been a pleasure to work alongside other universities in Thailand and overseas on academic projects where scholars carried out research and produced quality research papers which were submitted and published in our journal.

In Thailand, recognized as a prominent agricultural sector, Thai researchers are striving to develop advanced tools to strengthen the agricultural community's position as a world class producer. The tools are varied and destined to become an important part of Thailand's agricultural sector. This volume of our journal has a remarkable collection of other papers in a variety of fields that may ultimately support the agricultural community. It gives me great pleasure to know that it will become a valuable addition to the reader's library.

Prof. Preecha Prathepha. Ph.D

Editor-in-Chief

Cover photo explanation : Effect of Working fluids on Thermal Performance of Vertical Closed-loop Pulsating Heat pipe, Performance of Carbide Cutting Tool Coated DLC and Tialnto Wear Protection on Cutting Edge

Cover photo : Piyapong Suvunnajun *et al.*, 2559, 332-337., Paramet Baowan 2559, 338-341

CONTENTS

Original Articles

- Ultraviolet Radiation Reduces Microbial Contaminants while Increasing Antioxidant Activities in Black Jasmine Rice Pericarp Beverage** 261
Kanokwan Tandee, Suthaya Phimphilai, Somkiat Jaturonglumlert,
Aphiwat Teerawutgulrag, Jatuphon Varith, Surat Nuglor, Kajorndej Phimphilai
- Energy Saving Potential in a Fresh Market in Nakhon Sawan Province, Thailand** 267
Kittisak Khuwaranyu, Pongsiri Jaruyanon
- Current-mode Sinusoidal Oscillator Based-on CCCCTAs and Grounded Capacitors with Amplitude Controllable** 275
Phanida Srakaew, Atthapon Muenthom, Suphaphorn Panikhom, Adirek Jantakun
- The Application of the Environmental Adaptation Concept to A Collector Road in KKU, Thailand** 280
Pongrid Klungboonkrong, Monsicha Bejrananda, Natthapoj Faiboun
- Static Pile Load Test in Rajamangala University of Technology Khon Kaen Campus** 289
Pongsagorn Pongchompu, Sorasak Seawsirikul, Pongsagorn Pongchompu
- Experimental Investigation of Closed Loop Oscillating Heat Pipe at Startup Condition** 293
Surain Promdan, Phrut Sakulchangsajatai, Niti Kammuang-lue, Pradit Terdtoon
- Thermal Performance Enhancement in a Heat Exchanger Square-Duct With V-Shaped Fins Vortex Generator** 299
Supattarachai Suwannapan, Suriya Chokphoemphun, Panuwat Hoonpong, Pongjet Promvonge
- Texture of Cooked Selected KDML 105 Rice Mutants and Its Related Variables** 305
Wiwat Wangcharoen, Chaveewon Phanchaisri, Wichitra Daengprok, Rimruthai Phuttawong,
Tawan Hang Soongnern, Songchao Insomphun, Boonrak Phanchaisri
- Heat Transfer Correlations for Small Closed End Heat Pipe with Special Vapor Chamber** 314
Duangkamon Hemathurin, Narong Srihajong, Paisan Kumthong, Juthamat Silon
- Experimental Investigations on Thermal Performance of Small Closed End Heat Pipes with Special Vapor Chamber** 321
Kittipong Saehang, Narong Srihajong

CONTENTS

Original Articles

- Study of Heat Transfer Characteristics of Bent Heat Pipe with Multiple Heat Sources by Using Finite Element Method** 326
Nampon Sangpab, Phrut Sakulchangsattajai, Niti Kammuang-lue, Pradit Terdtoon
- Effect of Working fluids on Thermal Performance of Vertical Closed-loop Pulsating Heat pipe** 332
Piyapong Suvunnajun, Niti Kammuang-lue, Phrut Sakulchangsattajai, Pradit Terdtoon
- Performance of Carbide Cutting Tool Coated DLC and Tialnto Wear Protection on Cutting Edge** 338
Paramet Baowan
- FEM Study of Velocity Profile of Flattening Heat Pipe with Multiple Heat Sources** 342
Sophon Sinsang, Niti Kammuang-lue, Phrut Sakulchangsattajai, Pradit Terdtoon
- Snubber Circuit Used as the Temperature Dissipation of Mosfet for Electric Car Drive System** 350
Sakrawee Reweekul
- Design and Development of a Small 3D Scanner** 354
Sivapong Phetsong
- The Continuous Process of Biodiesel Production with Water Heater Assist** 362
Thibordin Sansawang, Chanjira Chimmanee, Trakan Butsing
- Heat Transmission of Double-Pane Windows with Horizontal Slats in Thailand** 368
Vichuda Mettanant, Pipat Chaiwiwatworakul

Ultraviolet Radiation Reduces Microbial Contaminants while Increasing Antioxidant Activities in Black Jasmine Rice Pericarp Beverage

Kanokwan Tandee^{1*}, Suthaya Phimphilai¹, Somkiat Jaturonglumlert¹,
Aphiwat Teerawutgulrag², Jatuphon Varith¹, Surat Nuglor¹, and Kajornraj Phimphilai³

Received: 12 June 2015; Accepted: 13 July 2015

Abstract

Black jasmine rice (*Oryza sativa* var. Hom Nil) is a great source of antioxidants mainly present in its pericarp, and the beverage extracted from this part is considered a functional food. However, production of beverage normally involves a heat treatment for safety purpose that possibly destroys some antioxidants, Ultraviolet (UV) radiation is thus proposed as an alternative process to reduce microbial contaminants and its effect on antioxidant activities is also determined. UV treatment through 6×6 W lamps at the lowest flow rate of 0.4 L/min could decrease ($p>0.05$) the total plate count as well as yeast and mold count in the beverage for 0.39 and 0.75 log CFU/mL, respectively. Antioxidant activities, analyzed by ABTS and FRAP assays, in the black jasmine rice pericarp beverage, were significantly ($p<0.05$) increased after UV treatment at a flow rate of 0.4, 0.7, or 1.0 L/min. Results suggest the multiple times of UV radiation should be used to effectively inhibit the microbial contaminants while antioxidants should be re-evaluated to ensure their stability. Black jasmine rice pericarp beverage, which is disinfected by UV treatment to meet a microbiological standard, could be a functional product without any health risk.

Keywords: ultraviolet radiation, rice pericarp beverage, microbial contaminant, antioxidant activity

Introduction

Black rice contains higher contents of protein, total essential amino acids, vitamin B1, and minerals when compared to common rice. Its pericarp is also abundant in anthocyanins, e.g. cyanidin 3-glucoside and peonidin 3-glucoside, as well as antioxidants, e.g. γ -tocotrienol, α -tocopherol, β -, γ -, δ -tocopherols and α -, δ -tocotrienols^{1,2}. Functional beverage produced from black jasmine rice, which is high in these compounds, could promote consumer health by inhibiting inflammation, allergy, cancer, and insulin resistance³⁻⁶. While several methods were used to extract natural compounds from plant materials⁷, optimal conditions of ultraviolet (UV) radiation and ultrasonication (US) were suggested for production of red rice extract drink, resulting in optimal antioxidant

activities and significantly lower microbial counts⁸. Microorganisms remaining in this non-thermally processed product might be, nevertheless, over a limit of microbiological standard that is less than 100 CFU/mL of *Bacillus cereus*, 100 CFU/mL of *Clostridium perfringens*, 100 CFU/mL of yeast and mold, 2.2 MPN/100mL of coliform bacteria, as well as an absence of *Salmonella*, *Staphylococcus aureus*, *Listeria monocytogenes*, and *Escherichia coli*^{9,10}. Low-acid canned foods were thus commonly heat-treated for safety purposes but possibly lost their nutritional value as well. UV radiation that has a germicidal activity by creating a thymine dimer in DNA¹¹ is, therefore, proposed as a non-thermal treatment after extraction of functional ingredients from black jasmine rice pericarp.

¹ Faculty of Engineering and Agro-Industry, Maejo University, Chiang Mai, 50290 Thailand

² Faculty of Science, Chiang Mai University, Chiang Mai, 50200 Thailand

³ Faculty of Engineering, Chiang Mai University, Chiang Mai, 50200 Thailand

* Email: ktandee@gmail.com

Previous studies indicated that UV effectively reduced the microbial contaminants in grape juice, wine, coconut beverage, orange juice, apple juice, guava-and-pineapple juice, mango nectar, strawberry nectar, and tropical juice¹²⁻¹⁵. The objective of this study was to evaluate the effectiveness of UV radiation in disinfecting the black jasmine rice pericarp beverage. Additionally, the stability of antioxidants present in this beverage was ascertained for the side effect of UV treatment.

Materials and Methods

1. Raw Material

Organic black jasmine rice (*Oryza sativa* var. Hom Nil) was purchased from AGRI CMU SHOP, Chiang Mai University after harvest in Phrao, Chiang Mai.

2. Preparation of Black Jasmine Rice Pericarp Beverage

Beverage was extracted from black jasmine rice pericarp as previously described⁸. Briefly, 2kg of rice was washed twice in a tap water and then spread to a thin layer before radiated with 4×15 W UV lamps (Sylvania, Japan) for 30 min. After that, 8L of commercial drinking water (Singha, Thailand) was added into an ultrasonicator model code W-113SANPA (Micromechatronics, USA) filled with the radiated rice. US condition was set at 28 kHz, 50°C for 60 min and the resulting extract was treated in a customized UV disinfection system equipped with 6×6 W lamps at 4 different conditions as described in (Table 1).

Table 1 Conditions of UV treatment used in this study.

Flow rate (L/min)	Contact time (min)
0.4	4.50
0.7	2.57
1.0	1.80
1.5	1.20

3. Microbiological Analyses

1 mL of sample was serially diluted in 9 mL of 0.1% peptone water to the 10⁻⁴ dilution. Bacterial number was determined using a pour plate technique¹⁶.

1 mL of each dilution was inoculated on Petri dish before approximately 15 mL of 45°C plate count agar (Himedia) was poured and mixed thoroughly. All dilution was plated in duplicate. Plates were incubated at 35°C for 48 h before colonies were enumerated.

Numbers of yeast and mold were evaluated using a spread plate technique¹⁶. 0.1 mL of each dilution was spread on potato dextrose agar (Himedia), which pH adjusted to 3.5 using 10% tartaric acid (Ajax Finechem, Australia), and all dilution was plated in duplicate. Plates were incubated at 25°C for 5 days before colonies were enumerated.

Dilution that showed 30-300 colonies of bacteria per plate or 10-150 colonies of yeast and mold per plate was selected for calculating a microbial count in a log scale per 1 mL of rice drink (log CFU/mL).

4. Antioxidant activities

4.1 ABTS^{•+} radical cation decolorization assay

The assay protocol was previously described by Re and colleagues¹⁷. ABTS radical cation (ABTS^{•+}) was prepared by mixing 7 mM ABTS [2,2'-azinobis(3-ethylbenzothiazoline-6-sulfonic acid); (Sigma-Aldrich, Germany)] with 2.45 mM K₂S₂O₈ (Sigma-Aldrich) at an equal volume and allowing the mixture to stand in the dark at room temperature for 12-16 h. This stock solution could be stable for 2 days and used to prepare the working solution by diluting with water (Merck, Germany) to an absorbance of 0.7-0.9 at 734 nm. To perform the ABTS^{•+} assay, 20 µL of sample was mixed with 80 µL of water and 2 µL of ABTS^{•+} working solution for 3 min and an absorbance at 734 was read using Trolox (6-hydroxy-2,5,7,8-tetramethylchroman-2-carboxylic acid; Sigma-Aldrich) as a standard. Each sample was analyzed in duplicate. Concentration of antioxidants was obtained by fitting a change in absorbance of samples to a standard curve of Trolox.

4.2 Ferric reducing ability power (FRAP) assay

The assay was slightly modified from a protocol developed by Benzie and Strain¹⁸. FRAP working reagent was freshly prepared before use by mixing 25

mL of 300 mM acetate buffer [$3.1 \text{ g C}_2\text{H}_3\text{NaO}_2 \times 3\text{H}_2\text{O}$ (Fisher Scientific, UK) and $16 \text{ mL of C}_2\text{H}_4\text{O}_2$ (Merck) per 1 L of buffer], $2.5 \text{ mL of } 10 \text{ mM TPTZ solution [2,4,6-tripyridyl-s-triazine (Sigma-Aldrich) in } 40 \text{ mM HCl (Merck)], and } 2.5 \text{ mL of } 20 \text{ mM FeCl}_3 \times 6\text{H}_2\text{O (Merck). To perform the FRAP assay, } 20 \text{ }\mu\text{L of sample was mixed with } 60 \text{ }\mu\text{L of water and } 600 \text{ }\mu\text{L of FRAP working reagent for } 4 \text{ min and an absorbance at } 593 \text{ was read using } \text{FeSO}_4 \text{ (Merck) as a standard. Each sample was analyzed in duplicate. Concentration of antioxidants was obtained by fitting a change in absorbance of samples to a standard curve of } \text{FeSO}_4$.

4.3 Total polyphenol content (TPC) assay

The assay protocol was previously described by Pinsirodom and Changnoi¹⁹. $0.5 \text{ mL of sample was mixed with } 9.5 \text{ mL of water and } 0.5 \text{ mL of Folin-Ciocalteu's reagent (Merck) for } 5 \text{ min and } 2 \text{ mL of } 10\% \text{ Na}_2\text{CO}_3 \text{ (Ajax Finechem) was then added. The solution was allowed to stand at room temperature for } 10 \text{ min before an absorbance at } 730 \text{ was read using gallic acid (Sigma-Aldrich) as a standard. Each sample was analyzed in duplicate. Concentration of antioxidants was obtained by fitting a change in absorbance of samples to a standard curve of gallic acid.}$

4. Statistical analyses

To determine the statistical differences among UV conditions, Analysis of Variance (ANOVA) followed by Least Significant Difference (LSD) tests were used at 95% confidence (SPSS version 11.5.0; IBM, USA).

Results and Discussions

1. UV Treatment Decreases Microbial Counts in the Black Jasmine Rice Pericarp Beverage.

Reductions of microbial contaminants in the black jasmine rice pericarp beverage after UV treatment at 4 different conditions are shown in (Figure 1) Values were in a range of -0.10 to -0.75 log CFU/mL , which was lower than previous studies^{12,15,20}. This is possibly due to the lower dosage used in this study since a germicidal effect of UV is dose and time dependent. A lower flow rate generally resulted in a greater microbial reduction although abnormality was observed at a flow rate of 0.7

L/min after a different batch of black jasmine rice was used.

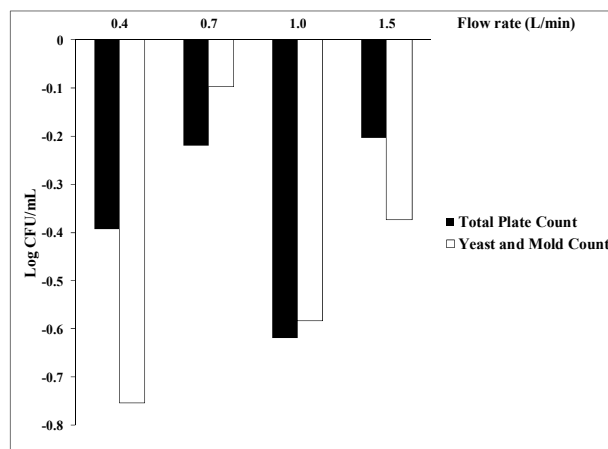


Figure 1 Reduction of microbial contaminants in the black jasmine rice pericarp beverage after UV treatment at 4 different conditions

Mesophilic bacteria after UV treatment was lowered in a range of -0.20 to -0.62 log CFU/mL and UV treatment at a flow rate of 0.4 L/min showed the maximum reduction, although this condition did not result in a significant number ($p > 0.05$) when compared to a control beverage. Meanwhile, decrease in yeast and mold after UV treatment was found in a range of -0.10 to -0.75 log CFU/mL . Yeast and mold present in the black jasmine rice pericarp beverage were also insignificantly ($p > 0.05$) decreased after UV treatment at a flow rate of 0.4 L/min . Since microbial contaminants remained in the beverage treated at this condition were 4.51 log CFU/mL for mesophilic bacteria and 2.06 log CFU/mL for yeast and mold, multiple times of UV radiation are recommended for the effective disinfection of the black jasmine rice pericarp beverage.

2. UV Treatment Increases Antioxidant activities in the Black Jasmine Rice Pericarp Beverage.

Changes in antioxidant activities, which were analyzed by ABTS⁺, FRAP, and TPC assays, in the black jasmine rice pericarp beverage after UV treatment at 4 different conditions were shown in (Figure 2) Values were in a range of -776.31 to 719.80 , which was higher than previous studies²¹⁻²². It is possibly due to the different variety of rice used.

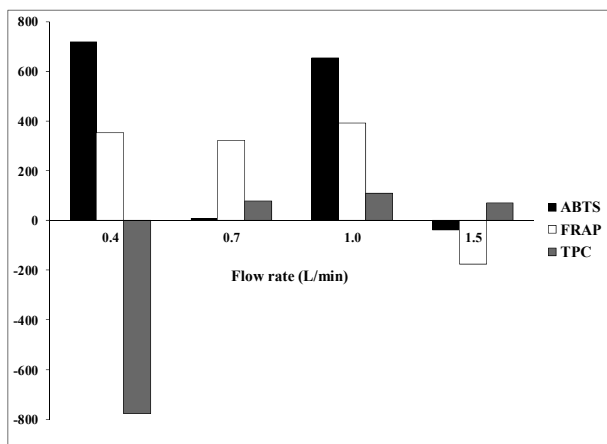


Figure 2 Changes in antioxidant activities, which were analyzed by ABTS⁺, FRAP, and TPC assays, in the black jasmine rice pericarp beverage after UV treatment at 4 different conditions

ABTS⁺ and FRAP assays, which are based on a single electron transfer as mechanism of free radical quenching reaction²³, resulted in a similar trend of antioxidant activities. More specifically, the activities were promoted by a lower flow rate of UV treatment but inhibited at a higher flow rate. However, contradiction was observed in a TPC assay where other phenolic compounds, such as flavonoids, lignins, and tannins, were analyzed as well²³.

Antioxidant activities, which were measured by ABTS⁺ assay, were found in a range of -38.21 to 719.80 mg Trolox equivalent/mL. Increase in these activities was significantly ($p < 0.01$) higher at a flow rate of 0.4, 1.0, and 0.7 L/min, respectively. Using FRAP assay, antioxidant activities were found in a range of -175.67 to 391.87 mg FeSO₄/50mL and significantly ($p < 0.01$) higher at a flow rate of 1.0, 0.4, and 0.7 L/min, respectively. UV treatment might induce enzymes involved in the antioxidant synthesis after exposure to oxidative stress as described in previous studies, resulting in a high level of antioxidant activities²⁴⁻²⁵.

Antioxidants as determined by TPC assay were found in a range of -776.31 to 109.17 mg gallic acid equivalent/50mL. Increase in antioxidants in the black jasmine rice pericarp beverage was significantly ($p < 0.01$) higher at a flow rate of 1.0, 0.7, and 1.5 L/min, respectively. The lower content of total polyphenol at a flow rate of 0.4

L/min is possibly due to the degradation of some compounds, which are not involved in any antioxidant activities, after a long period of UV exposure. Overall, UV treatment at the lowest flow rate of 0.4 L/min is suitable for the black jasmine rice pericarp beverage since microbial contaminants were maximally reduced and antioxidant activities, which were measured by ABTS⁺ and FRAP assays, were maximally increased when compared to a control beverage.

Conclusion

UV radiation could be a promising alternative to heat treatment of black jasmine rice pericarp beverage due to the reduction of microbial contaminants and the increase of antioxidant activities. The lowest flow rate of 0.4 L/min was recommended as a condition of UV disinfection system, although multiple passes are necessary to ensure the microbiological safety of final product.

Acknowledgement

This research was financially supported by the Agricultural Research Development Agency (Thailand). We greatly appreciate the technical assistance from Miss Sookhathai-Yaibua and Miss Prapatsara Supamongkol, undergraduate students in Food Science and Technology Program at Maejo University.

References

- [1] Sompong, R., Siebenhandl-Ehn, S., Linsberger-Martin, G., and Berghofer, E. Physicochemical and Antioxidative Properties of Red and Black Rice Varieties from Thailand, China and Sri Lanka, *Food Chem.*, 2011; 124(1): 132-140.
- [2] Yoshida, H., Tomiyama, Y., and Mizushima, Y. Lipid Components, Fatty Acids and Triacylglycerol Molecular Species of Black and Red Rices, *Food Chem.*, 2010; 123(2): 210-215.
- [3] Chen, M., Choi, S., Kozukue, N., Kim, H., and Friedman, M. Growth-Inhibitory Effects of Pigmented Rice Bran Extracts and Three Red Bran Fractions against Human Cancer Cells: Relationships with Composition and Antioxidative Activities, *J. Agr. Food Chem.*, 2012; 60(36): 9151-9161.

- [4] Fan, J., Choi, K., and Han, G. Inhibitory Effects of Water Extracts of Fermented Rice Bran on Allergic Response, *Food Sci. Biotechnol.*, 2010; 6: 1573-1578.
- [5] Guo, H., Ling, W., Wang, Q., Liu, C., Hu, Y., and Xia, M. Cyanidin 3-Glucoside Protects 3T3-L1 Adipocytes against H₂O₂ - or TNF- α -Induced Insulin Resistance by Inhibiting c-Jun NH2-Terminal Kinase Activation, *Biochem. Pharmacol.*, 2008; 6: 1393-1401.
- [6] Min, S., Ryu, S., Kim, D. Anti-Inflammatory Effects of Black Rice, Cyanidin-3-O- β -d-Glycoside, and Its Metabolites, Cyanidin and Protocatechuic Acid, *Int. Immunopharmacol.*, 2010; 10(8): 959-966.
- [7] Oroian, M. and Escriche, I. Antioxidants: Characterization, Natural Sources, Extraction and Analysis, *Food Res.* 2015; 74: 10-36.
- [8] Tandee, K., Phimphilai, S., Jaturonglumlert, S., Teerawutgulrag, A., Varith, J., Nuglor, S., and Phimphilai, K. Effect of Ultraviolet Radiation and Ultrasonication on Quality of Red Rice Extract Drink, *RMUTI J., Special issue*, 2015; 217-222.
- [9] Ministry of Public Health. Article No. 356: Beverages in Closed Containers. Royal Thai Government Gazette, 2013; 87: 93-97.
- [10] Ministry of Public Health. Article No. 364: Food Standard on Pathogens. Royal Thai Government Gazette, 2013; 148(13): 42.
- [11] Ortoneda, M., Cullen, J.D, Phipps, D.A., and Al-Shamma'a, A.I. Use of UV Light for Environmentally Friendly Microbial Control, Online, 2010.
- [12] Fredericks, I.N., du Toit, M., and Krügel, M., Efficacy of Ultraviolet Radiation as an Alternative Technology to Inactivate Microorganisms in Grape Juices and Wines, *Food Microbiol.*, 2011; 28(3): 510-517.
- [13] Gabriel, A.A., Aguila, M.L.C., and Tupe, K.A.M. Application of Ultraviolet-C Radiation to Inactivate Acid-and-Desiccation Stressed *Salmonella Enterica* in Young and Mature Coconut Liquid Endosperm Mix Beverage, *Food Control*, 2011; 51: 425-432.
- [14] HakguderTaze, B., Unluturk, S., Buzrul, S., Alpas, H. The Impact of UV-C Irradiation on Spoilage Microorganisms and Colour of Orange Juice, *J. Food Sci. Tech.*, 2015; 52(2): 1000-1007.
- [15] Keyser, M., Müller, I.A., Cilliers, F.P., Nel, W., and Gouws, P.A. Ultraviolet Radiation as a Non-Thermal Treatment for the Inactivation of Microorganisms in Fruit Juice, *Innov. Food Sci. Emerg. Technol.*, 2008; 9(3): 348-354.
- [16] Association of Official Analytical Chemists. Official Methods of Analysis of AOAC International, Washington D.C., 2005.
- [17] Re, R., Pellegrini, N., Proteggente, A., Pannala, A., Yang, M., and Rice-Evans, C. Antioxidation Activity Applying an Improved ABTS Radical Cation Decolorization Assay, *Free Radic. Biol. Med.*, 1999; 9(10): 1231-1237.
- [18] Benzie, I.F.F. and Strain, J.J. The Ferric Reducing Ability of Plasma (FRAP) as a Measure of "Antioxidant Power": the FRAP Assay, *Anal. Biochem.*, 1996; 239(1): 70-76.
- [19] Pinsirodom, P. and Changnoi, W. Comparison of Total Polyphenol Content and Antioxidant Potential of Extracts Obtained from Seeds of Different Citrus Fruits Cultivated in Thailand, *Food* 2002; 32(4): 300-307.
- [20] Tran, M. and Farid, M. Ultraviolet Treatment of Orange Juice, *Innov. Food Sci. Emerg. Technol.*, 2004; 5(4): 495-502.
- [21] Aguilar-Garcia, C., Gavino, G., Baragaño-Mosqueda, M., Hevia, P., and Gavino, V.C. Correlation of Tocopherol, Tocotrienol, γ -Oryzanol and Total Polyphenol Content in Rice Bran with Different Antioxidant Capacity Assays, *Food Chem.*, 2007; 102(4): 1228-1232.
- [22] Sompong, R., Siebenhandl-Ehn, S., Linsberger-Martin, G., and Berghofer, E. Physicochemical and Antioxidative Properties of Red and Black Rice Varieties from Thailand, China and Sri Lanka, *Food Chem.*, Vol.124, No.1, 1 January 2011, 132-140, 2011.
- [23] Wootton-Beard, P.C., Moran, A., Ryan, L., Stability of the Total Antioxidant Capacity and Total Polyphenol Content of 23 Commercially Available Vegetable Juices before and after *in vitro* Digestion Measured by FRAP, DPPH, ABTS and Folin-Ciocalteu Methods, *Food Res. Inter.*, 2011; 44(1): 217-224.

- [24] Erkan, M., Wang, S., and Wang, C. Effect of UV Treatment on Antioxidant Capacity, Antioxidant Enzyme Activity and Decay in Strawberry Fruit, *Postharvest Biol. Technol.*, 2008; 48(2): 163-171.
- [25] González-Aguilar, G.A., Zavaleta-Gatica, R., and Tiznado-Hernández, M.E. Improving Postharvest Quality of Mango 'Haden' by UV-C Treatment, *Postharvest Biol. Technol.*, 2007; 45(1): 108-116.

Energy Saving Potential in a Fresh Market in Nakhon Sawan Province, Thailand

Kittisak Khuwaranyu^{1*}, Pongsiri Jaruyanon¹

Received: 30 June 2015; Accepted: 13 July 2015

Abstract

This research aims at studying the feasibility of starting an energy saving program at a fresh market in Nakorn Sawan province. The researcher investigated and collected data from fresh markets and identified the basic level of feasibility to make improvements at a targeted fresh market and then established a pilot program at the fresh market. From the research findings, six main energy saving measures, which can be divided into five electricity saving measures, and heat energy saving measures were found. All measures can result in saving up to 34.05%. As a result, it can be concluded that all proposed measures can be used as guidelines for saving energy in other fresh markets.

Keywords: energy saving, fresh market, energy consumption

Introduction

Nowadays, energy is essential for human beings as it is embedded in all sectors including housing, business, and manufacturing. As a result, energy is a really significant factor for the manufacturing industry. especially, due to rapidly growing industry and technology towards a global economy. This accelerates the demand for energy in order to uphold national development. Recent data indicates that Thailand has a steadily rising GDP which has risen annually at the average of 4% while the annual rate of electricity energy consumption has gradually increased at 4.2 %, which costs many billion baht¹.

Over the next 20 years, if either the energy saving measures or efficient energy increasing measures are not fully implemented, the demand for energy at BAU (Business-as usual) will actually increase from 71,000 ktoe/year (kilotonne of oil equivalent, as of 2010) to 151,000 ktoe (i.e. 2.1times or equivalent to 3.9% annual increasing rate), assuming that GDP increases at 4.2 % annually and the demand for energy in both industries and commercial buildings are higher than that in other sectors. Yunfeng² studied how to save energy in buildings in China by investigating the energy consumption condition

and efficient consumption. The research findings indicated that the standard of living has been improved and building awareness towards the energy saving is the most successful factors for energy saving in China. Hyeonjeong³ investigated the decision making and scheduling for electricity in the house model designed for energy saving purpose. The “data record for daily activities” were done for making decision in using energy. The data were collected and analyzed to the development indicators. The result showed that the volume of electricity consumption was significantly decreased by the setting switching on-and-off to home appliance. Ruzena⁴ proposed the energy saving initiatives by setting new lighting system which focuses on the efficient lighting and expense. When the new energy saving strategies were used, it was seen that the full participation from employees in the sampled firms could help boost efficient energy savings. Rajesh⁵ examined the assessment for feasibility for energy saving in hotels in Chaipura, India. According to research findings, applying the energy saving measures led to highly feasible energy saving. These measures can also be applied to analyze the energy saving feasibility in other sectors e.g. hospitals, office buildings, department

¹ Mechanical Engineering Department, Faculty of Engineering and Industrial Technology, Silpakorn University, Nakhon Pathom, 73000, Thailand

* kittisak_mesu@yahoo.com

stores, etc.

One of the important business sectors definitely relating to daily life in Thailand is the fresh market which uses many systems: lighting system, cooling system, electric motor system, and heating system from LPG and charcoal. Since this has resulted in the high energy consumption, the researcher co-ordinates with the Energy Office in Nakhon Sawan province for the efficient energy saving which includes energy consumption and energy cost reduction. In addition, the research can also be applied to other fresh markets in Thailand.

Materials and Methods

As illustrated in (Figure 1) this research was conducted by following six main steps for three sample groups – researcher group, vendors in fresh market, and governmental offices. Some steps were taken by more than one researcher. Furthermore, in step 4, preparing the pre-feasibility for improving the energy consumption in fresh market. was divided into 8 minor steps. All steps are as follows:

I. Identify research objectives – the researcher identified research objectives to prepare feasibility study for energy saving for both electricity and heat power in the pilot fresh markets

II. Review literature and previously related research – this is to understand the insight from the related studies

III. Collect data – the researcher collected data from fresh markets in Nakhon Sawan province to select the pilot fresh markets

IV. Prepare pre-feasibility study for improving the energy saving in fresh markets – this is to identify energy saving measures in order to apply to the others and can be divided into minor steps as follows (please see Research Findings for details):

- a. Select fresh markets for preparing pre-feasibility study
- b. Identify data which was focusing on the study
- c. Design survey form
- d. Contact fresh market managers/ owners

- e. Collect data at fresh markets
- f. Prepare pre-feasibility study for improving the energy saving
- g. Select the “pilot fresh market”
- h. Collect and analyze data and feasibility for improving the energy saving

V. Analyze the energy consumption of the pilot fresh markets – it is to calculate the saving rate from the energy saving measures by statistical techniques.

Summarize the feasibility of improving energy consumption in pilot fresh markets – this is to demonstrate the result of energy saving, reducing expenses, cost, and payback period of each energy saving measure.

Results

The research findings are as follows:

a. Select fresh markets for preparing pre-feasibility study

1) To identify the targeted four fresh markets for preparing pre-feasibility for improving energy saving, the researcher set up two main criteria as follows: The fresh market are owned by government offices

2) The fresh market is certified as a good and Thai healthy market at the excellent level (by Nakhon Sawan health station No. 8, Department of Health, Ministry of Public Health)

The fresh markets which meets requirements above are as follows (as expressed in Table 1):

b. Identify data which was focused to study as follows:

1) Primary data: location, name of fresh market, managers/ owners, map, layout (booth)

2) Energy consumption data: electricity usage rate, number and size of transformer, energy consumption data, number of electrical appliance, using method, and electrical power expense

c. Design survey form

The researcher team divided survey form into two types—Form 1 which focused on the co-operation and attitude of fresh market managers/owners and Form 2 which focused on other aspects to be used for pre-feasibility for improving energy saving in fresh markets.

d. Contact fresh market managers/ owners

The researcher contacted the four fresh market managers and owners – Nakhon Sawan Municipality, Banphotphisai Sub district Municipality, Thatako Sub district Municipality, and Phayuhakhiri Sub district Municipality.

e. Collect data at fresh markets

The researcher collected primary data, electricity and heat power usage data, and equipment using electricity and/ or heating power at all booths in four targeted fresh markets.

f. Prepare pre-feasibility study for improving the energy saving

Referring to two types of collected data (Table 2 and 3), the findings was shown as follows:

g. Select the “pilot fresh market”

The researcher verified the completeness of data for assessing the pre-feasibility of improving energy saving in fresh markets as expressed in (Table 4 and 5).

h. Collect and analyze data and feasibility for improving the energy saving

After selecting the fresh market at Nakhon Sawan Municipality as “pilot fresh markets”, the researcher estimated and analyzed the initiatives to improve the energy saving, validated measures to adjust equipment (Table 6), and designed the set up the equipment to save energy.

Conclusions

1. Energy consumption analysis

With the total area of 1,970 m², the fresh market at Nakhon Sawan Municipality, ranked as good level, can be divided into two main areas – the front area which covers 1,250 m² and the back area which covers 720 m². There are 178 booth which operate approximately 18-20 hours/ day, at 11:00 PM – 7:00 PM.

As for the energy consumption, it was found that the highest energy consumption was in electricity power which totally requires 140,981.60 kWh/year, equivalent to 621,515.60 THB/ year, and can be classified into two main purposes. The first one is the power used in the main area i.e. lighting systems within fresh market,

side area, footpath and street, and toilets which operate at 5:00 PM – 8:00 AM. The usage in these areas is 61,947.97 kWh/year or equivalent to 272,582.12 THB/ year. The main purpose is lighting system (85 %). Another purpose is for booth in fresh market i.e. light bulb, cooler, grinder, coconut extracting machine, etc. which operates at 2:00 AM – 8:30 AM. The usage in these areas is totally 79,033.63 kWh/year or equivalent to 348,933.48 THB/ year. The main purpose is lighting systems (51%) and electric motors used in grinder and coconut extracting machine (35%).

2. Result of energy consumption analysis

Measurement to energy consumption in fresh market :

As for the energy consumption at fresh market in Nakhon Sawan Municipality, it was found that the lighting system at the main area starts at 5:00 PM and fully operates at 6:00 PM until 8:00 AM of the following day. There is no energy consumption at the main area at 8:00 AM – 5:00 PM. For the electricity power used at booth (red line), it was operated at high level at 2:00 AM – 8:30 AM when the market vendors use chiefly for lighting in their booth (e.g. lighting, cooler, and grinder). From the summary of energy conservation measures, the total implemented measures saving for the market is around 140,981.60 Baht/year (48,010.92 kWh/year) in which all saving cost come from the electrical energy saving measures. All measures can result in saving energy up to 34.05%

Acknowledgement

This research was supported by Energy Conservation Promotion Fund (ENCON Fund), Energy Policy and Planning Office, Ministry of Energy, Royal Thai Government and the Department of Mechanical Engineering, Faculty of Engineering and Industrial Technology, Silpakorn University, Thailand.

References

- [1] Electricity Generating Authority of Thailand (EGAT). Electricity usage and electricity generating in Thailand. [Online] (May, 20 2015) .

- [2] Yunfeng, H. "Development of energy-saving buildings in China", *Energy and Buildings*, 2011; 21: 298-302.
- [3] Hyeonjeong, Y. and Hyunsoo L. "Lighting scheduling for energy saving in smart house based on life log data", *Energy and Buildings*, 2014; 22: 403-413.
- [4] Ruzena, K. "Energy Saving Techniques and Strategies for Illumination in Industry", *Energy policy*, 2015; 100: 187-195.
- [5] Rajesh, C. "Energy saving potential through Energy Conservation Building Code and advance energy efficiency measures in hotel buildings of Chaipura City, India" *Energy and Buildings*, 2015; 92: 282-295.

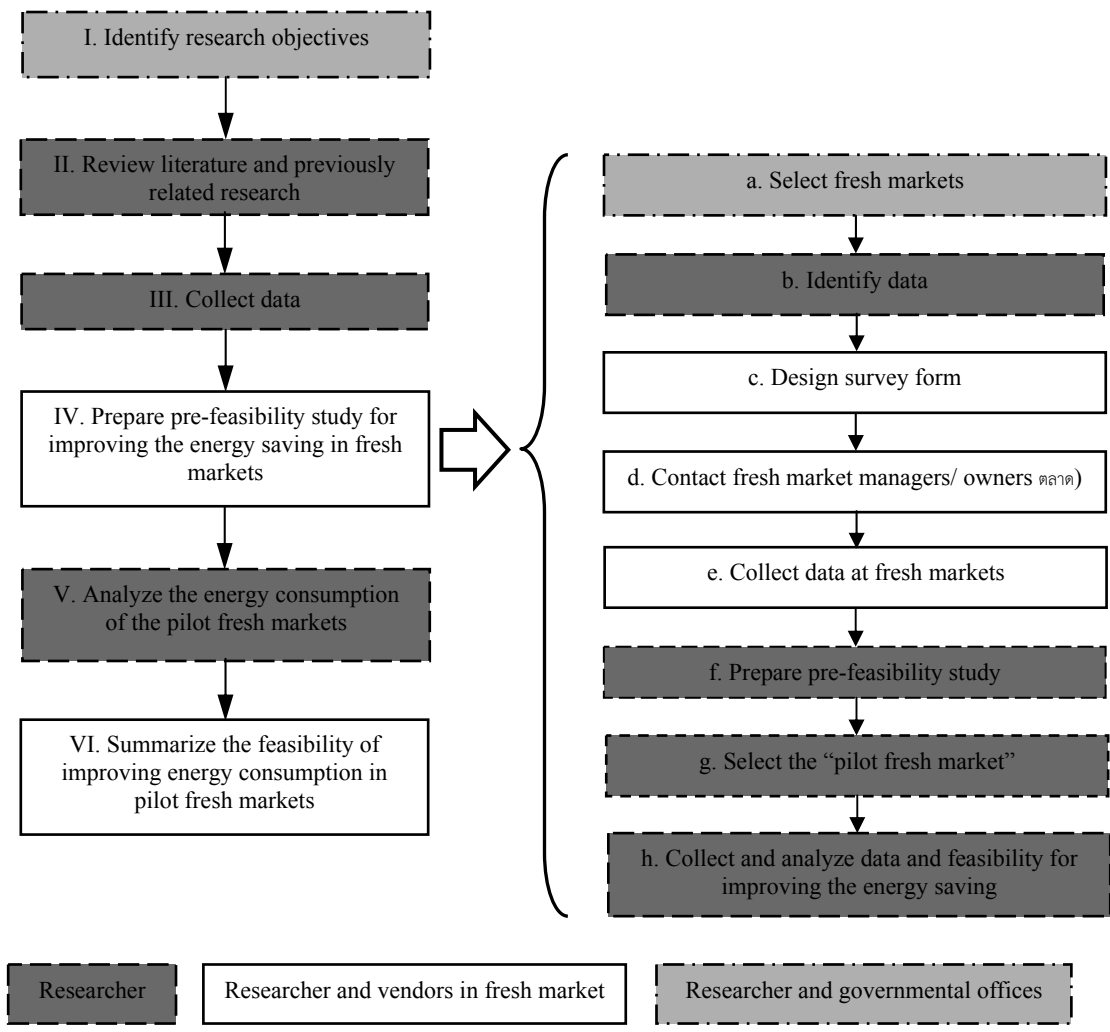


Figure 1 Research methodology

Table 1 The fresh markets that can be acceptable two main criteria

No.	Name of fresh market	Location				Fresh market managers/ owners	Remark
		House No.	Village No.	Sub-district	District		
1	Nakhon Sawan Municipality market	-	-	Paknampo	Meuang Nakhon Sawan	Nakhon Sawan Town Municipality	Thai healthy market good level
2	Thatako Subdistrict Municipality market	-	1	Thatako	Thatako	Thatako Subdistrict Municipality	Thai healthy market good level
3	Banphotphisai Subdistrict Municipality market	-	2	Thangio	Banphotphisai	Banphotphisai Subdistrict Municipality	Thai healthy market excellent level
4	Phayuhakhiri Subdistrict Municipality market	-	4	Phayuhakhiri	Phayuhakhiri	Phayuhakhiri Subdistrict Municipality	Thai healthy market good level

Table 2 Co-operation and attitude of fresh market managers/ owners

Detail	Municipality fresh market			
	Nakhon Sawan	Thatako	Banphotphisai	Phayuhakhiri
1. Municipality				
2. Co-operation and attitude of fresh market managers/ owners				
2.1 Activity for energy saving that Municipality has ever conducted	Yes	No	No	No
2.2 Activity for energy saving that the fresh market has ever conducted	Yes	No	Yes	No
2.3 Knowledge of energy saving	Yes (Medium)	Yes (Few)	Yes (Few)	Yes (High)
2.4 Interest in implementing energy saving activities	Yes	Yes	Yes	Yes
2.5 Attitude towards energy saving	Fully supporting	Not supporting	Supporting but in some extent	Supporting but in some extent
2.6 Energy management policy	Yes	Yes	Yes	Yes
2.7 Organization management	Yes	No	No	No
2.8 Motivation and reinforcement	Yes	No	No	No
2.9 Information system	No	No	No	No
2.10 Public relations	No	No	No	No
2.11 Investment	Yes	No	No	No
3. Assessing the readiness for participating the energy saving improvement				
3.1 Is your fresh market ready to join the energy saving campaign?	Yes	Yes	Yes	Yes
3.2 If your fresh market joins, you are willing to share cost of changing the equipment	Yes	Yes	Yes	Yes

Table 3 Other aspects to be used for pre-feasibility for improving energy saving in fresh markets.

Detail	Municipality fresh market				
	Municipality	Nakhon Sawan	Thatako	Banphotphisai	Phayuhakhiri
1. Data Completeness		High	Medium	Few	Few
2. No. of trade panel		178	121	38	20
3. Energy consumption					
3.1 Electricity consumption (kWh/year)		140,981.60	78,342.26	20,890.15	20,406.42
3.2 Electricity cost (Baht/year)		588,716.64	313,369.04	83,560.60	81,625.68
3.3 Fuel consumption (LPG - kg/year)		5,832.70	1,825.00	5,333.06	-
3.4 Fuel cost (Baht/year)		163,315.61	51,100.00	149,325.68	-
3.5 Net consumption (MJ/year)		800,510.29	373,701.89	343,084.15	73,463.11
Total energy consumption (High-Low)		1	2	3	4
4. Energy consumption of market facility					
4.1 Electricity consumption (kWh/year)		61,947.97	21,435.71*	8,674.56*	20,307.87
4.2 Electricity cost (Baht/year)		272,582.12	85,742.84	34,698.24	81,231.4*8
5. Energy consumption of all trade panel					
5.1 Electricity consumption (kWh/year)		79,033.63	56,906.55	12,215.59	98.55
5.2 Electricity cost (Baht/year)		316,134.52*	227,626.20*	48,862.36*	394.20*
5.3 Fuel consumption (LPG - kg/year)		5,832.70	1,825.00	13,296.43	-
6. Maximum energy use by system sector (market facility)					
Lighting system (%)		94.31	58.38*	100.00*	100.00*
7. Maximum energy use by system sector (trade panel)					
Lighting system (%)		36.30	30.46	75.56	-**
8. Electricity saving potential (measure)		5	4	2	2
9. Thermal energy saving potential (measure)		1	1	1	Non
10. Percent of energy reduction of the total energy consumed					
10.1 Electricity saving potential (%)		30.34	13.57	20.05	71.76
10.2 Thermal energy saving potential (%)		23.29	50.00	25.00	0.00
11. Energy Saving					
11.1 Electricity saving potential (kWh/year)		42,772.56	10,629.96	4,189.04	14,644.10
11.2 Thermal energy saving potential (MJ/year)		68,248.00	45,834.88	166,970.05	0.00
Total energy saving potential (MJ/year)		222,229.22	84,102.73	182,050.59	52,718.76

Remark * The values are estimated or re-calculated by using energy data, -** very less usage

Table 4 The completeness of data for assessing the pre-feasibility of energy saving potential

Detail		Municipality fresh market			
Municipality		Nakhon Sawan	Thatako	Banphotphisai	Phayuhakhiri
1	Primary data	1	1	0.5	0.5
2	Market layout (position of energy equipment)	1	0.5	0.5	0
3	Energy consumption of market facility	1	0.5	0.5	0
4	Energy consumption of all trade panel	1	0.5	0.5	0
5	Fuel consumption (LPG – trade panel)	0.5	0.5	0.5	0.5
6	Percent of energy reduction of the total energy consumed (market facility)	1	0.5	0	0
7	Percent of energy reduction of the total energy consumed (trade panel)	1	0.5	0	0
8	Energy saving potential	1	0.5	0.5	0.5
Total (Ave.)		0.94	0.56	0.38	0.19
Data Completeness		High	Medium	Few	Few

Remark: 1 – Complete collected data, 0.5 – partially collected data and 0 – non data

Data completeness (Score) : High (0.8-1.0), Medium (0.5-0.8) and Few (less than 0.5)

Table 5 Energy usage data and energy saving potential

Detail		Municipality fresh market			
Municipality		Nakhon Sawan	Thatako	Banphotphisai	Phayuhakhiri
1. Data Completeness		High	Medium	Few	Few
2. No. of trade panel		178	121	38	20
3. Energy consumption					
	3.1 Electricity consumption (kWh/year)	140,981.60	78,342.26	20,890.15	20,406.42
	3.2 Electricity cost (Baht/year)	588,716.64	313,369.04	83,560.60	81,625.68
	3.3 Fuel consumption (LPG - kg/year)	5,832.70	1,825.00	5,333.06	-
	3.4 Fuel cost (Baht/year)	163,315.61	51,100.00	149,325.68	-
	3.5 Net consumption (MJ/year)	800,510.29	373,701.89	343,084.15	73,463.11
	Total energy consumption (High-Low)	1	3	2	4
8. Electricity saving potential (measure)		5	4	2	2
9. Thermal energy saving potential (measure)		1	1	1	ไม่
11. Energy Saving					
	11.1 Electricity saving potential (kWh/year)	42,772.56	10,629.96	4,189.04	14,644.10
	11.2 Thermal energy saving potential (MJ/year)	68,248.00	45,834.88	166,970.05	0.00
	Total energy saving potential (MJ/year)	222,229.22	84,102.73	182,050.59	52,718.76

Table 6 The energy conservation measure for improving the energy saving

No.	Title of Measure	Potential (per year)				Cost	Investment cost	Payback Period
		Energy source	Quantity	Unit	Energy (MJ)	(Baht)	(Baht)	(Year)
1	Replacing the existing gas stove (LPG) with high efficiency gas stove	LPG	1,358.71	kg	68,248.00	38,043.88	60,000.00	1.58
2	Replacing the existing incandescent light bulb with LED light bulb in trade panel area	Electrical	12,594.12	kWh	45,338.83	55,604.13	36,570.00	0.66
3	Replacing the existing fluorescent light tube (36 Watt) with LED light tube (18 Watt)	Electrical	6,268.06	kWh	22,565.02	27,674.03	49,500.00	1.79
4	Replacing the existing HID lamp (400 Watt) with LED light lamp (200 Watt)	Electrical	3,236.09	kWh	11,649.92	34,105.92	130,600.00	3.83
5	Replacing the existing spotlight (400 Watt) with LED light lamp (200 Watt)	Electrical	4,415.04	kWh	15,894.14	24,160.78	111,760.00	4.63
6	Replacing the existing fluorescent light tube (36 Watt) with LED light tube (18 Watt) in main market area	Electrical	2,842.92	kWh	10,234.51	12,565.71	27,000.00	2.15
7	Using solar power to produce electricity (20 kW)	Electrical	16,060.00	kWh	57,816.00	70,904.90	2,300,000.00	32.44
Total		-	-	-	231,746.43	263,059.35	2,715,430.00	10.32

Grand total electric saving = 140,981.60 kWh/year

Grand total cost saving = 48,010.92 Baht/year

Energy saving = 34.05 %

Current-mode Sinusoidal Oscillator Based-on CCCCTAs and Grounded Capacitors with Amplitude Controllable

Phanida Srakaew¹, Atthapon Muenthom¹, Suphaphorn Panikhom¹, Adirek Jantakun¹

Received: 12 June 2015; Accepted: 13 July 2015

Abstract

This article describes the sinusoidal oscillator with amplitude controllable based-on CCCCTAs. The proposed circuits consist of 2 CCCCTAs and 2 grounded capacitors. In addition, the proposed circuits can be electronically controlled of condition and frequency of oscillation with bias current of CCCCTAs. The output signals have high output impedances which are connected or driven to next stages or loads. Furthermore, the output signals can be electronically adjusted the amplitude which is easily and convenient for uses in communication systems or demonstrated in laboratory. The PSPICE simulation results are confirmed that the proposed circuits have a good performance and accordance with the theoretical analysis.

Keywords: Sinusoidal oscillator, Current-mode, CCCCTA, Grounded Capacitor

Introduction

The sinusoidal oscillator is vastly used in electrical or electronic engineering such as the modulation and demodulation circuits of communication system, instrument or measurement system, control system, and in laboratory of communication systems¹⁻⁴. Currently, the passive elements in analogue signal processing circuits are frequently connected to ground since, they require a small area when fabricated to integrated circuits (IC). The grounded capacitor is expediently reduced to the size of an IC⁴. In addition, the grounded capacitor serves to compensate or eliminate the latent capacity that occurs at the terminals of active device and the nodes of the circuit¹⁻⁶. An adjustment of the amplitude of sinusoidal signal is attractive to research and development^{4,7}, since it can be applied to communication systems. These are AM (Amplitude Modulation)/ASK (Amplitude Shift Keying) which are classical modulation schemes in communication system. Furthermore, AM is useful in plenty of applications such as AM radio broadcasting and aircraft navigation system. Moreover, ASK also is widely-used in many applications; for example in optical communication^{4,7}. AM and ASK are vastly used in laboratories for studying fundamental of electronics/

telecommunication engineering.

The sinusoidal oscillator based-on CCCCTA has been reported in literature¹⁻¹⁴. For example, the oscillator circuits in¹⁻⁶ are compacted and it can be tuned the condition of oscillation (CO) and frequency of oscillation (FO) with electronic method by DC bias current of CCCCTA. However, the proposed circuits in¹⁻³ afflicted from using 2 output ($2g_m$) in which is the circuits are complicated. Also, the circuits in Ref.³⁻⁵ are using an external passive resistor in which thermal noise may occur and it is difficult to implement in IC¹⁴. The circuit in⁷⁻¹³ employs two CCCCTAs and two grounded capacitors which is ideal for IC implementation. Also, it can be electronically/independently adjusted. Unfortunately, the output currents are unfeasible for adjustment of amplitude which is not convenient in AM/ASK systems. The current-mode sinusoidal oscillator in^{4,14} introduced FO and CO which can be electronically adjusted by DC bias currents as well as the amplitude can be tuned with biasing of CCCCTA, which is good for AM/ASK communication system. Nevertheless, the output currents can control the amplitude with only a single output.

¹ Department of Electronics and Telecommunication, Faculty of Engineering, Rajamangala University of Technology Isan, Khonkaen Campus, Khonkaen, 40000, Thailand Email: adirek.ja@rmuti.ac.th

The purpose of this paper is to introduce the synthesis of a sinusoidal oscillator circuit based-on CCCCTAs. The usefulness of proposed circuits have the following:

- Using grounded capacitors which are suitable for IC implementation and eliminable the parasitic capacitances at ports/nodes.
- The CO and FO can easily be electronically controlled via DC bias current of CCCCTAs.
- The output currents have high output impedances that are useful for current-mode circuitry configuration.
- The amplitude of output currents can be electronically/independently adjusted with DC bias current, which is suitable for using in AM/ASK systems.

The workability of the proposed sinusoidal oscillator is confirmed via the PSPICE simulation.

Current controlled current conveyor transconductance amplifier (CCCCTA)

Since the proposed circuit is based on CCCCTA. The characteristics of the ideal CCCCTA are represented by the following hybrid matrix:

$$\begin{bmatrix} I_y \\ V_x \\ I_{z,zc} \\ I_o \end{bmatrix} = \begin{bmatrix} 0 & 0 & 0 & 0 \\ 1 & R_x & 0 & 0 \\ 0 & 1 & 0 & 0 \\ 0 & 0 & 0 & \pm g_m \end{bmatrix} \begin{bmatrix} V_y \\ I_x \\ V_o \\ V_z \end{bmatrix} \tag{1}$$

For the CCCCTA implemented by a bipolar technology, the parasitic resistance is given as

$$R_x = \frac{V_T}{2I_{B1}} \tag{2}$$

and transconductance is given as

$$g_m = \frac{I_{B2}}{2V_T} \tag{3}$$

The circuit symbol and equivalent circuit of the CCCCTA are illustrated in (Figure 1(a) and (b)), respectively

Proposed Circuit

The proposed sinusoidal oscillator is shown in (Figure 2) It consists of two CCCCTAs, two grounded capacitors and one grounded resistor. The use of grounded passive element is advantageous from the point of view of integrated circuit implementation. Moreover, it is found that the oscillator provides high output impedance which can directly drive a load without buffering devices. Using (1) and doing routine circuit analysis, the system characteristic equation can be expressed as

$$s^2 C_1 C_2 R_{x1} R_{x2} + s(C_2 R_{x2} - C_1 R_{x1}) + 1 = 0 \tag{4}$$

From (4), it can be seen that the proposed circuit can produce oscillations if the condition of oscillation is fulfilled

$$C_1 R_{x1} = C_2 R_{x2} \tag{5}$$

If the above condition of oscillation (CO) is satisfied, the circuit produces oscillation with frequency (FO) of

$$\omega_{osc} = \frac{1}{\sqrt{C_1 C_2 R_{x1} R_{x2}}} \tag{6}$$

Substituting the parasitic resistance R_x and transconductance g_m as respectively shown in (2) and (3) into (5) and (6), the CO becomes

$$I_{A2} C_1 = I_{A1} C_2 \tag{7}$$

and the FO is obtained as

$$\omega_{osc} = \frac{2}{V_T} \sqrt{\frac{I_{A1} I_{A2}}{C_1 C_2}} \tag{8}$$

If $I_{A1} = I_{A2} = I_A$ and $C_1 = C_2 = C$, the FO is modified to

$$\omega_{osc} = \frac{2I_A}{V_T C} \tag{9}$$

From (9), it is clear that, the CO and FO can be adjusted simultaneously with electronic tuning by I_A .

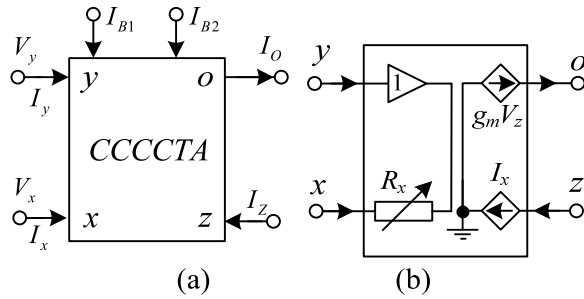


Figure 1 CCCCTA (a) schematic symbol (b) equivalent circuit

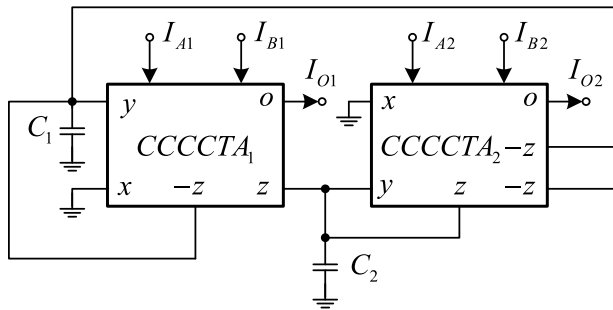


Figure 2 The proposed sinusoidal oscillator

Simultaneously, the output currents can be obtain as

$$I_{O1} = g_{m1}V_{z1} \tag{10}$$

and

$$I_{O2} = g_{m2}V_{z2} \tag{11}$$

It should be noted that the amplitude of the current output I_{O1} and I_{O2} can be electronically controlled by I_{B2} and I_{B1} , respectively. Moreover, they have high output impedances which is driven or cascaded to load without using a buffering device. Furthermore, if I_{B1} or I_{B2} is information signal, the AM and ASK can be generated at current outputs.

Simulation results

To prove the performances of the proposed oscillator, the PSPICE simulation was performed for examination. The BJT technology was simulated by using the parameters of the PR200N and NR200N bipolar transistors of ALA400 transistor array from AT&T. (Figure 3) depicts the schematic description of the CCCCTA used in the simulations with power supplies. The sinusoidal

oscillator was designed with , and . This yields oscillation frequency of 2.2MHz. (Figure 4 (a) and (b)) show simulated output waveforms in transient and steady state, respectively. (Figure 5) shows simulated output spectrum, where the total harmonic distortions (THD) of output currents are about 3.43%. To confirm the output current can be operated of AM, where I_{B1} was triangular signal with a 50kHz frequency is applied, The AM signal at I_{O1} is depicted in (Figure 6) Besides, the proposed circuit has functioned as AM generator, where I_{B2} was sinusoidal signal with a 50kHz frequency shown in (Figure 7) The results are proper with the theoretical analysis in (10) – (11).

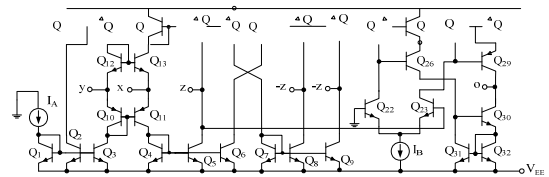


Figure 3 The internal construction of CCCCTA

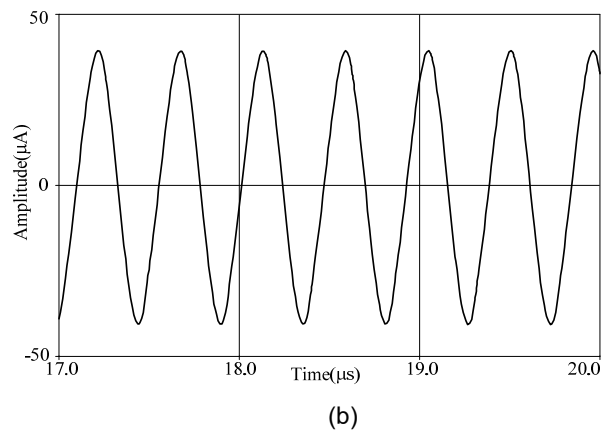
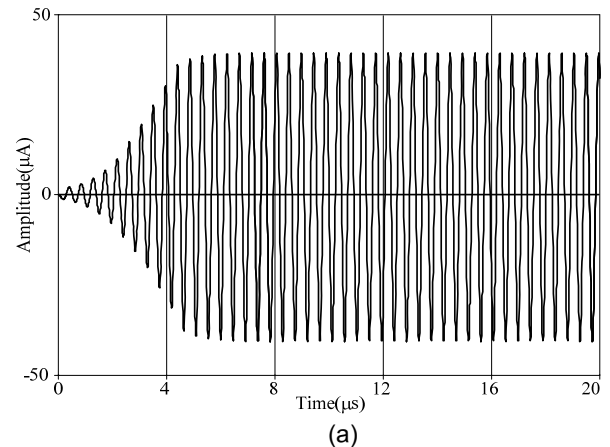


Figure 4 The simulated output waveforms (a) transient state (b) steady state

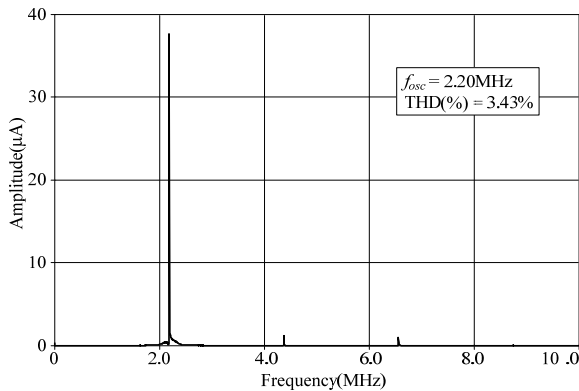


Figure 5 The simulated output spectrum

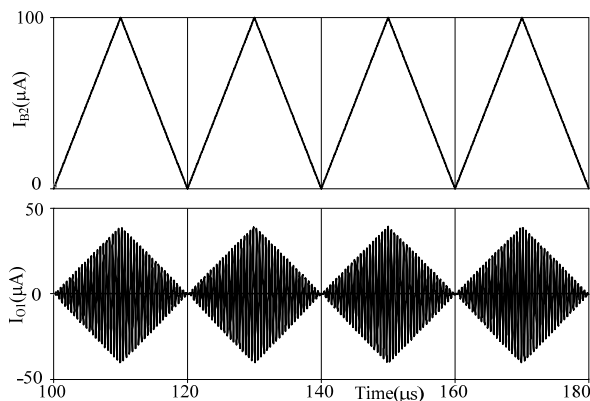


Figure 6 Results of operation of AM of I_{O1}

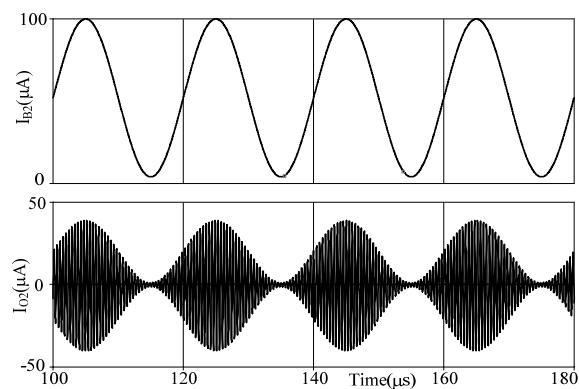


Figure 7 Results of operation of AM of I_{O2}

Conclusion

The sinusoidal oscillator using CCCCTAs and grounded capacitors with current controlled amplitude has been presented. It employs two CCCCTAs and two grounded capacitors. Also, grounded capacitors can reduce the fabrication area of IC and compensated the latent capacitance at node and input/output ports of CCCCTAs. In addition, the CO and FO can be adjusted with electronic tuning. Furthermore, the output current

signals can be electronically controllable which are easy for using in AM/ASK communication system. Not only the output current has high impedance but also the circuit can be cascaded without additional current buffers. The performance of proposed circuit are depicted through PSPICE simulation. The results agree well with the theoretical anticipation.

References

1. Bumronghoke T., Jaikla W., Siripruchayanun M., An Electronic Controllable Simple Current-mode Oscillator using Single MO-CCCCTA and Grounded Capacitors. The 1st international conference on Technical Education, Bangkok, 20-21 Jan. 2010. 217–220, 2010.
2. Thosdeekoraphat T., Summart S., Thongsopa C. Current-mode Sinusoidal Oscillator using Single Dual-output Current Controlled Current Conveyor Transconductance Amplifier (DO-CCCCTA). *Aust. J. Basic & Appl. Sci.*, 2013; 7(8): 230-236.
3. Maiti S., Pal R. R. Dual mode Quadrature Oscillator Employing Single Current Controlled Current Conveyor Transconductance Amplifier. *Int. J. Innovative Research in Science, Engineering and Technology*, 2013; 2: 3015-3112.
4. Jantakun A., Sa-ngiamvibool W., Current-mode Sinusoidal Oscillator using Current Controlled Current Conveyor Transconductance Amplifier. *Rev. Roum. Sci. Techn.– Électrotechn. et Énerg.*, 2013; 58(4): 415-423.
5. Lamun P., Kumngern M., Phasukkit P., Dejhan K., Current-mode Quadrature Oscillator using Single CCCCTA, *Ladkrabang Engineering Journal*, 2554; 28(1): 7-12.
6. Siripruchayanun M., Jaikla W., Current Controlled Current Conveyor Transconductance Amplifier (CCCCTA): A building block for analog signal processing. *Electrical Engineering*. 2008; 90: 443-453.
7. Pisutthipong N., Silapan P., Siripruchayanun M., CC-CCTA Based Current-mode Quadrature Oscillator. In Proc. The Seventh PSU Engineering Conference. Songkla, 20-22 May 2009, pp. 302–305, 2009.

8. Jaikla W., Noppakarn A., Lawanwisut S., New Gain Controllable Resistor-less Current-mode First Order Allpass Filter and Its Application. *Radioengineering*, 2012; 21(1): 312-316.
9. Duangmalai D., Jaikla W., Realization of Current-mode Quadrature Oscillator Based on Third order Technique. *Int. J. on Electrical and Power Engineering*. 211; 2(3): 46-49.
10. Tanaphatsiri C., Jaikla W. Electronically Tunable Four Phase Quadrature Oscillator Employing Current-controlled Current Conveyor Transconductance Amplifiers. 2011 Sixth International Symposium on Electronic Design Test and Application, Queentown, 17-19 Jan. 2011, 89-92.
11. Siripongdee S., Suwanjan P., Jaikla W., Electronically Tuned Current-mode Quadrature Oscillator with Independently Controllable FO and CO. *Recent Advance in Communications Circuits and Technological Innovation*. Paris, 2012. 213-216.
12. Pitaksuttayaprot K., Jaikla W., Implementation of Second Order Current-mode Quadrature Sinusoidal Oscillator with Current Controllability. *World Academy of Science Engineering and Technology*. 2013; 77: 476-478.
13. Singh S. V., Gupta G., Chhabra R., Nagpal K., Devansh., Electronically Tunable Voltage-mode Biquad filter/oscillator Based on CCCCTAs. *International Journal of Computer Science and Information Security*, 2010.
14. Sa-ngiamvibool W., Jantakun A. Quadrature Oscillator using CCCCTAs and Grounded Capacitors with Amplitude Controllability, *International Journal of Electronics*, 2014; 101(12): 1737-1758.

The Application of the Environmental Adaptation Concept to A Collector Road in KKU, Thailand

Pongrid Klungboonkrong¹, Monsicha Bejrananda², Natthapoj Faiboun³

Received: 29 May 2015; Accepted: 13 July 2015

Abstract

A collector road in Khon Kaen University, Thailand, previously suffered from pedestrian accident risk, adverse traffic environmental impacts and amenity problems. Most vehicles commonly travel at high speeds and barely reduce their speeds and stop to permit safe and secure pedestrian crossing. The main objectives of this research are as follows: (i) to determine the pedestrian accident risk in a specific area along a collector road in front of the complex building in KKU and (ii) to evaluate the applications of environmental adaptation concept to manage the vehicle/pedestrian conflicts on such road. Traffic calming namely the Environmental Adaptation Method (EAM) concept was applied to manage the hazardous interactions between pedestrian crossings and vehicle movements. The activity profile was modified in correspondence with the adapted speed profile by changing various road physical and land use characteristics of the collector road. The performance evaluation of road physical and land use modifications of the collector road in the two occasions were conducted. However, the recent road modification illustrated relatively unsuccessful results in reducing the operating speed while traffic flows increased dramatically.

Keywords: Traffic Calming, Environmental Adaptation, Sharing the Main Streets, Collector Road

Introduction

Khon Kaen University (KKU) is located in Khon Kaen city positioned in the middle of the northeastern region of Thailand. The campus covers around 900 hectares and has more than 60,000 residents including academia, students, staff members and others. KKU campus currently becomes the main access for local residents to connect with other parts of the city. The collector road in front of the complex building see (Figure1) is an important route in KKU and is used as the short cut between two national highways, located at the boundary of the campus. The conflicts between pedestrians and vehicular movements on the KKU collector road in front of the KKU complex building were pronounced and urgently needed

to be resolved. To alleviate the pedestrian and vehicle interactions, the concepts of the Environmental Adaptation Method (EAM)¹ was applied in this area in two occasions.

The main objectives of this research are as follows: (i) to determine the pedestrian accident risk in a specific area along a collector road in front of the complex building in the KKU and (ii) to evaluate the applications of environmental adaptation concept to manage the vehicle/pedestrian conflicts on such road. This paper describes the following elements: (i) introduction and research objective; (ii) research methodology; (iii) the applications of the environmental adaptation concept; (iv) results analysis and (v) conclusions.

^{1,3} Sustainable Infrastructure Research and Development Center (SIRDC), Department of Civil Engineering, Faculty of Engineering, Khon Kaen University, Thailand

² Faculty of Architecture, Khon Kaen University, Thailand

¹ E-mail: kku.sirdc.17@gmail.com

² E-mail: monbej@gmail.com

³ E-mail: tgalive@gmail.com

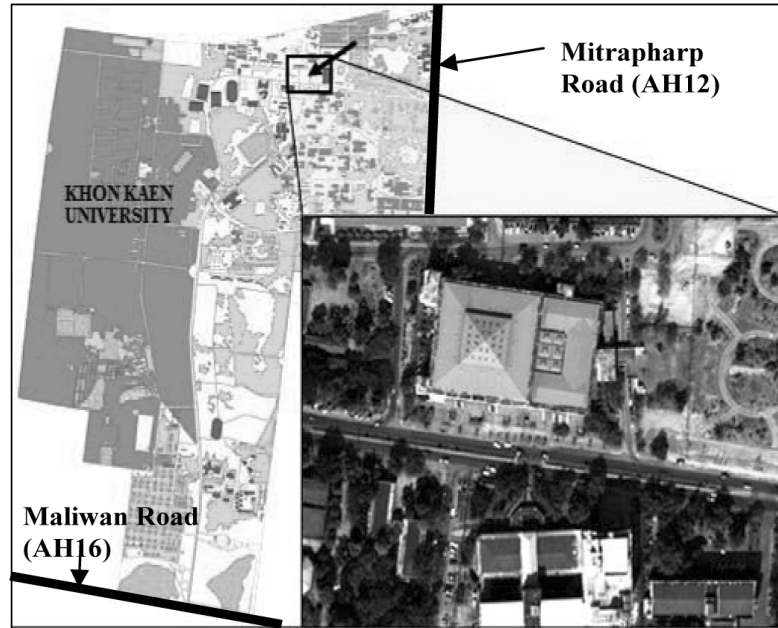


Figure 1 A collector road adjacent to the complex building in Khon Kaen University

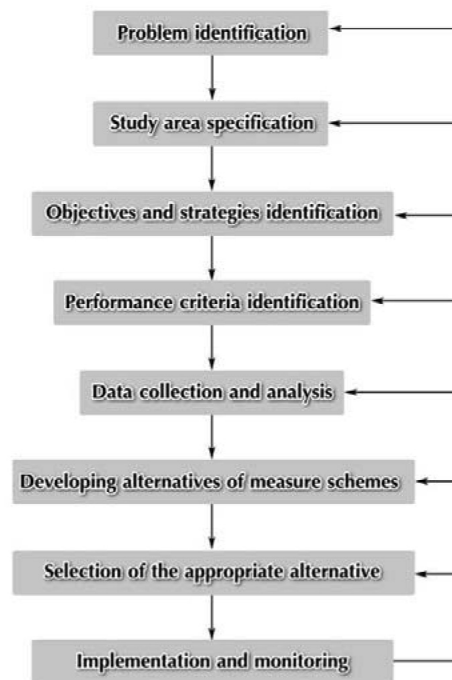


Figure 2 Flow chart diagram of the application process of the EAM concept

Materials and Methods

The interactions between pedestrian crossings and vehicle movements on a collector road in front of the KKU complex building were well recognized as pedestrian accident risk, traffic environmental impacts and amenity problems. EAM was consequently applied to resolve the problems. The following description will explain the important steps of the EAM application process to the

KKU collector road⁶ and (Figure 2) also shows flow chart diagram of the process. The EAM application processes are as follows: **(i) problem identification:** based on comprehensive field surveys and data collections of traffic and land use characteristics along a collector road in front of the KKU complex building has been suffered from pedestrian accident risk, traffic environmental impacts, amenity and esthetic and land scape problems;

(ii) study area specification: a collector road, a divided four-lane road with 1.5 meters median width and narrow footpath as shown in (Figure 1 and 3) in front of the complex building is functioning as the main street in KKU. In addition, the adjacent road network and surrounding land use on both sides of the road were also taken into account; **(iii) objectives and strategies identification:** the main objectives of this research is to improve road and land use physical characteristics to reduce conflicts between pedestrian maneuverings and vehicles movements (therefore pedestrian accident risk) and to improve the environmental and amenity quality; **(iv) performance criteria identification:** prior to conducting a detailed investigation of the project. The performance criteria must be identified and selected to assess and evaluate the outcome of proposed alternatives; **(v) data collection and analysis:** the collected data include physical road and land use characteristics of a collector road, adjacent road network and surrounding land use such as mid-block and intersection traffic volume, Origin and Destination (O-D) traffic data, operating speed, pedestrian crossing maneuvering and others; **(vi) developing alternatives of measure schemes:** alternatives will be developed in an integrated fashion. Therefore, different control, design and construction measures as suggested in¹ will be properly selected and incorporated as set of different alternatives to be proposed for implementation; **(vii) selection of the appropriate alternative:** the different alternative were proposed and compared in correspondence to the specified objectives. Then, the appropriate alternative was selected for actual implementation.

In this research, ESM, Song's model^{2,3} and other methods were adopted to assess the pedestrian accident risk performance. In addition, the micro-simulation modeling approach was systematically adopted to assess the several performance outcomes of the existing and the proposed alternatives⁴; **(viii) implementation and monitoring:** the selected alternative was actually implemented. Based on the performances criteria, the comparisons of between the before implementation (existing) situation and the implemented (the first implementation) alternatives were systematically

conducted. Subsequently, the second improvement was recently implemented. The details of the before-, the first- and the second- implementations and their determined performances were briefly summarized in section 5.

The Application of the environmental adaptation concept

EAM developed by Professor Hans Westerman¹ is the method to modify the physical and land use characteristics of the roads in response to the needs of users by process of land use planning and transportation policy. It aims to provide safety, efficient traffic operation, amenity, and cost-effectiveness to all road users. EAM focuses on the management of the conflicts between vehicles movements and pedestrian activities along sub-arterial roads, collector roads and the likes. EAM must be conducted in an integrated approach involving modification of street function and/or activities along the road. This approach is related to the alteration of road and/or activity function, the design and management of road space and its corresponding traffic, and the design and management of the frontage landscape. The following process is the heart of the application of the EAM¹: (i) gathering all pedestrian-oriented activities into a 'core zone' and directing all vehicle-oriented activities to a 'transition zone'; (ii) integrating all control measures to reduce traffic speed and/or minimize traffic volume in a core zone (to the target (the 85th percentile) speed of 25-35 km/h) and in a transition zone (to 40 km/h); and (iii) improving the quality of street and streetscape within study area by modifying the landscape, road space, and road frontage¹. The key factors influencing the design and planning for the EAM are the changes in road function, vehicle speed, traffic flow, through traffic, heavy vehicles, frontage activities, pedestrian behaviors, road reserve width and so on. Design for EAM can be reflected in the selection of design, construction and control measures in the way that they are integrated to achieve the primary objectives¹. EAM has been successfully applied and implemented in many projects in Australia^{1,5,6}.

The details of applications of EAM to the collector road in KKU are shown in (Table 3). In addition, it should

be noted that the process of EAM of the main street in KKU campus was done with high level of public participation. Information of EAM and design was disseminated through open sources such as university's radio channel, web site, advertising boards and brochures. The main objective of the adaptation is to reduce accidental risk due to pedestrian-vehicle conflict as well as increase amenities of the campus especially in student service zone.

The results of pedestrian accident risk, pedestrian safety analysis, and field surveys indicated that there is high risk of an accident during pedestrian crossing

maneuverings. The EAM concept therefore was applied to manage pedestrian safety problems. The activity profile (number pedestrians per hour per 100 m) is rearranged in accordance with the target speed profile by changing several road physical characteristics and landscape. Two actual improvements were completed as shown in (Figure 3). The summary of the details of road physical and land use characteristics during the before improvement period, the first improvement period and the second improvement period were also presented in (Table 1).

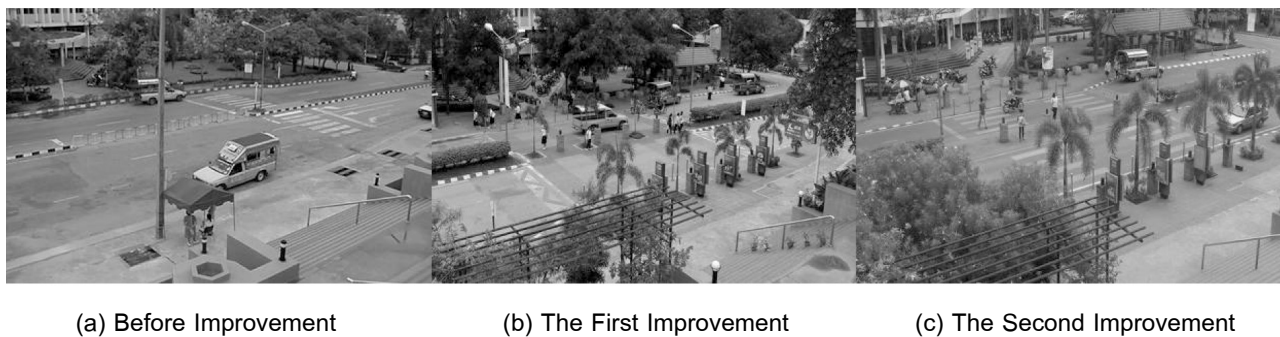


Figure 3 The road and land use physical characteristics of the study area during before and after applying the EA concept

Table 1 The road physical characteristics during the before-, the first- and the second-improvements

Road physical and land use adaption	Before Improvement	The 1 st Improvement	The 2 nd Improvement
Core zone and transition zones	No Core zone and transition zone	Core zone 40 m. Transition zone 80 m. (on both sides)	The same as the 1 st Improvement
Speed hump length at core zone	Level asphaltic concrete road surface without speed hump	Brick-paver speed hump is 40 m. long at the core zone. Speed hump side slopes are 7 percent and 15 cm. high.	In west-bound direction, two asphaltic-concrete speed hump of 82 m. and 15 m. long at core zone and transition zone, respectively. In east bound direction, one asphaltic concrete speed hump of 82 m. long at core zone. Speed-hump side slope are 7 percent and 10 cm. high.
The effective road width and the median and footpath width	Footpath width of 2.5 m. Road width of 9.0 m. in each direction the median width of 1.5 m.	Widening the median with from 1.5 m. to 2.0 m.; widening footpath width to at least 3.0 m. and reducing the road width to 6.0 m. in each direction.	The same as the 1 st Improvement
Bus stop locations	In west bound direction, bus stop location is situated at the location prior the pedestrian crossing	Relocating the new bus stop location in the west bound direction. Beyond the speed hump location	The same as the 1 st Improvement
Pedestrian crossing control at mid-block location	Raised median of 1.5 m. wide	Planting bush trees (Bougainvillea) along the median (transition zone), except for the core zone.	The same as the 1 st Improvement
Warning the driver and riders to reduce their running speeds	No warning	Installing rumble strips and changing the texture of road surface to brick pavement at the intersection prior to the improvement area	No rumble strips and the texture of road surface to asphaltic pavement at the intersection prior to the improvement area

Results

The road physical conditions, road networks, origin-destination data, traffic volumes, speeds, composition, pedestrian movements, jay walkers and jay runners were observed and collected during the before- and the first- and the second-improvement periods. Further analysis is solely concentrated on the vehicle/pedestrian interactions at the core zone (C) in the morning peak period.

As indicate in (Figure 4) in the before-improvement period at the core zone (C), the traffic flows (collected during 7:30 and 8:30 AM) in the east-bound, west-bound and combined both directions were 577, 610 and 1,187 passenger cars per hour, respectively, while in the first improvement period, the traffic volumes the east-bound, west-bound and combined both directions were 790, 812 and 1,602, respectively. In the second improvement period, the traffic volumes in the east-bound, west-bound and combined both directions were 833, 921 and 1,754, respectively. In the first and second improvement periods, the morning peak hourly (combined both directions) volumes were considerably greater than that in the before improvement period. This was possibly because during the first and the second improvement periods, the certain amount of through traffic attempted to avoid traffic congestion on the existing road network and use the collector road as the short-cut route.

(Figure 5) illustrated the speed profile collected during 7:30 and 8:30 AM in the core zone (C) and the

transition zones (A, B, D and E) during the before-, the first- and the second- improvement periods. In the before-improvement period, the 85th percentile speeds in the core zone were 54.8 km/h and 45.0 km/h in the east- and west-bound directions, respectively, while in the first-improvement period, the 85th percentile speeds in the core zone were reduce to 31.0 km/h and 30.6 km/h in the east- and west-bound directions, respectively. Interestingly, in the second-improvement period, the 85th percentile speeds in the core zone were become 43.0 km/h and 38.7 km/h in the east- and west-bound directions, respectively. It could be concluded that based on the 85th percentile speeds (in both directions) in the core zone, the first- and the second- improvements could potentially reduce traffic speeds dramatically. The results indicated that the installation of a speed hump (in the first-improvement period) can effectively reduce the hazardous speed (in the before- improvement period) to the safer target speed interval (25-35 km/h). McLean et al⁷ implicitly noted that if a car hit a pedestrian at the impact speed of 50 km/h, the probability of survival is only 7%. However, if the impact speed is reduced to 31 km/h, the probability of survival is greatly raised to 99 %. However, the effectiveness of the improvement in the second-improvement period was lesser than that of the first-improvement period, because of the construction of speed humps during the two improvement periods were physically different in terms of the type of road surface and their physical characteristics (side slopes and heights).

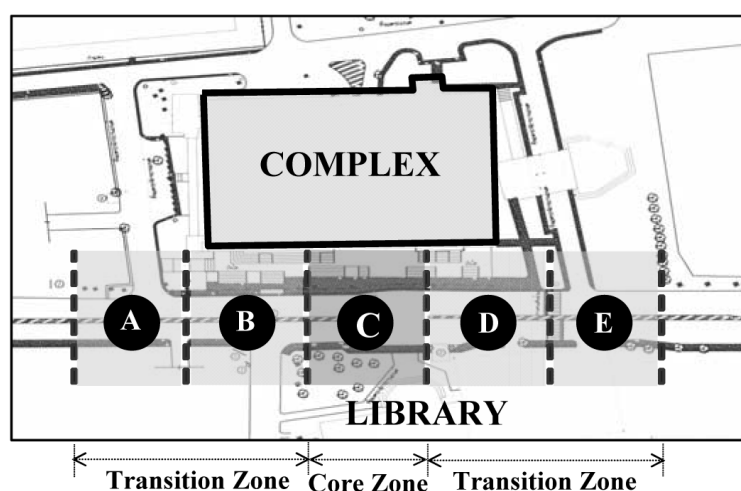
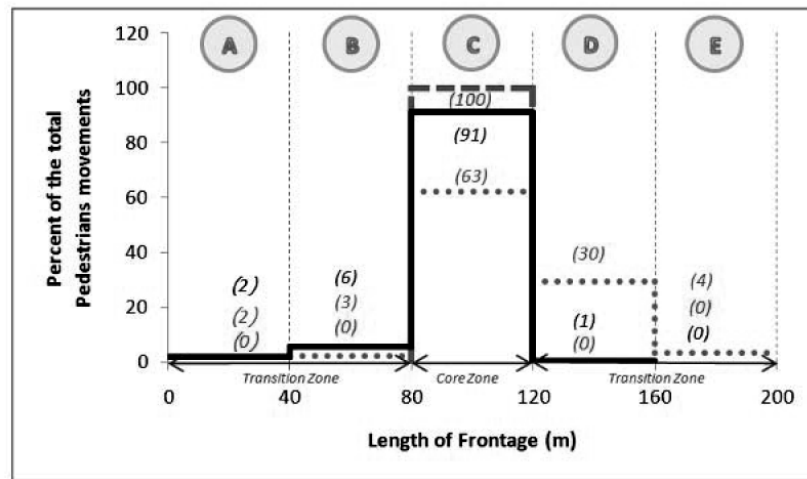


Figure 4 Five zones of pedestrian crossing data collection

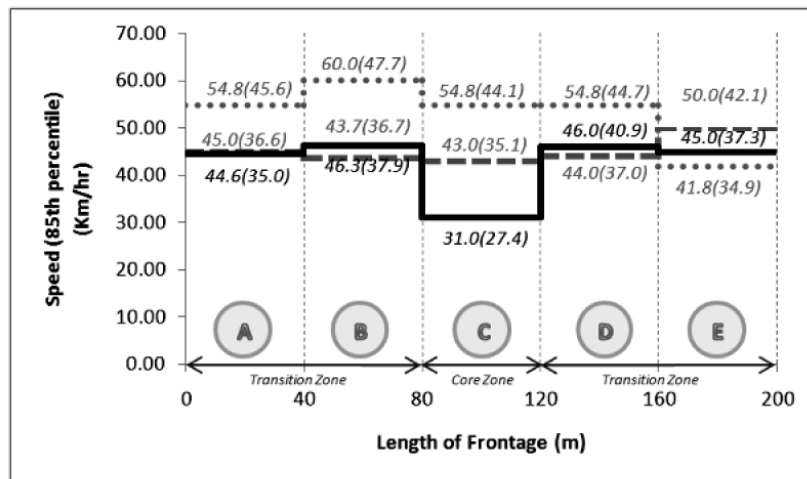
(Figure 5) also illustrated that the pedestrian crossings maneuverings (activity profile) collected during 7:30 and 8:30 AM in the core zone (C) and the transition zones (A, B, D and E) during the before-, the first- and the second-improvement periods. These pedestrian crossings were classified into walking and running maneuvering. As shown in (Figure 7), the percentage of the pedestrian crossings in core zone (C) was increased from 63% (in the before- improvement period) to 91% and approximately 100% in the first- and the second-improvement periods, respectively. In the transition zone (D), the

percentage of the pedestrian crossings was reduced from 30% (in the before-improvement period) to only 1% and 0% in the first- and the second-improvement periods, respectively. In other remaining zones, the percentages of the pedestrian crossings were very low and relatively unchanged during those periods. The results clearly show that the principal achievement of the applications of the EAM concept in gathering as many as pedestrian crossings in core zone (with lower target speeds) and minimizing such crossings in transition zone (with high traffic speeds).

(a) East-bound direction

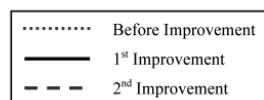


Activity profile



85th Percentile Speed (Average Speed)

Speed profile



(b) West-bound direction

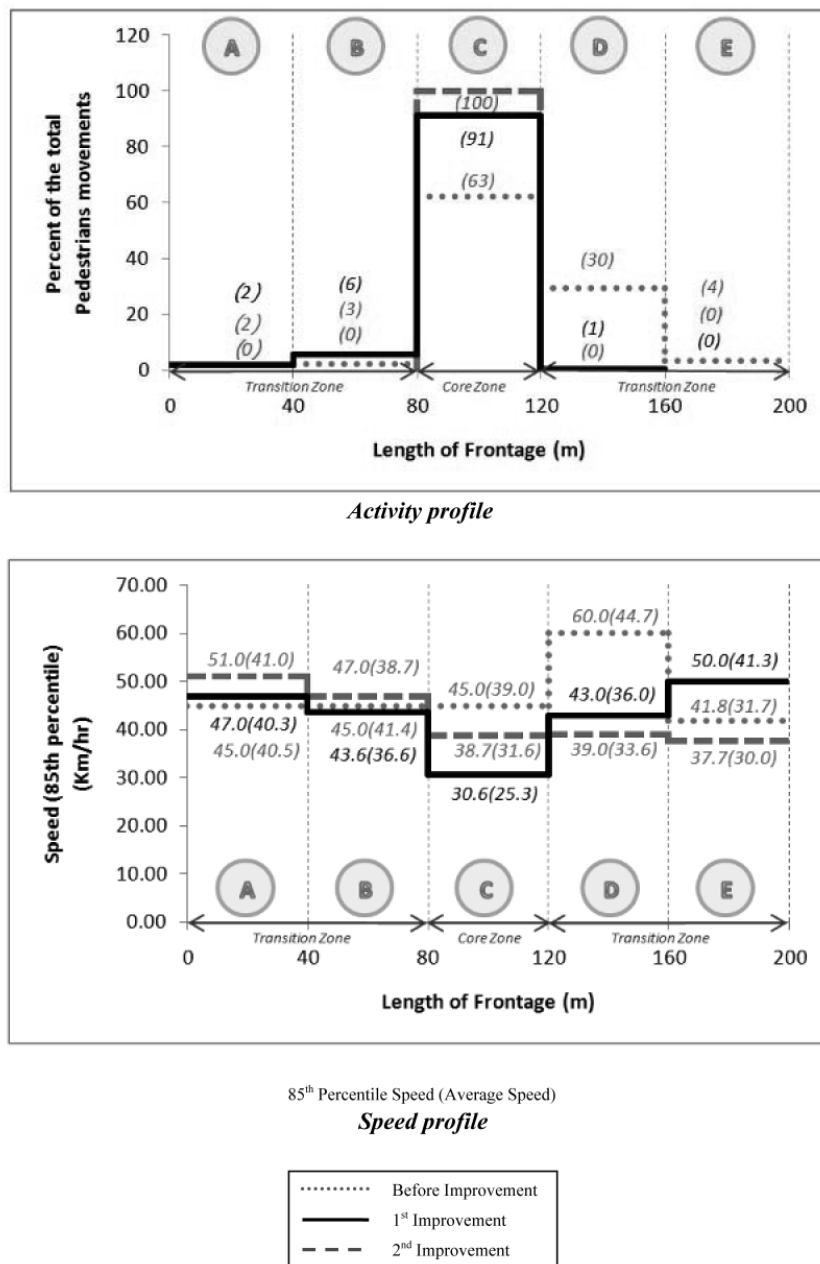


Figure 5 Activity profiles and speed profiles by traffic directions during the before-, the first, and the second-improvement periods

The comparative evaluation in various performance aspects (during the before-improvement, the first-improvement and the second-improvement periods) was summarized in (Table 2). The percentage of jay runners in core zone was slightly reduced from 28.0 % in the before-improvement period) to 25.6 % and 24.0% (in the first- and the second-improvement periods, respectively). The rating score of the Environmental Sensitivity (ES) index for pedestrian safety⁸ was improved from 'high' (in the before-improve-

ment period) to 'medium' (in both the first- and the second-improvement periods). Based on the Song et al's model^{2,3}, pedestrian accident risk for both the before-improvement and the first- and the second-improvement periods is calculated as 2.18×10^{-5} (high risk) and 1.51×10^{-5} (medium risk) and 2.04×10^{-5} (high risk), respectively. It should also be noted that even though the traffic volumes in the first- and the second-improvement periods considerably increased, the pedestrian accident risk is safer than that

in the before-improvement period. This is because the vehicular speed is reduced dramatically according to the installation of a speed hump and time required to cross the shorter effective walked distance of approximately 10.0 m. (post) compared to 16.5 m. (pre) for pedestrians was decreased dramatically. However, it is important to

note that based on the calculated pedestrian accident risk, the pedestrian safety during the second-improvement period performed lesser degree of success compared to the first-improvement period. Based on the extensive people interviews, the perceived safety, esthetics, and landscaping aspects were significantly improved.

Table 2 The comparative evaluation of various performance aspects

Objective	Performance Indicators	Level of achievement of the project			
		Before Improv.	1 st Improv.	2 nd Improv.	Remarks
Reduction in conflicts between pedestrians and vehicles	-Traffic volume in core zone (veh/h)	1,187	1,602	1,754	Average in both directions.
	-Vehicle speed (85 th percentile in core zone (km/hr)	50	31	42.1	Average in both directions.
	-Pedestrian crossings in core zone (ped./h/100 m)	625	696	695	Average in both directions.
	-Jay runners in core zone (%)	28.0	25.6	24.0	Average in both directions.
	-ES for pedestrian safety	High	Medium	Medium	Based on ESM concept
	-Pedestrian accident risk	2.18×10^{-5}	1.51×10^{-5}	2.04×10^{-5}	Based on Song's model
Improvement in quality of the environment	-Footpath width (m)	2.0	3.5	3.5	
	-Median width (m)	1.5	2.0	2.0	
	-Effective Crossing distance (m)	18.0	12.0	12.0	

Conclusions

The conflicts between pedestrians and vehicle movements on a collector road in front of the KKU complex building were mostly recognized as problematic and required the suitable traffic-calming scheme to alleviate the problem. According to the ESM method, the pedestrian accident risk in that area was critical. The EAM was consequently applied to the case study area. Based on the field surveys, the applications of the EAM could potentially and effectively mitigate the traffic accident risk, maintain the environmental and amenity quality and enhance the acceptability of the affected stakeholders in terms of esthetics and landscaping. This concept can also be applied to other similar situations. The improved collector road performed well in reducing the vehicle and pedestrian conflicts. The EAM is an effective measure to manage potential pedestrian-vehicle accident risk on a

collector road. The recent road modification (in the second-improvement period) showed lesser degree of success in calming the traffic speed while traffic volumes and pedestrian crossings increased dramatically.

References

- [1] RTA., "Sharing the Main Street: Practitioners' Guide to Managing the Road Environment of Traffic Routes Through Commercial Centres", Roads and Traffic Authority (RTA) of New South Wales and Federal Office of Road Safety, 2000.
- [2] Song, L, Black, J & Dunne, M., Environmental capacity based on pedestrian delay and accident risk, *Road & Transport Research*, 2 (3), 40-49, 1993a.
- [3] Song, L, Dunne, M C, & Black, J A., Models of delay and accident risk to pedestrian, In *Transportation and Traffic Theory*, Daganzo, C F (Editor), Elsevier

Science Publishers, 1993b

- [4] Klungboonkrong, P and Woolley, J E., Modelling the Environmental Adaptation of a Collector Road in an Area of High Pedestrian Activity in the City of Khon Kaen, *Journal of Transport Engineering in Australia*, 2003; 9 (1), 25-34.
- [5] O'Brien, A P., Traffic management Opportunities for Town and 'Strip' Centres, *Road & Transport Research*, 3(2), 74-80, 1994.
- [6] Austroads., *Cities for Tomorrow A Guide to Better Practice (Vol. 1) and Resource Document*, 1998
- [7] McLean, A J, Anderson, R W G & Farmer, M J B., Pedestrian Accidents on Arterial Roads, *Proceedings of the AITPM 8th National Conference*, Adelaide, South Australia, Australia, 143-152, 1995.
- [8] Klungboonkrong, P. and Taylor M.A.P., An Integrated Planning Tool for Evaluating Road Environmental Impact, *Journal of Computer-Aided Civil and Infrastructure Engineering*, 14, 335-345.

Static Pile Load Test in Rajamangala University of Technology Khon Kaen Campus

Pongsagorn Pongchompu¹, Sorasak Seawsirikul², Pongsagorn Pongchompu³

Received: 30 June 2015; Accepted: 13 July 2015

Abstract

In this research, static driven pile load tests in Rajamangala University of technology Isan Khon Kaen campus were generally performed to prove that piles are capable of sustaining the ultimate design load. In order to prove test, the pile load test was conducted in two types as follows: 1) Standard Loading Procedure and 2) Cyclic Loading Procedure. The strength of test pile was greater than 240 ksc (Schmidt Hammer). Conventional statics pile load tests in driven piles consisted of constructing a reaction frame, the test pile located center position, then incrementally loading the pile with the hydraulic jack. The reaction frame was anchored by six reaction piles. The test load was measured with load cells and the pile head vertical displacement was measured with strain gauges. The test has been designed to allow safe loading of the pile (Design Load) up to 6 tons and a maximum payload test (Test Load) was equal to twice the payload safely, 12 tons. The test pile in the field (Pile load test) was used to secure that the ratio is equal to 2. Due to that the study cannot be reach to ultimate load it is necessary to predict the ultimate load of driven piles by means of Davission, Mazurkiewicz and Brinch Hansen that is corresponding to data test. Thus, it can be concluded that the piles are capable of sustaining the ultimate design load and the deflection is within allowable levels, the test has proved that the pile is acceptable.

Keywords: driven pile, factor of safety, ultimate load of pile

Introduction

The Pile Load Test was used to test the loading capacity of piles in real practical use. The test was conducted on ten piles at the back of Building 10 at the Rajamangala University of Technology Isan Khon Kaen Campus in order to find the Ultimate Load of the piles. A two number of load patterns were used for Vertical Compression (ASTM D1143-81, Reapproved 1994), which are the Standard Loading Procedure and the Cyclic Loading. The collected data was analyzed and compared by the Static Method for pile design. The Load Test was conducted as shown in the (Figure 1), (Figure 2) and (Figure 3).

Vertical Compression Load Test Installation

The research objective was to investigate the model of a pile load test of driven piles with dimensions of 0.18x0.18x4.00 m. Consisting of anchored pile, new reaction beam with cable. The test set up was as follows;

1. Reaction Beam installation consists of upper beams and lower beams. Both the upper beams and the lower beams use 3 I-Beams each.
2. A steel plate with bolts is used to combine the upper beam and the lower beam.
3. Three small hydraulic jacks are installed to distribute the load from the lower beam to the upper beam. This will reduce a deformation of the lower beam.
4. The Reaction Load to the Reaction Beams is increased by using a concrete block with 4 hollow sections which is used as a safety measure to protect the concrete block from falling down during testing.
5. A sling is used to bind the Anchors and Reaction Beam in order to increase the load efficiency and synchronize the Anchors and Reaction Beam movement. The sling should be installed between the I-Beams to protect the I-Beams from destruction. Part of the reaction force comes from the anchor piles which have 3 piles on

^{1,2,3} Rajamangala University of technology Khonkaen Campus, Khon Kaen E-mail: ppoungchompu@yahoo.com

^{1,2,3} Rajamangala University of technology Khonkaen Campus, Khon Kaen

each side, and each pile has a diameter of 18 x 18 cm. and is 4 m. long.

6. Load Beam Installation: The plate is put on the Test Pile for load distribution. Then the Hydraulic Jack with a load capacity of 30 tons and traveling distance of 10 cm. is put between the plate and the Load Beam.

7. Six Dial Gauges are installed by six people to read the destructiveness of the Test Pile and the movement of the Anchors. Two Dial Gauges are installed at the Test Pile head to measure the destructiveness of the Test Pile head. Two Dial Gauges are each installed on the left and the right Anchors to measure the movement of the Anchors during the test. The Reference Beam is attached to the Dial Gauges with the Support and is installed 2.5 m. from each Anchor.

8. The Loading Pattern in the Standard Loading Procedure and the 30 ton hydraulic is controlled by one person. Each load will be 25% - 200% of the safe loading weight. The weight is only to be increased when the collapsing rate is less than 0.25 mm per hour and takes no longer than two hours. When the test load is increased to the highest level (2 times the safe load weight), it is left for 24 hours. The settlement is recorded throughout every 2 hours. The testing weight is reduced to 75, 50, 25, 10 and 0% of the highest testing weight and the last settlement is recorded at one hour intervals between each recording.

9. The Loading Pattern of the Cyclic Loading Procedure: The process of increasing and reducing the loading weight was divided into steps and the testing was done by using the same steps as per (8) Standard Loading Procedure at loading weights 50, 100, and 150 of the safe load weight. The load weights were left on for 1 hour and the load weights were reduced using the same steps that were used when it was increased. In each phase, they were left on for 20 minutes and when all the weight had been lifted, the weight was once again increased by 50% of the safe load weight each time until the previous load weight had been reached. In each phase, the weight was left on for 20 minutes. During each step, the weight was further increased as per (8) Standard Loading

Procedure. When the highest test level weight had been reached, the weight was pulled out using the same steps as per the test in step (8).

Test result and discussions

From the three testing methods for finding Pile Bearing Capacity, the data of Deflection and Rebound Deflection passed the limitation of Residual Deflection at 6 mm. after maintaining the maximum load for 24 hours.

Destruction of the pile resulted from the destruction of the soil, which occurred under the conditions in which the pile had excessive deflection under a small increase in weight. In the past, the definition of Ultimate Load has been a load that causes a deflection to more than 10 percent of the pile diameter. Based on the Static pile load test conducted at Building 10 with piles of 0.18 m. diameter and 4 m. long, Standard loading procedure and Cyclic load test were performed as shown in (Figure 4) and (Figure 5).

In the comparative study, the relationship between results vertical pile load test was evaluated by 3 methods which are as follow;

1. Load Failure using The Davisson Method (1972) as shown in (Figure 6), which shows that the Pile Load Test result is relevant to the theory of Davisson with an Ultimate Load of 10.90 tons.

2. Load Failure by The 90% Brinch Hansen Method as shown in (Figure 7), which shows that the Pile Load Test result is relevant to the theory of Brinch Hansen with an Ultimate Load of 10.08 tons.

3. Load Failure utilizing the Mazurkiewicz Method as shown in (Figure 8), which shows the prediction by equally dividing the Deflection and finding the cross point which will achieve an Ultimate Load of 10.08 tons.

The Vertical Ultimate Load from the Pile Load Test compared with the safety load (6 tons per pile) shows the following: 1) the Davisson Method gave a Safety Ratio of 1.82, 2) the 90% Brinch Hansen Method gave a Safety Ratio of 1.68, 3) the Mazurkiewicz Method gave a Safety Ratio of 2.05, and 4) the Static Method gave a Safety Ratio of 1 as shown in (Figure 9).

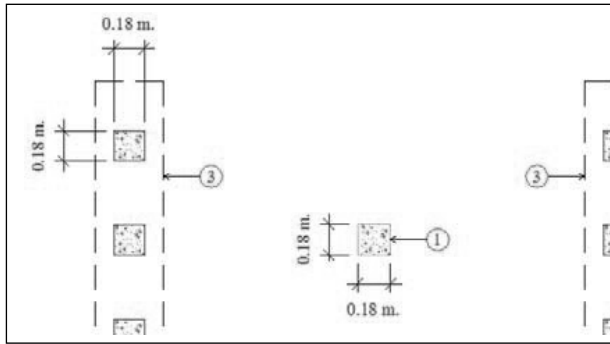


Figure 1 Test set up (top view)

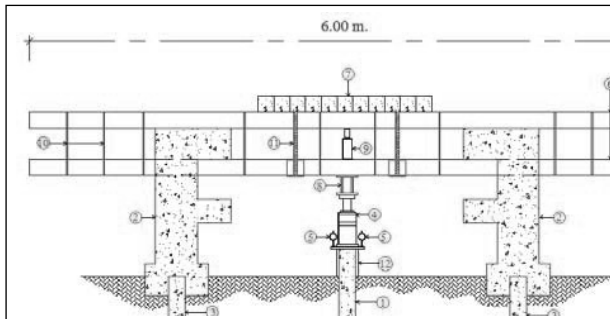


Figure 2 Test set up (front view)

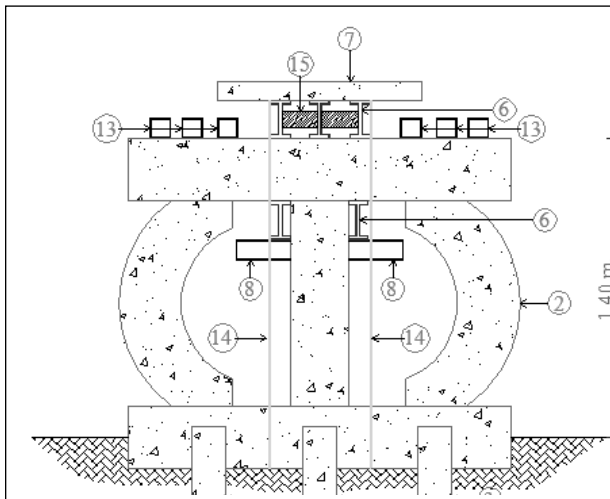


Figure 3 Test set up (side view)

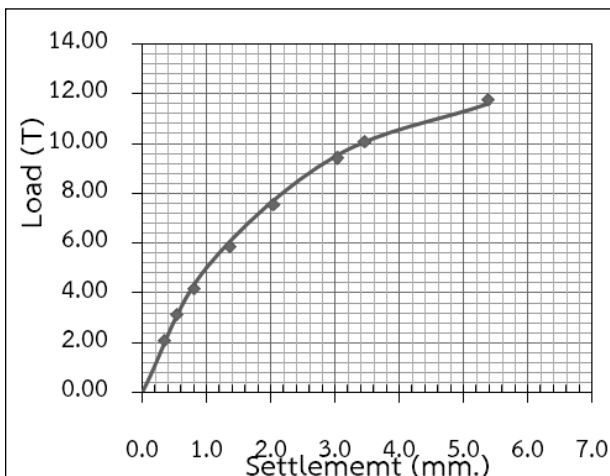


Figure 4 Load-settlement curve for standard loading test.

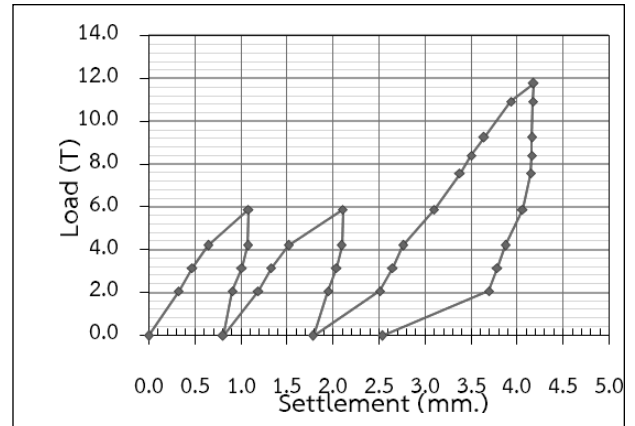


Figure 5 Load-settlement for cyclic loading test

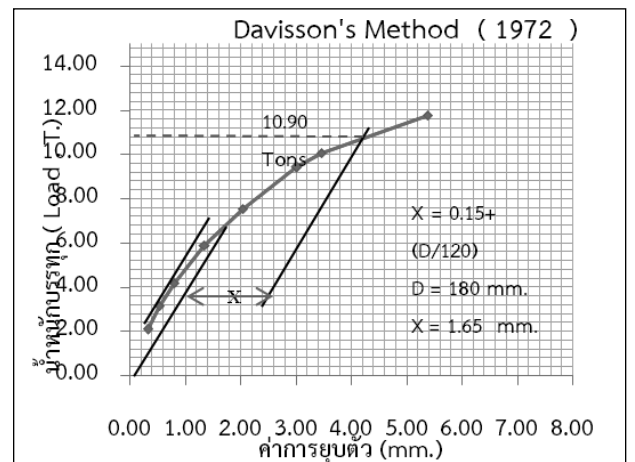


Figure 6 Davisson 's method

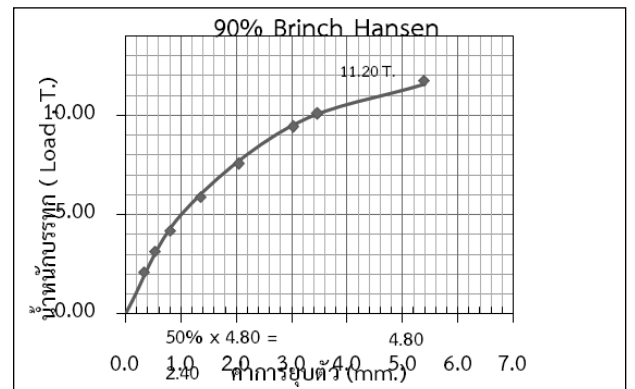


Figure 7 90% Brinch Hasen 's method

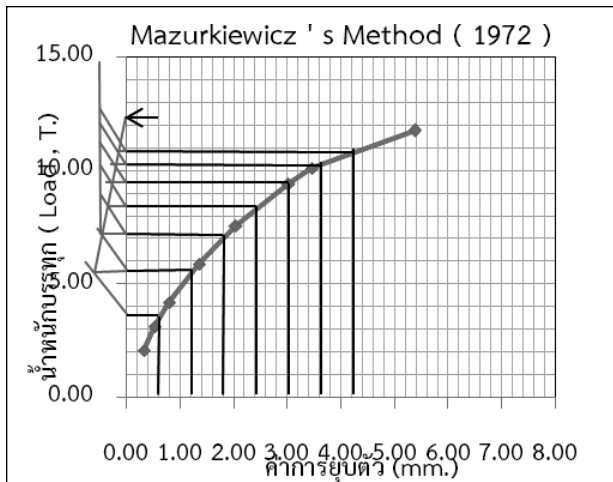


Figure 8 Mazurkiewicz 's method

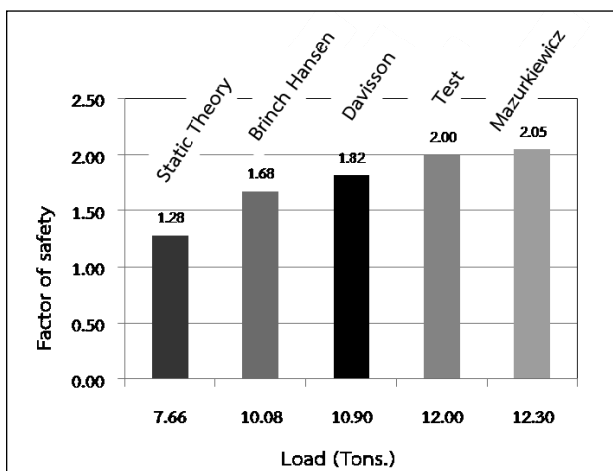


Figure 9 Factor of safety

Conclusion

The Pile Load Test was used to test the loading capacity of piles in real practical use. By using Vertical Compression (ASTM D1143-81, Reapproved 1994) which includes the Standard Loading Procedure and the Cyclic Loading Test, testing was conducted on a square pile with a section of 18 x 18 cm. and 4.00 m. long at the back of Building 10 at the Rajamangala University of Technology Isan Khon Kaen Campus

The first Vertical Load Test results were compared to the Vertical Ultimate Load and Safety Ratio during the field Pile Load Test, and the predictions made by the Static Pile Load Test were in the same cluster. As for the Static Method, the result was lower than the two methods mentioned above and the test pile with a section of 18 x 18 cm. and 4.00 long was able to sustain the designed Ultimate Load without Load Failure. The Cyclic

Load Test was compared to the code which allowed for maximum Deflection at Bearing Load of 0.25 mm. per hour and maximum Deflection of 6 mm. after the 24 hour load test. The result was that the pile was able to sustain the load no more than the limitation.

Acknowledgement

Acknowledgement is to Rajamangala University of technology Isan Khon Kaen campus that supported the research.

References

- [1] Terzaghi, K. 1943, Theoretical Soil Mechanics, Wiley, New York.
- [2] Tomlinson, M.J. 1957, "The adhesion factor of pile driven in clay soils", Proc. 4th International Conference on Soil Mechanics and Foundation Engineering, 1957;2:66-71
- [3] Vesic, A.S. 1967, "Investigation of bearing capacity of piles in sand", Proceedings of North American Conference on Deep Foundations, Mexico City, 1967;1:197-224
- [4] Horpibulsuk, S. 2009, Foundation Engineering, Top publishing, Thailand.
- [5] Nanegrungsunk, B. 2009, Foundation Engineering and Tunnelling, Top publishing, Thailand.
- [6] Gasaluk, W. 2010, Shallow Foundation, The Engineering institute of Thailand under H.M. The King 's Patronage.

Experimental Investigation of Closed Loop Oscillating Heat Pipe at Startup Condition

Surain Promdan¹, Phrut Sakulchangsatjatai¹, Niti Kammuang-lue¹ and Pradit Terdtoon¹

Received: 11 June 2015; Accepted: 13 July 2015

Abstract

The objective of this paper is to investigate startup conditions of a closed loop oscillating heat pipe (CLOHP). The CLOHP are made of a long copper capillary tube with an inner diameter of 2.03 mm. The number of turns was 4, 5 and 7. The ends of the tube are connected to complete the loop. The evaporator, adiabatic and condenser sections are all an equal length of 50 mm. R123, acetone and water were used as the working fluids with a 50% filling ratio. The CLOHP was operated horizontally and the condenser temperature was controlled at 25 °C. A low-voltage high-current heater was used as the heat source and the cooling medium was a solution of water and ethylene-glycol with a 1:1 mixing volume ratio. The number of turns is 7, changing the working fluid between R123, acetone and water, it was found that the heat transfer rate increases from 5.72 W using R123 as working fluid, to 7.35 W and 14.71 W using acetone and water as working fluids, respectively. The frequency of the working fluid decreased from 0.94 cycle/s using R123 as working fluid, to 0.65 cycle/s and 0.19 cycle/s using acetone and water as working fluids, respectively. The amplitude increased from 0.36 °C using R123, to 0.55 °C and 3.62 °C using acetone and water, respectively. In the case of using water as working fluids, changing the number of turn from 4 to 5 and 7 turns, it was found that the heat transfer rate increased from 11.43 W using 4 turns, to 12.25 W and 14.71 W using 5 and 7 turns, respectively. The frequency did not change switching to 5 turns but did change from 0.18 cycle/s to be 0.19 cycle/s when using 7 turns. The amplitude increased from 2.35 °C using 4 turns, to 3.24 °C and 3.62 °C using 5 and 7 turns, respectively.

Keywords: closed-loop oscillating heat pipe, startup condition

Introduction

A Closed Loop Oscillating Heat Pipe (CLOHP) is a type of heat exchanger. It is constructed by bending a capillary tube in an undulating bundle of a tube connecting both ends together to form a closed loop¹. Heat is transferred by the oscillation of working fluid inside the CLOHP. Nowadays, modern technology usually consists of smaller in size and higher in performing electronic devices. A consequence of this is considerably high heat accumulation in these devices as well as decreasing surface area for heat dissipation. Because of the very high heat generation and limited heat sink area, CLOHP are utilized and installed onto electronic circuits for heat management. However, there are studies showing the oscillating heat pipe cannot start to operate in some cases². This can cause failure in

the device, e.g. a decrease in working hours and performance.

CLOHPS were investigated in many previous studies. One main aspect of a quantitative study³ was concerned with the effect of tube geometry and the type of working fluid on heat transfer rates. But a qualitative study was concerned with the effect of tube geometry, type of working fluid, and filling ratio on internal flow pattern inside CLOHP.

The modeling and theoretical analysis of the startup of an oscillating heat pipe shows the effects of the evaporator surface roughness and superheated temperature necessary to make the CLOHP operate properly at normal conditions. But in some cases, the CLOHP cannot startup, even if the superheated level is

¹ Department of Mechanical Engineering, Faculty of Engineering, Chiang Mai University, Chiang Mai, Thailand 50200.
E-mail: surapin_me@hotmail.com

reached^{4,5}. However, a basic concept of startup conditions and a mathematical model to predict operation of the CLOHP was already established⁶. It is found that the point at which a CLOHP can start takes place when replacement mechanism of the inside working fluid is possible. This mechanism occurs when net condensation rate of vapor plugs is higher than net evaporation rate of vapor plugs. But there are a few studies about the effect of parameters on the approach to steady state of CLOHP. Therefore, this study focuses on quantitative experiments to obtain the startup condition at which the working fluid inside the CLOHP start to operate.

Materials and Methods

The CLOHP was made of a long copper capillary tube with the inner diameter of 2.03 mm and the turns was 4, 5 and 7 turns. The ends were connected to close the loop. The evaporator, adiabatic and condenser section were all an equal length of 50 mm. R123, acetone and water were used as the working fluids with a 50% filling ratio.

1. Experimental setup and procedure

“(Figure. 1)” shows the experimental equipment. The CLOHP were filled with a working fluid by filling machine. Thermocouples were attached to the heat pipe at 10 points on the middle of each tube of the evaporator section (T_{e_1} - $T_{e_{10}}$), 4 points on the adiabatic section (T_{a_1} - T_{a_4}), and 4 points on the condenser section (T_{c_1} - T_{c_4}). The CLOHP was then set up with another experimental instrument. Thermocouples were attached at the inlet and outlet positions of the cooling jacket and then connected to relay information to the data logger for analysis. The AC high current supply was connected, the cold bath was adjusted to a temperature of 25°C, and the flow rate of cooling medium was adjusted, using a ball valve, to about 0.15 kg/min. After this, heat was supplied to the evaporator section continuously, the voltage was adjusted (one step increasing of the Variac can increase temperature of the evaporator section approximately one or two °C), and the temperature data was recorded. During the recording of data from the experiment, the temperatures at the evaporator and condenser sections

were observed while the voltage was slightly increased until the CLOHP started up. Then the amplitude and frequency after start up were defined (amplitude $\geq 0.2^\circ\text{C}$, frequency ≥ 0.1 Hz). Before repeating the experiment, all experimental components were paused for 60 minutes or until all measured temperature points were equal to the ambient temperature.

The heat transfer rate of the cooling medium in the condenser section is calculated by substituting an inlet and outlet cooling medium temperature as shown in the following equation.

$$Q = \dot{m}c_p(T_{out} - T_{in}) \quad (1)$$

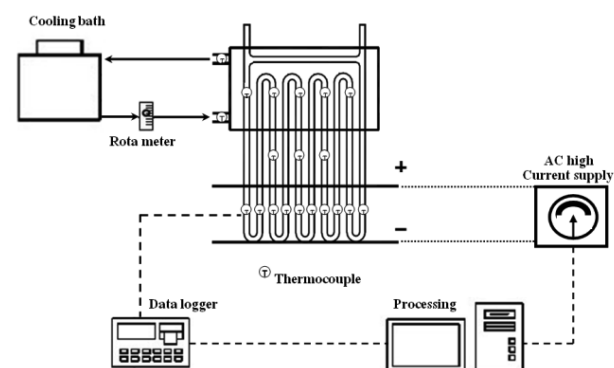


Figure 1 The whole experimental setup

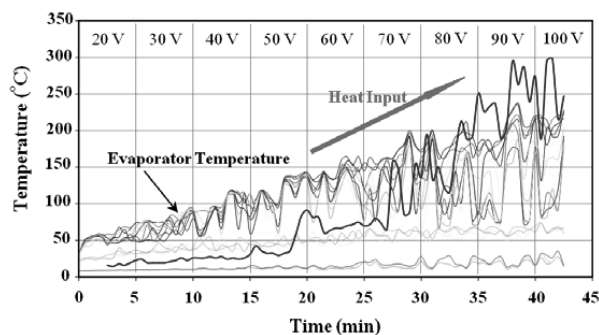
2. Definition of startup condition

Since there is no quantitative definition of operational startup criteria, the definition used in this study considered the fluctuation of working fluid temperature. The CLOHP is defined to start its operation when the fluctuating amplitude of temperature is greater than or equal to 0.2°C and the fluctuating frequency of temperature is greater than or equal to 0.1 Hz. If these conditions are not met, the CLOHP is defined as unable to start transferring heat. The fluctuating amplitude and frequency of working fluid inside CLOHPs are measured using thermocouples, which are attached on the outer surface of the evaporator, adiabatic and condenser sections.

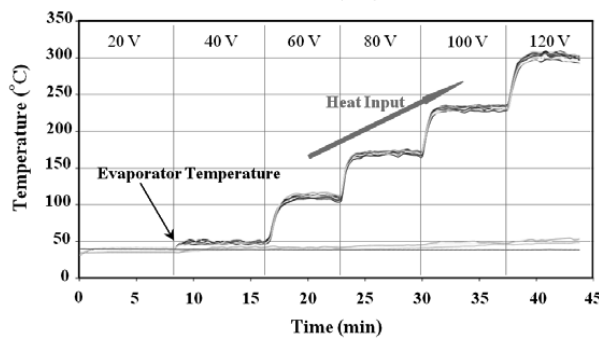
From (Figure 2(a)), it can be seen that the CLOHP starts its operation. When electrical voltage increases to 20 Variac (“Variac” in this study is a scale used in the voltage or current adjustment of the AC high current transformer) or the CLPHP is supplied with a

higher input heat, the evaporator section temperature increases during the 1 to 3 minutes but there is no fluctuation of working fluid temperature. Therefore, the CLOHP does not operate during this time. After 3 minutes to find the fluctuation of working fluid temperature within the evaporator section, the amplitude and frequency are in the defined range. Thus, this is defined to be a point at which the CLOHP starts its operation. After the

CLOHPs can normally transfer the heat. When electrical voltage increases from 20 Variac up to 100 Variac, will find that the fluctuation of working fluid temperature within the evaporator section to a wider range and the heat transfer is increased as well. In addition, heat transfer rate measured in the startup condition is very low compared with a case of the normal operating state.



(a) The CLOHP starts its operation



(b) The CLOHP cannot operate

Figure 2 Increase of evaporator and condenser section temperature with appropriate startup conditions

(Figure 2(b)) shows the non-working CLOHP.

Increasing the heat at the evaporator section, and fluid cannot flow to the evaporator section. Thus the replacement and circulation of working fluid cannot take place because all of the working fluid is evaporated from the increasing activity in the evaporator. This is called dryout. This dryout affects increasing temperature at the evaporator section so that the CLOHP cannot operate, and there is no heat transfer.

Results and Discussions

All results show the relationship between the heat transfer rate, frequency and amplitude, on the effect of closed loop oscillating heat pipes (CLOHP) at startup conditions. For each frequency and amplitude is calculated by the program⁷.

1. Effects of working fluids

The investigated CLOHP had an inner diameter of 2.03 mm, evaporator lengths of 50 mm, and was 4, 5 and 7 turns. R123, acetone and water were used as working fluids with latent heat of 161, 501 and 2386 kJ/kg respectively. (Figure 3) shows the effect of working fluids on the startup conditions of CLOHP. (Figure 3(a)) shows effect of heat transfer rate on the working fluids with 7 turns. Changing the working fluid between R123, acetone and water, it is found that the heat transfer rate increases from 5.72 W using R123 as working fluid, to 7.35 W and 14.71 W using acetone and water as working fluids, respectively. (Figure 3(b)) shows the effect of frequency on the working fluids, it is found that the frequency of the working fluid decreases from 0.94 cycle/s using R123 as working fluid, to 0.65 cycle/s and 0.19

cycle/s using acetone and water as working fluids, respectively. (Figure 3(c)) shows effect of amplitude on the working fluids, it is found that the amplitude increases from 0.36 °C using R123, to 0.55 °C and 3.62 °C using acetone and water, respectively.

A working fluid with high latent heat needs more than heat to change phase from liquid to vapor,

when compared with the same weight. As a result, heat transfer rate, Amplitude increase and Frequency decrease at startup conditions. It is consistent with the previous study^{7,8}, when decreasing the working fluid's latent heat causes collapsing ratio of vapor slugs in condenser section increases, the CLOHP's can be easier obtained.

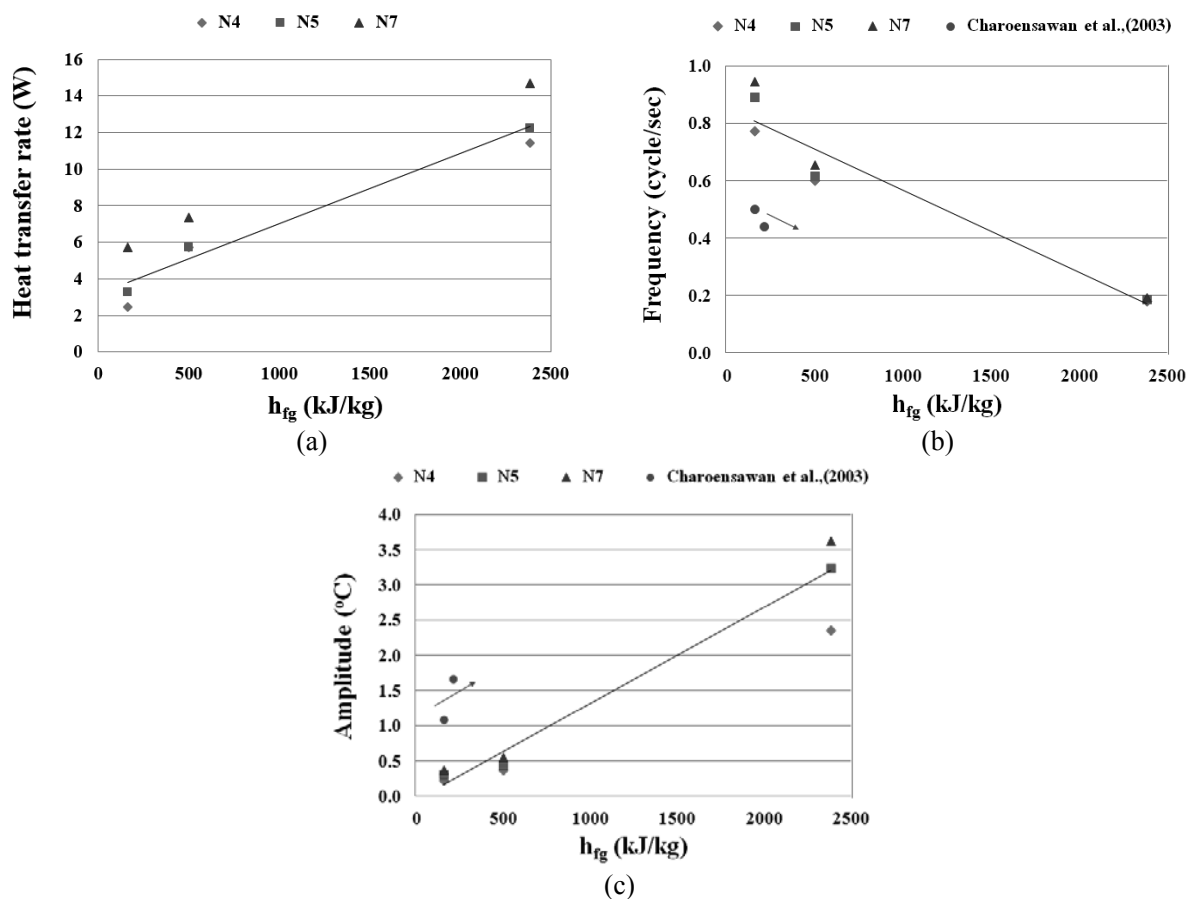


Figure 3 Effect of working fluids on the startup of CLOHP

(a) Heat transfer rate (b) Frequency (c) Amplitude

2. Effects of number of turns

The investigated CLOHP had an inner diameter of 2.03 mm, evaporator lengths of 50 mm, and was 4, 5 and 7 turns. R123, acetone and water were used as working fluids with latent heat of 161, 501 and 2386 kJ/kg respectively. (Figure 4) shows the Effect of number of turns on startup conditions. (Figure 4(a)) shows the effect of heat transfer rate on the number of turns, In case of using water as working fluid, changing the number of turn from 4 to 5 to 7 turns, it was found that the heat transfer

rate increases from 11.43 W using 4 turns, to 12.25 W and 14.71 W using 5 and 7 turns, respectively. (Figure 4(b)) shows the effect of Frequency on the number of turns, it is found that the frequency of the number of turns does not change switching to 5 turns but does change from 0.18 cycle/s to 0.19 cycle/s when using 7 turns. (Figure 4(c)) shows the effect of Amplitude on the number of turns, it is found that the amplitude increases from 2.35 °C using 4 turns, to 3.24 °C and 3.62 °C using 5 and 7 turns, respectively.

The increase of number of turns is the same as the increase in the heat transfer area. As a result, the heat transfer rate, Frequency and Amplitude increase at

startup conditions. This is consistent with the previous study^{8,9}.

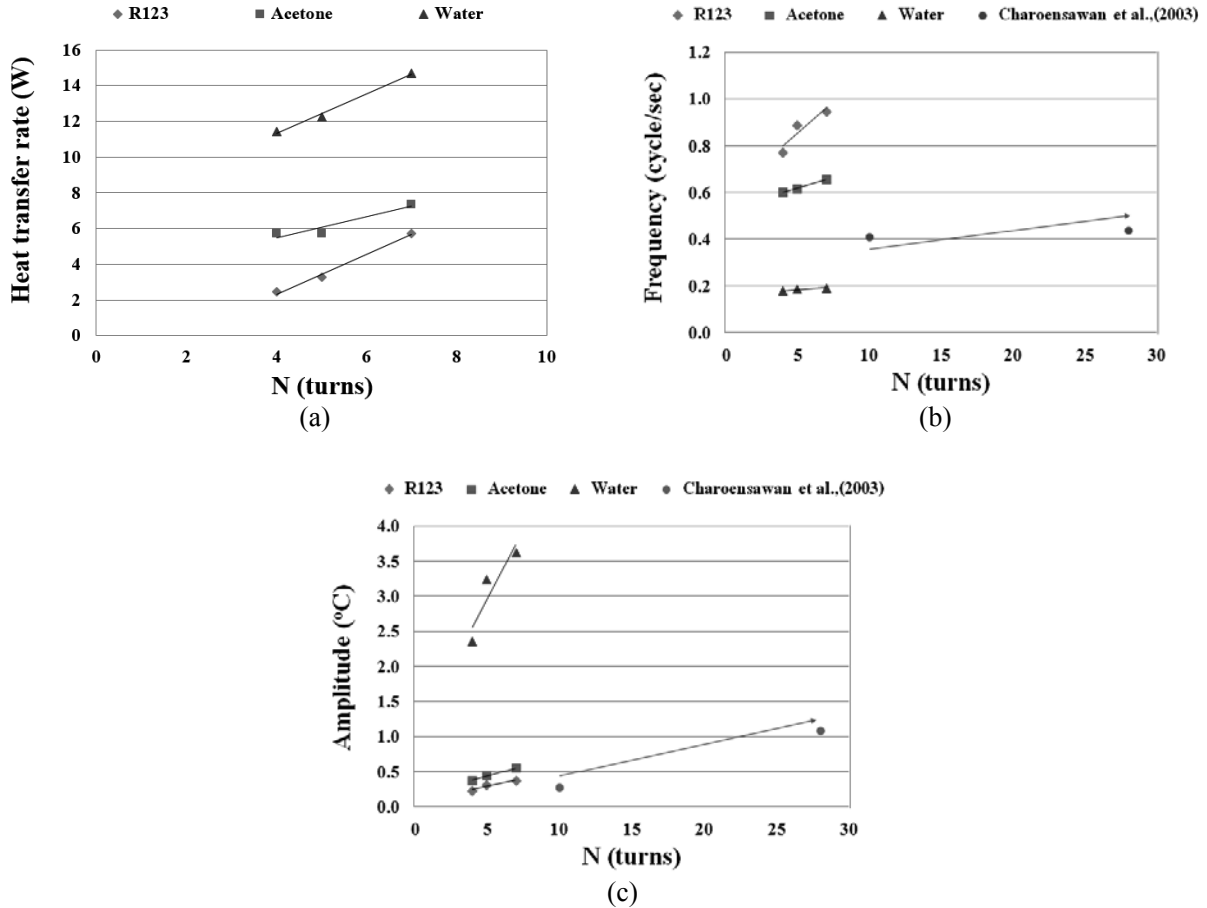


Figure 5 Effect of number of turns on the startup of CLOHP
 (a) Heat transfer rate (b) Frequency (c) Amplitude

Further work should be extended to study the internal flow patterns on startup condition in CLOHP. This application could be useful for the entire operation.

Conclusion

From this experimental investigation of a closed loop oscillating heat pipe at startup condition, it can be concluded that, when the number of turns is 7 and, changing the working fluid between R123, acetone and water:

- The heat transfer rate increases from 5.72 W using R123 as working fluid, to 7.35 W and 14.71 W using acetone and water as working fluids, respectively.
- The frequency of the working fluid decreases

from 0.94 cycle/s using R123 as working fluid, to 0.65 cycle/s and 0.19 cycle/s using acetone and water as working fluids, respectively.

- The amplitude increases from 0.36 °C using R123, to 0.55 °C and 3.62 °C using acetone and water, respectively.

In case of using water as working fluid, changing the number of turn was 4 to 5 to 7 turns, it was found that.

- The heat transfer rate increases from 11.43 W using 4 turns, to 12.25 W and 14.71 W using 5 and 7 turns, respectively.
- The frequency of the number of turn does not change when switching to 5 turns but does

change from 0.18 cycle/s to be 0.19 cycle/s when using 7 turns.

- The amplitude increases from 2.35 °C using 4 turns, to 3.24 °C and 3.62 °C using 5 and 7 turns, respectively.

It can be noted that working fluid with low latent heat and low number of turns, allows the CLOHP to start easily, which can be observed by the heat transfer rate, frequency and amplitude.

Acknowledgement

This research has been supported by Heat Pipe and Heat System Laboratory and Graduate School of Chiang Mai University and has been conducted at Rajamagala University of Technology Lanna (LMUTL), Thailand. The authors would like to express their sincere appreciation for all of the support provided.

References

- [1] Maezawa, S.(2000). Heat Pipe : Its Origin, Development and Present Situation. Procs. of the 6th International Heat Pipe Symposium 2000, Chiang Mai, Thailand.
- [2] Charoensawan, P. and Terdtoon, P. Thermal performance of horizontal closed-loop Oscillating Heat Pipes, *Applied Thermal Engineering*, 2008; 28: 460.
- [3] Charoensawan, P., Khandekar, S., Groll, M. and Terdtoon, P., Closed Loop Pulsating Heat Pipe Part A: Parametric Experimental Investigations. *Applied Thermal Engineering*. 2003.
- [4] Qu, W. and Ma, H.B., Theoretical analysis of startup of a pulsating heat pipe, *International Journal of Heat and Mass Transfer*, 2007; 50, 11-12, 2309-2316.
- [5] Xu, J.L. and Zhang, X.M. Start-up and steady thermal oscillation of a pulsating heat pipes, *Heat Mass Transfer*, 2005; 41, 685-694.
- [6] Sophonpipat, N., Sakulchangsajatai. P., Saiseub, M. and Terdtoon,P., Time Response Model of Operational Mode of Closed Loop Oscillating Heat Pipe at Normal Operating Heat pipe. Procs. of the 8th International Heat Pipe Symposium. Kumamoto Japan., 2006: 291-296.
- [7] Promdan, S., Sakulchangsajatai, P., Kammuang-lue, N., and Terdtoon, P., (2013). Effects of Working Fluid on Startup Conditions of Closed Loop Oscillating Heat Pipes, *The Fifth International Conference on Science, Technology and Innovation for Sustainable Well-Being (STISWB V)* , Luang Prabang, Lao PDR.
- [8] Charoensawan, P., Terdtoon, P., Tantakom, P., and Ingsuwan, P., Effect of Evaporator Section Lengths, Number of Turns and Working Fluid on Internal Flow Patterns of a Vertical Closed-Loop Oscillating Heat Pipe. Procs. of the 7th International Heat Pipe Symposium. Jeju Korea., 2003; 360-367.
- [9] Promdan, S., Sakulchangsajatai, P., Kammuang-lue, N., and Terdtoon, P., An Approach for Identify the Steady State of Closed Loop Oscillating Heat Pipes, *The 6th International Conference on Science, Technology and Innovation for Sustainable Well-Being (STISWB VI)* , Kingdom of Cambodia. 2014; 687-693, 1989.

Thermal Performance Enhancement in a Heat Exchanger Square-Duct With V-Shaped Fins Vortex Generator

Supattarachai Suwannapan^{1*}, Suriya Chokphoemphun², Panuwat Hoonpong³, Pongjet Promvonge⁴

Received: 12 June 2015; Accepted: 13 July 2015

Abstract

The article presents an experimental study on thermal performance enhancement in a constant heat-fluxed square-duct inserted diagonally with V-shaped fins vortex generator. The experiments were carried out by varying the airflow rate through the tested square-duct with V-shaped fins inserts for Reynolds number from 4000 to 25,000. The effect of the V-shaped fins with V-tip pointing downstream at various relative fin pitches on heat transfer and pressure drop characteristics was experimentally investigated. Both the heat transfer and pressure drop were presented in terms of Nusselt number and friction factor, respectively. Several V-shaped fins characteristics were introduced such as fin pitch to duct height ratios or pitch ratios, ($P/H=PR=0.5, 1.0, 1.5, 2.0, 2.5$ and 3.0), fin to duct height ratio or blockage ratio, ($e/H=BR=0.2$) and fin attack angle, ($\alpha=45^\circ$). The experimental results reveal that the heat transfer and friction factor values for the V-shaped fins inserts increase with the decrement of PR. The inserted square-duct for $BR=0.2$ at $PR=0.5$ provides the highest heat transfer and friction factor but the one at $PR=1.5$ yields the highest thermal performance.

Keywords: thermal performance, heat exchanger, V-shaped fins, vortex generator, heat transfer

Introduction

Originally, heat exchangers were introduced using a plain or smooth surface. Then, an improvement was developed using several heat transfer enhancement devices. In the past, many researchers studied the effects of turbulator or swirl/vortex generator devices on heat transfer, pressure drop and thermal performance behaviors in pipe/duct heat exchanger. Liu et al.¹ experimentally studied on heat transfer characteristics in steam-cooled rectangular channels with two opposite rib-roughened walls. They reported that the average Nusselt number for the channel with $\alpha=45^\circ$ was higher than $\alpha=60^\circ$. Promvonge et al.² studied the turbulent flow and heat transfer characteristics

in a square duct fitted diagonally with 30° angle-finned tapes. Promvonge et al.³ numerically investigated on laminar flow and heat transfer characteristics in a three-dimensional isothermal wall square-channel fitted with inline 45° V-shaped baffles on two opposite walls. It was apparent that the longitudinal counter-rotating vortex flows created by the V-baffle can induce impingement/attachment flows over the walls resulting in greater increase in heat transfer over the test channel. Singh et al.⁴ experimentally investigated the heat and fluid flow characteristics of rectangular duct having one broad wall heated and roughened with periodic discrete V-down rib. Tanda⁵ experimentally investigated the forced convection

¹ Department of Mechanical Engineering, Faculty of Engineering, Rajamangala University of Technology Isan, Khonkaen Campus, 150 Srichan Road, Muang, Khonkaen, 40000, Thailand

² Major of Mechanical Engineering, Faculty of Industry and Technology, Rajamangala University of Technology Isan, Sakonnakhon Campus, 193 Phangkhon-Waritchaphum Road, Phangkhon, Sakonnakhon, 47160, Thailand

³ Department of Mechanical Technology, Faculty of Industrial Technology, Thepsatri Rajabhat University, 321 Naraimaharat Road, Talaychubsorn, Lopburi, 15000, Thailand

⁴ Department of Mechanical Engineering, Faculty of Engineering, King Mongkut's Institute of Technology Ladkrabang, Bangkok, 10520, Thailand

* Corresponding author, E-mail address: oak_su@hotmail.com Tel.: +66 43-338-869-70; fax: +66 43-338-869-70

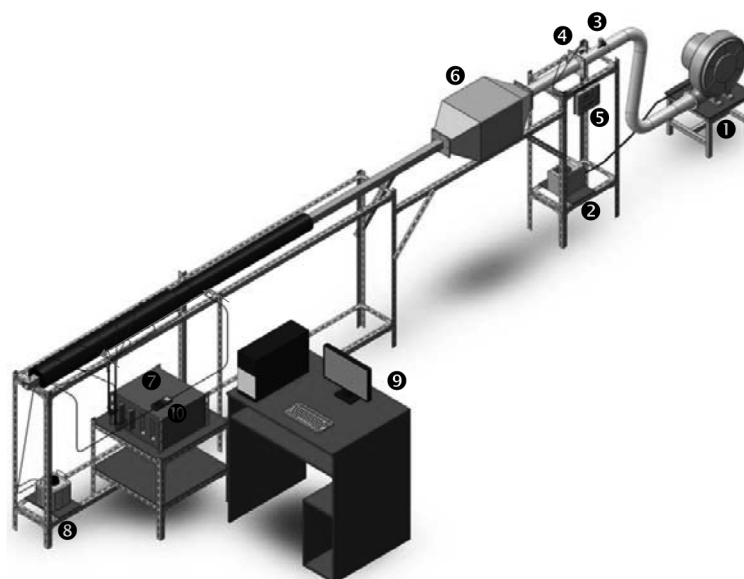
heat transfer in a rectangular channel with inclined 45° angled rib turbulators. Hans et al.⁶ experimentally investigated the effect of multiple V-rib roughness on heat transfer coefficient and friction factor in an artificially roughened solar air heater duct. Khan et al.⁷ experimentally studied the heat transfer augmentation in developing turbulent flow through a ribbed square duct. Momin et al.⁸ experimentally investigated the effect of geometrical parameters of V-shaped ribs on heat transfer and fluid flow characteristics of rectangular duct of solar air heater with absorber plate having V-shaped ribs on its underside.

In the present work, the study on thermal performance enhancement in a heat exchanger square-duct with V-shaped fins inserts has never been reported. These V-shaped fins acted as a vortex generator to create a vortex flow inside the duct. The result could lead to an increase in heat transfer rate. However, the pressure loss would be increased. Therefore, in order to yield the optimum thermal performance, the designed parameters

which are shape, size, height, angle and pitch of the vortex generator are studied to investigate their effects on the heat transfer and flow friction.

Materials and Methods

A schematic diagram of the experimental setup is presented in (Figure 1). The system consists of a high-pressure blower, an orifice flow meter, a settling tank, and a square duct test section. The overall length of the duct was 3000 mm comprised an entrance section of 2000 mm and a test section of 1000 mm (L). The test section in square duct was made of aluminum plate having thickness of 3 mm. and a cross sectional area of $45 \times 45 \text{ mm}^2$ (H×H). (Figure 2) shows the V-shaped fins placed on a double-sided aluminum frame. The V-fin's geometries were fin-to duct-height ratio or blockage ratio, ($e/H=BR=0.2$), fin pitch to duct height ratio, ($P/H=PR=0.5, 1.0, 1.5, 2.0, 2.5$ and 3.0) and fin attack angle, $\alpha=45^\circ$ with V-tip pointing downstream (called "V-downstream")



(1) blower, (2) inverter, (3) control valve, (4) orifice plate, (5) inclined manometer, (6) settling tank, (7) data logger, (8) variac transformer, (9) personal computer, (10) digital differential pressure.

Figure 1 Schematic diagram of experimental apparatus.

The AC power supply provided energy for heating four walls of the test section and maintaining a uniform surface heat flux condition. Air as the working fluid was forced through the system by a 1.45 kW high-pressure

blower. An inverter was used to control the air flow rate. The flow rate was measured by using an orifice plate. The orifice plate was calibrated by hot wire and vane-type anemometers. The pressure drop across the orifice was

measured using an inclined manometer. The axial temperature distributions along the test section were measured by twenty-eight thermocouples. Two thermocouples were positioned at the entrance and the exit of the duct to measure the inlet and outlet temperatures. All measured temperature values were fed into a data logger (Fluke 2650A) and recorded via a personal computer. Two static pressure taps were located at the top walls to measure axial pressure drops across the test section.

This pressure drop was determined to calculate the friction factor. The pressure drop was measured by a digital differential pressure transducer.

The uncertainty analysis in the data calculation was based on⁹. The maximum uncertainties of non-dimensional parameters were ±5% for Reynolds number, ±7% for Nusselt number and ±9% for friction factor.

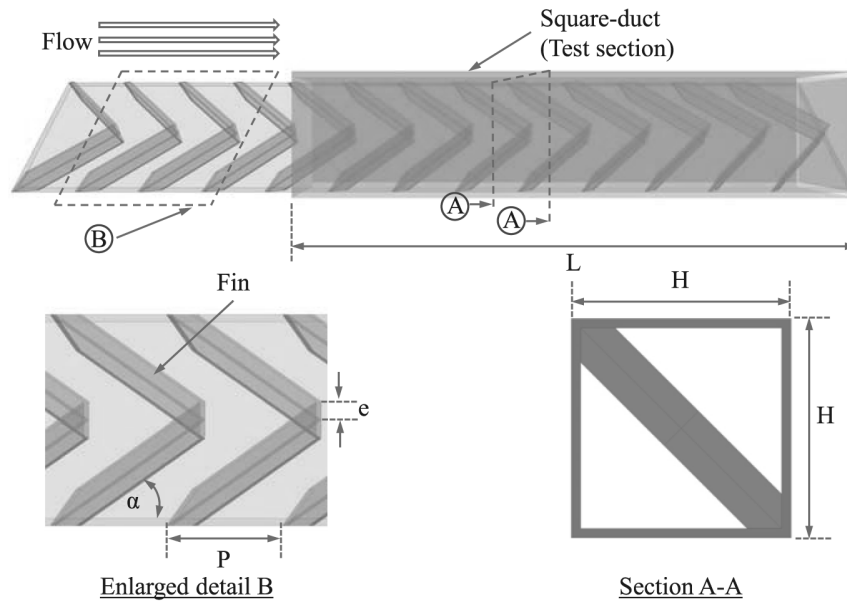


Figure 2 Test section with V-shaped fins

Data processing

The present experiment was conducted to investigate the heat transfer, pressure drop and thermal performance in a square-duct inserted with the V-shaped fins. The results obtained are displayed in dimensionless terms of Nusselt number and friction factor. The average heat transfer coefficients are calculated by using the experimental data via the following equations:

$$Q_{air} = Q_{conv} = \dot{m}C_p(T_o - T_i) \tag{1}$$

$$h = \frac{Q_{conv}}{A(\tilde{T}_s - T_b)} \tag{2}$$

in which,

$$T_b = (T_o + T_i)/2 \tag{3}$$

and

$$\tilde{T}_s = \sum T_s/28 \tag{4}$$

where A is the heat transfer surface area of duct, T_s is the local surface temperature along the duct length, and \tilde{T}_s is the average surface temperature. Thus, the average Nusselt number is written as

$$Nu = \frac{hD_h}{k} \tag{5}$$

The Reynolds number based on the duct hydraulic diameter (D_h) is given by

$$Re = UD_h/\nu \tag{6}$$

The duct hydraulic diameter is defined by

$$D_h = \frac{4A_c}{P_w} = H \tag{7}$$

in which A_c is the cross-sectional area and P_w is the wetted perimeter of the cross section.

The friction factor is evaluated by

$$f = \frac{2}{(L/D_h)} \frac{\Delta P}{\rho U^2} \tag{8}$$

where ΔP is the pressure drop across the test duct and U is the mean air velocity in the duct. All properties of air are evaluated at the overall bulk air temperature from Eq. (3).

The thermal enhancement factor (η) defined as the ratio of the heat transfer coefficient of an inserted duct, h to that of smooth duct, h_0 , at a constant blowing power¹⁰ is given by

$$\eta = \frac{h}{h_0} \Big|_{bp} = \frac{Nu}{Nu_0} \Big|_{bp} = \left(\frac{Nu}{Nu_0} \right) \left(\frac{f}{f_0} \right)^{-1/3} \tag{9}$$

Results and Discussions

1. Validation of smooth square-duct

The experimental results of Nusselt number and friction factor obtained from the present smooth duct are compared with those from correlations of Gnielinski and Petukhov found in Ref.¹¹ for turbulent flow in ducts.

Gnielinski's correlation

$$Nu = \frac{(f/8)(Re - 1000)Pr}{1 + 12.7(f/8)^{1/2}(Pr^{2/3} - 1)} \tag{10}$$

Petukhov's correlation

$$f = (0.79 \ln Re - 1.64)^{-2} \tag{11}$$

The comparison of Nu and f obtained from the present smooth duct with those from correlations of Eqs. (10, 11) is depicted in (Figure 3) It is seen in the figure that the present results are in good agreement within $\pm 5\%$ with the correlation data.

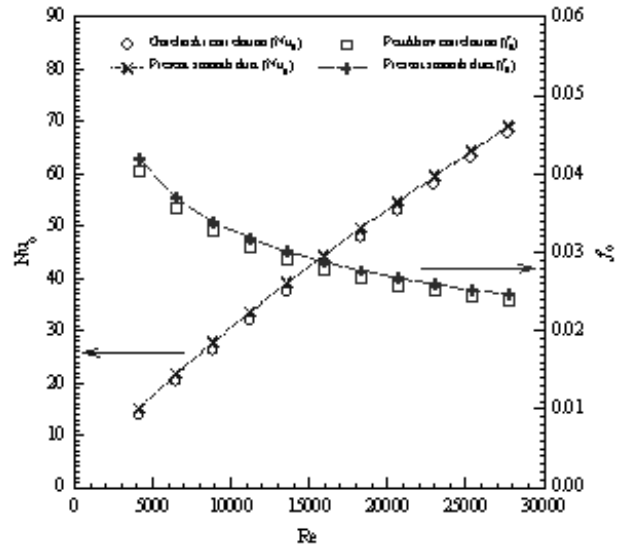


Figure 3 Validation of Nu_0 and f_0 for smooth duct.

2. Effect of PR on heat transfer

The Nu and Nu/Nu_0 plotted against Re values is displayed in (Figure 4a) and b, respectively. The Nusselt number ratio, Nu/Nu_0 , is defined as a ratio of the enhanced Nusselt number to Nusselt number of smooth duct. In (Figure 4a), the inserted duct yields the considerable heat transfer enhancement with similar trend pattern in comparison with the smooth duct and thus, the Nu increases with the rise of Re . It is seen in the (Figure 4b) that the decrement of PR results in the increase in Nu/Nu_0 . This is because the effect of the vortex flows from the V-shaped fins can help to increase the turbulence intensity and to transport the fluid from the central core to the near-wall regions. Also, the vortex flows can wash up the flow trapped in the duct corner regions normally act as ineffective heat transfer areas, leading to higher heat transfer rate in the duct. At a given BR, the V-shaped fins provides the Nu/Nu_0 in the range of 3.93-4.00, 3.82-3.89, 3.62-3.68, 3.43-3.50, 3.18-3.24 and 3.00-3.05 for PR=0.5, 1.0, 1.5, 2.0, 2.5 and 3.0 respectively. It can be observed that the duct with PR=0.5 provides heat transfer rate higher than others. This can be attributed to the use of V-shaped fins with the smallest pitch leading to stronger vortex strength of the flow and thus promoting high levels of mixing over the others.

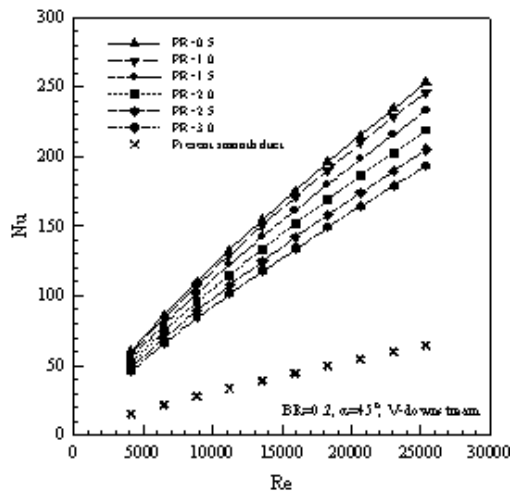
3. Effect of PR on friction loss

The plot of f and f/f_0 against Re is, respectively, exhibited in (Figure 5a) and b for various PR values. It is

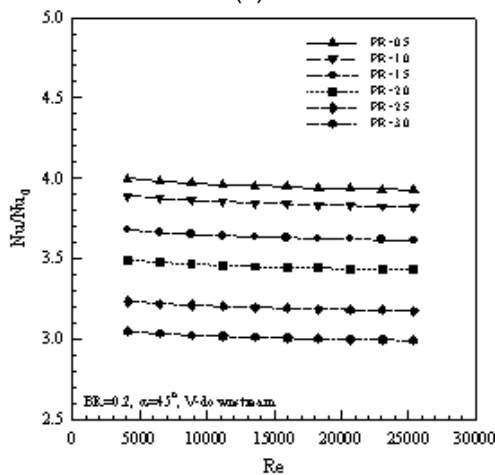
visible in (Figure 5a) that the use of the V-shaped fins vortex generators leads to substantial increase in f above the smooth duct and the f shows the decreasing tendency with the increment of Re . It can be observed in the (Figure 5b) that the ff_0 for the inserted duct tends to increase considerably with rising Re but with reducing PR. The inserted duct at PR=0.5 provides the highest ff_0 value. This is because the use of PR=0.5, caused higher flow resistance, larger surface area and the reverse flow, leading to the substantial increase in pressure drop. The ff_0 values for the V-shaped fins of the BR=0.2 is in the range of 28.04–33.62, 22.00–26.38, 16.30–19.54, 14.94–17.91, 13.10–15.70 and 11.82–14.17 for PR=0.5, 1.0, 1.5, 2.0, 2.5 and 3.0 respectively.

4. Thermal performance evaluation

(Figure 6) presents the influence of PR values on thermal enhancement factor (h) for using the V-shaped fins vortex generators. The h value was obtained from comparison of the Nu/Nu_0 and ff_0 ratios at similar blowing power as defined in Eq. (9). In the figure it is observed that the h shows the downtrend pattern with the increment in Re for all cases investigated. The use of the V-shaped fins leads to much higher h than that of the smooth duct for all cases. It is visible that the maximum h is achieved for using the V-shaped fins with PR=1.5 and this case of PR values is considered to be the best operating condition in this investigation. The highest h is about 1.45 at the lowest Re .

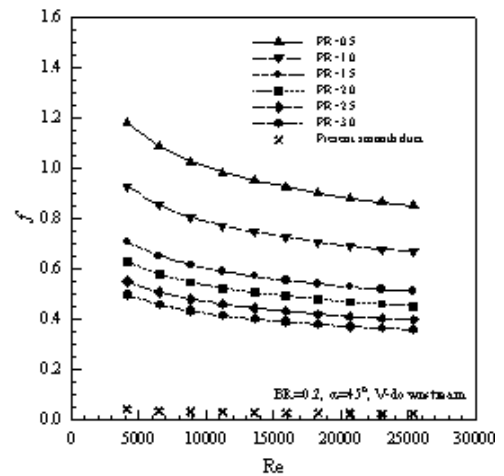


(a)

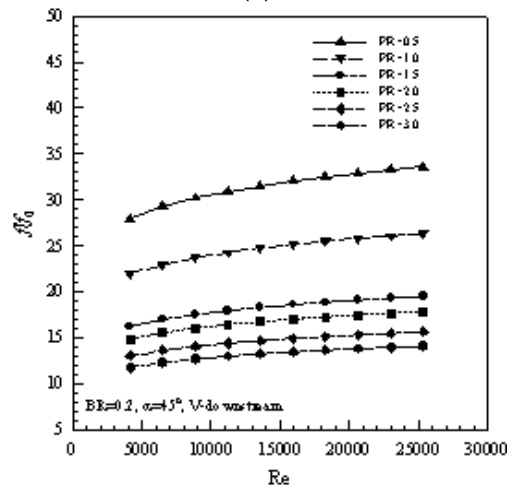


(b)

Figure 4 Variation of (a) Nu and (b) Nu/Nu₀ with Re.



(a)



(b)

Figure 5 Variation of (a) f and (b) ff_0 with Re.

Conclusion

An experimental investigation on heat transfer, flow friction and thermal enhancement factor characteristics in a uniform heat-fluxed square-duct with the V-shaped fins vortex generator inserts at different PR for turbulent air flow, Reynolds number from 4000 to 25,000 has been conducted. The V-shaped fins insert provides a significant effect on the change of flow direction in the duct leading to the considerable increase in both heat transfer and pressure drop. It is seen that the maximum heat transfer rate and pressure drop from the vortex generator devices is found at the smallest of PR. At the given BR, the V-shaped fins with PR=0.5 provides much higher Nusselt number and friction factor than the others while, the V-shaped fins with PR=1.5 yields the highest thermal enhancement factor around 1.45 at the lowest Re value.

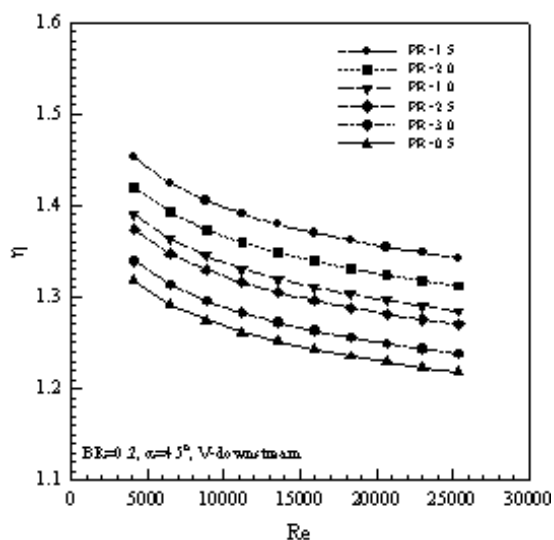


Figure 6 Variation of η with Re

References

- [1] Liu, J., Gao J., Gao T. and Shi X., Heat Transfer Characteristics in Steam-Cooled Rectangular Channels with Two Opposite Rib-Roughened Walls, *Appl. Therm. Eng.*, 2013; 50, 104-111.
- [2] Promvong, P., Skullong, S., Kwankaomeng, S. and Thianpong, C., Heat Transfer in Square Duct Fitted Diagonally with Angle-Finned Tape-Part 1: Experimental Study, *Int. Commun. Heat Mass Transfer*, 2012; 39: 617-624.
- [3] Promvong, P., Jedsadaratanachai, W., Kwankaomeng, S. and Thianpong, C., 3D Simulation of Laminar Flow and Heat Transfer in V-Baffled Square Channel, *Int. Commun. Heat Mass Transfer*, 2012; 39: 85-93.
- [4] Singh, S., Chander, S. and Saini, J.S., Heat Transfer and Friction Factor Correlations of Solar Air Heater Ducts Artificially Roughened with Discrete V-Down Ribs, *Energy*, 2011; 36: 5053-5064.
- [5] Tanda, G., Effect of Rib Spacing on Heat Transfer and Friction in a Rectangular Channel with 45° Angled Rib Turbulators on One/Two Walls, *Int. J. Heat Mass Transfer*, 2011; 54: 1081-1090.
- [6] Hans, V.S., Saini, R.P. and Saini, J.S. Heat Transfer and Friction Factor Correlations for a Solar Air Heater Duct Roughened Artificially with Multiple V-Ribs, *Solar Energy*, 2010; 84: 898-911.
- [7] Khan, R.K., Ali, M.A.T. and Akhanda, M.A.R., Heat Transfer Augmentation in Developing Flow Through a Ribbed Square Duct, *J. of Therm. Sci.*, 2006;15: 251-256.
- [8] Momin, A.M.E., Saini, J.S. and Solanki, S.C. Heat Transfer and Friction in Solar Air Heater Duct with V-Shaped Rib Roughness on Absorber Plate, *Int. J. Heat Mass Transfer*, 2002; 45: 3383-3396.
- [9] [ANSI/ASME, Measurement Uncertainty, PTC 19, 1-1985. Part I, 1986.
- [10] Webb, R. L., Principles of Enhanced Heat Transfer, New York: John-Wiley & Sons, 1994.
- [11] Incropera, F.P., Dewitt, D.P., Bergman, T.L. and Lavine, A.S., Introduction to Heat Transfer, 5th ED, John Wiley & Sons, 2006.

Texture of Cooked Selected KDML 105 Rice Mutants and Its Related Variables

Wiwat Wangcharoen^{1*}, Chaveewon Phanchaisri¹, Wichitra Daengprok¹, Rimruthai Phuttawong², Tawan Hang Soongnern³, Songchao Insomphun⁴ and Boonrak Phanchaisri⁵

Received: 29 May 2015; Accepted: 13 July 2015

Abstract

The relation of cooked rice texture, pasting properties, contents of amylose, protein, and fat of selected KDML 105 rice mutants, obtained from low energy ion beam bombardment including HyKOS3, HyKOS3-1, HyKOS7-1, HyKOS16, HyKOS21 and HyKOS22, together with KDML 105 and Hom Viengping was studied. The multiple regression analysis showed that hardness was related to amylose content, water addition when cooked, setback and peak time. Cohesiveness was related to amylose and protein content as well as setback. Adhesiveness was related to protein content and water addition when cooked. Springiness and chewiness were related to amylose and protein content, setback and peak time. For pasting properties, it was found that breakdown, setback and peak time was related to amylose and protein content. Pasting temperature was related to amylose, protein, and fat content, while final viscosity was related to amylose content only.

Keywords: KDML 105rice mutants, texture, pasting properties, amylose, protein

Introduction

Rice is a major food crop for the people of the world in general and Asians in particular: Nearly 90% of the world's rice is produced and consumed in this region¹. KDML 105, Thai Hom Mali rice, or Thai jasmine rice, is popular worldwide among rice consumers because of its distinctive properties. It is classified as non-glutinous rice with long grain and slender shape. Its grain is transparent or clear and contains very few chalky kernels. When cooked, it has a soft texture and presents a natural fragrant smell. Unfortunately, it is susceptible to all major diseases and insect pests². And it can be cultivated only once a year in the in-season period (July–December)³ and only in rainfed area, the North and Northeast of Thailand².

Many efforts have been used to increase the production of rice with desired properties of KDML 105. One of them is the application of low energy ion beam bombardment to produce new genetic modifications. Its

application in KDML 105 at Chiang Mai University has resulted in many new lines with characters that allow higher yields including semi-dwarfism and photoperiod insensitivity³, blast disease resistance⁴, and drought resistance⁵, and characters that provide potential health benefit including dark purple/black pericarp^{3,5-6} and more antioxidant enzyme activity⁷.

Since the soft texture of cooked KDML 105 is desirable, texture parameters, pasting properties and chemical contents of 6 KDML 105 rice mutants cultivated in the in-season and off-season periods, KDML 105 (control for the in-season period) and Hom Viengping (control for the off-season period) were studied to find out variables related to texture of cooked rice. Six KDML 105 rice mutants were selected in this work because they could yield as much as 910 – 1,725 kg/rai, when cultivated with good care⁸.

¹ Faculty of Engineering and Agro-Industry, Maejo University, Chiang Mai 50290, Thailand

² Institute of Product Quality and Standardization, Maejo University, Chiang Mai 50290, Thailand

³ Rainbow Farm, Chiang Mai 50330, Thailand

⁴ Faculty of Agriculture, Chiang Mai University, Chiang Mai 50200, Thailand

⁵ Science and Technology Research Institute, Chiang Mai University, Chiang Mai 50200, Thailand

* Corresponding Author: wiwat@mju.ac.th

Materials and Methods

1. Rice Sample

All rice samples including KDML105, Hom Viengping and two crops of 6 selected KDML 105 rice mutants (HyKOS3, HyKOS3-1, HyKOS7-1, HyKOS16, HyKOS21 and HyKOS22) were supplied by the Science and Technology Research Institute, Chiang Mai University.

2. Cooking Method

The 150 g of rice sample was washed, drained and weighted. Water was added to make a certain rice and water ratio at 1:1.50, 1:1.75 and 1:2.0 (w/w). Cooking was done by the electric rice cooker (SHARP Model KSH 206, Thai City Electric, Bangkok, Thailand) at 300 watts for 10 – 21 min depending on rice and water ratio and rice samples.

3. Texture Measurement

Cooked rice was kept in the inner pot of the electric rice cooker (3 hr) for cooling down to room temperature. Its texture parameters were measured by Lloyd Universal testing Machine (Model LR10K, Lloyd Instruments, Hampshire PO15 5TT, UK). Cooked rice was compressed by a 10-mm diameter steel cylinder probe with a flat end. Test speed was 100 mm/min and the sample was compressed to 75%, held for 3 sec., released and compressed again to complete the two-cycle compression test⁹. The measurement was repeated ten times per sample.

Texture parameters including hardness (maximum force, kgf), cohesiveness (ratio of positive force area of the second compression to that of the first compression) and adhesiveness (negative area between the first and second compressions, kgf.mm), springiness (height that sample springs back after the first compression, mm) and chewiness (energy required to chew a solid food to the point required for swallowing it = hardness x cohesiveness x springiness, kgf.mm) were derived from the instrument software.

4. Pasting Properties Measurement

Rice sample was ground to make rice flour. Its pasting properties were measured by Rapid Visco Analyzer (Model 3-D RVA, Newport Scientific, Sydney, Australia). Three gram of rice flour and 25 ml of distilled

water were mixed. The sample was held at 50 °C for 1 min, heated to 95 °C at a rate of 12 °C/min, held at 95 °C for 2.5 min, cooled to 50 °C at a rate of 12 °C/min and held at 50 °C for 2.5 min. The rotating speed of the paddle was kept at 160 rpm throughout the run except at the first 10 s the paddle speed was 960 rpm¹⁰. All measurements were triple replicated.

The pasting properties including peak viscosity (maximum viscosity when heated, cP), peak time (time at peak viscosity, min), trough viscosity (minimum viscosity when heated, cP), breakdown (heat resistance and stickiness = peak viscosity – trough viscosity, cP), final viscosity (final viscosity after cooling down, cP), setback (gel formation and hardness = final viscosity – peak viscosity, cP), and pasting temperature (°C)¹¹ were derived from the instrument software.

5. Chemical Analysis

Amylose content was analyzed by Spectrophotometer¹². Protein and fat contents were analyzed by AOAC official method¹³.

6. Statistical Analysis

Each data set was analyzed by analysis of variance (Completely Randomized Design, CRD) and their means were compared by Tukey (a)'s w test. Multiple regression analysis was applied between texture parameters and chemical contents together with rice and water ratio, between texture parameters and pasting properties, and between pasting properties and chemical contents. All analysis was done by SPSS 16.0 and all graphs were created by Gnuplot 4.6.

Results and Discussions

1. Texture and Pasting Properties Measurement and Chemical Analysis

Results of texture parameters are shown in (Table 1), They were average values using 3 rice and water ratios (1:1.5, 1:1.75 and 1:2.0) When cooked. It was found that HyKOS3-1 and HyKOS22 were the hardest varieties with more cohesive, more springy and more chewy texture. Hom Viengping was harder than KDML 105 but their other parameters were similar. Other rice varieties had similar texture to Hom Viengping or

KDML 105, but HyKOS3 and HyKOS7-1 were less springy.

Pasting properties of samples were different than their texture parameters as shown in (Table 2) because pasting properties were analyzed with a certain water quantity, while texture parameters were analyzed by varying water quantity because the increase of rice and water ratio when cooked could make HyKOS3-1 and HyKOS22 softer⁹.

Chemical analysis in (Table 3) showed that HyKOS3-1 and HyKOS22, the hardest varieties, contained

higher amylose content at 20.63 ± 1.32 and $23.45 \pm 1.08\%$, respectively, which could be classified into intermediate amylose type (containing 20 – 25% amylose), while other rice varieties were low amylose type (10 – 20%). The appropriate quantity of cooking water depends on the level of amylose. Rice with low amylose needs less water and too much water addition make rice soggy and pasty. Rice with high amylose will be hard if water addition is not enough. The recommended rice and water ratio for KDML 105 is 1:1.7 by weight, and it should be reduced when a large amount of rice is cooked².

Table 1 Texture parameters of cooked Hom Viengping, KDML105 and its 6 selected mutants.

Rice varieties	Hardness (kgf)	Cohesiveness	Adhesiveness (kgf.mm)	Springiness (mm)	Chewiness (kgf.mm)
Hom Viengping	$0.89^b \pm 0.21$	$0.18^b \pm 0.03$	$0.25^{bc} \pm 0.18$	$8.81^b \pm 1.76$	$1.43^b \pm 0.57$
KDML105	$0.57^c \pm 0.12$	$0.19^b \pm 0.05$	$0.17^c \pm 0.12$	$8.33^b \pm 3.15$	$0.95^b \pm 0.50$
HyKOS3	$0.74^{bc} \pm 0.22$	$0.17^b \pm 0.03$	$0.33^b \pm 0.03$	$6.59^c \pm 1.26$	$0.88^b \pm 0.43$
HyKOS3-1	$1.30^a \pm 0.39$	$0.23^a \pm 0.05$	$0.67^a \pm 0.27$	$13.05^a \pm 1.83$	$4.10^a \pm 2.14$
HyKOS7-1	$0.73^{bc} \pm 0.15$	$0.18^b \pm 0.04$	$0.40^b \pm 0.25$	$6.21^c \pm 1.38$	$0.90^b \pm 0.52$
HyKOS16	$0.72^{bc} \pm 0.19$	$0.18^b \pm 0.04$	$0.37^b \pm 0.33$	$6.95^{bc} \pm 2.17$	$0.98^b \pm 0.50$
HyKOS21	$0.60^{bc} \pm 0.13$	$0.17^b \pm 0.03$	$0.29^{bc} \pm 0.18$	$7.79^b \pm 1.65$	$0.81^b \pm 0.31$
HyKOS22	$1.77^a \pm 0.64$	$0.24^a \pm 0.05$	$0.32^b \pm 0.17$	$12.73^a \pm 2.13$	$5.58^a \pm 2.75$

a, b, ... Means with different letters in the same column were significantly different ($p \leq 0.05$).

Table 2 Pasting properties of Hom Viengping, KDML105 and its 6 selected mutants.

Rice varieties	Peak viscosity (cP)	Peak time (min)	Trough viscosity (cP)	Breakdown (cP)
Hom Viengping	$2245^b \pm 139$	$5.9^{ab} \pm 0.1$	$1310^b \pm 82$	$936^b \pm 62$
KDML105	$1459^d \pm 151$	$5.9^{ab} \pm 0.1$	$901^d \pm 89$	$558^d \pm 73$
HyKOS3	$770^e \pm 162$	$5.6^b \pm 0.2$	$430^e \pm 93$	$340^e \pm 70$
HyKOS3-1	$2552^a \pm 124$	$6.2^a \pm 0.3$	$2131^a \pm 87$	$421^e \pm 48$
HyKOS7-1	$2280^b \pm 128$	$5.8^{ab} \pm 0.4$	$1269^b \pm 75$	$1011^{ab} \pm 94$
HyKOS16	$2528^a \pm 117$	$5.7^b \pm 0.2$	$1329^b \pm 73$	$1199^a \pm 82$
HyKOS21	$1925^c \pm 114$	$5.9^{ab} \pm 0.3$	$1112^c \pm 90$	$813^c \pm 38$
HyKOS22	$1372^d \pm 294$	$5.3^b \pm 0.4$	$891^d \pm 211$	$481^{de} \pm 109$

a, b, ... Means with different letters in the same column were significantly different ($p \leq 0.05$).

Table 2 (continued) Pasting properties of Hom Viengping, KDML105 and its 6 selected mutants.

Rice varieties	Final viscosity (cP)	Setback (cP)	Pasting Temperature (°C)
Hom Viengping	2525 ^b ± 88	280 ^c ± 82	86.7 ^a ± 0.4
KDML105	1605 ^d ± 117	146 ^d ± 62	87.5 ^a ± 1.2
HyKOS3	956 ^e ± 161	187 ^d ± 40	87.8 ^a ± 2.2
HyKOS3-1	4070 ^a ± 113	1518 ^a ± 82	83.2 ^b ± 1.0
HyKOS7-1	2294 ^{bc} ± 165	14 ^e ± 197	76.8 ^c ± 1.7
HyKOS16	2190 ^c ± 24	-338 ^f ± 127	73.3 ^d ± 1.0
HyKOS21	1839 ^d ± 106	-86 ^e ± 32	83.7 ^b ± 2.3
HyKOS22	1876 ^d ± 366	504 ^b ± 127	78.3 ^c ± 0.9

^{a, b, ...} Means with different letters in the same column were significantly different ($p \leq 0.05$).

Table 3 Chemical analysis of Hom Viengping, KDML105 and its 6 selected mutants.

Rice varieties	Amylose (%)	Protein (%)	Fat (%)
Hom Viengping	15.99 ^c ± 0.61	8.87 ^a ± 0.19	0.79 ^a ± 0.04
KDML105	12.87 ^e ± 0.95	4.19 ^c ± 0.40	0.30 ^b ± 0.12
HyKOS3	13.93 ^{de} ± 1.27	9.17 ^a ± 0.16	0.58 ^{ab} ± 0.05
HyKOS3-1	20.63 ^b ± 1.32	8.08 ^b ± 0.33	0.51 ^{ab} ± 0.13
HyKOS7-1	13.63 ^{de} ± 0.88	8.32 ^{ab} ± 0.98	0.82 ^a ± 0.20
HyKOS16	14.46 ^d ± 0.57	8.37 ^{ab} ± 0.32	0.65 ^a ± 0.16
HyKOS21	13.58 ^{de} ± 0.84	9.45 ^a ± 0.76	0.57 ^{ab} ± 0.25
HyKOS22	23.45 ^a ± 1.08	8.30 ^{ab} ± 0.71	0.39 ^b ± 0.17

^{a, b, ...} Means with different letters in the same column were significantly different ($p \leq 0.05$).

Data were reported on the basis of 14% grain moisture content.

2. Multiple Regression Analysis

Multiple regression analysis between texture parameters and chemical contents or pasting properties showed that hardness was related to amylose content, water addition when cooked, setback and peak time. Cohesiveness was related to amylose and protein content as well as setback. Adhesiveness was related to protein content and water addition when cooked. Springiness and chewiness were related to amylose and protein content, set back and peak time (Figure 1-2). These results agreed with Rice Department² which mentioned that rice with high amylose will be harder and more water must be put to

make it soften and Supakitkanjana¹¹ who mentioned that setback is a parameter representing gel formation and hardness.

For pasting properties, it was found that breakdown, setback and peak time was related to amylose and protein content. Pasting temperature was related to amylose, protein, and fat content, while final viscosity was related to amylose content only (Figure 3). These results agreed to a work of Fitzgerald et al.¹⁴ who found that protein and fat also affect to pasting properties of rice flour.

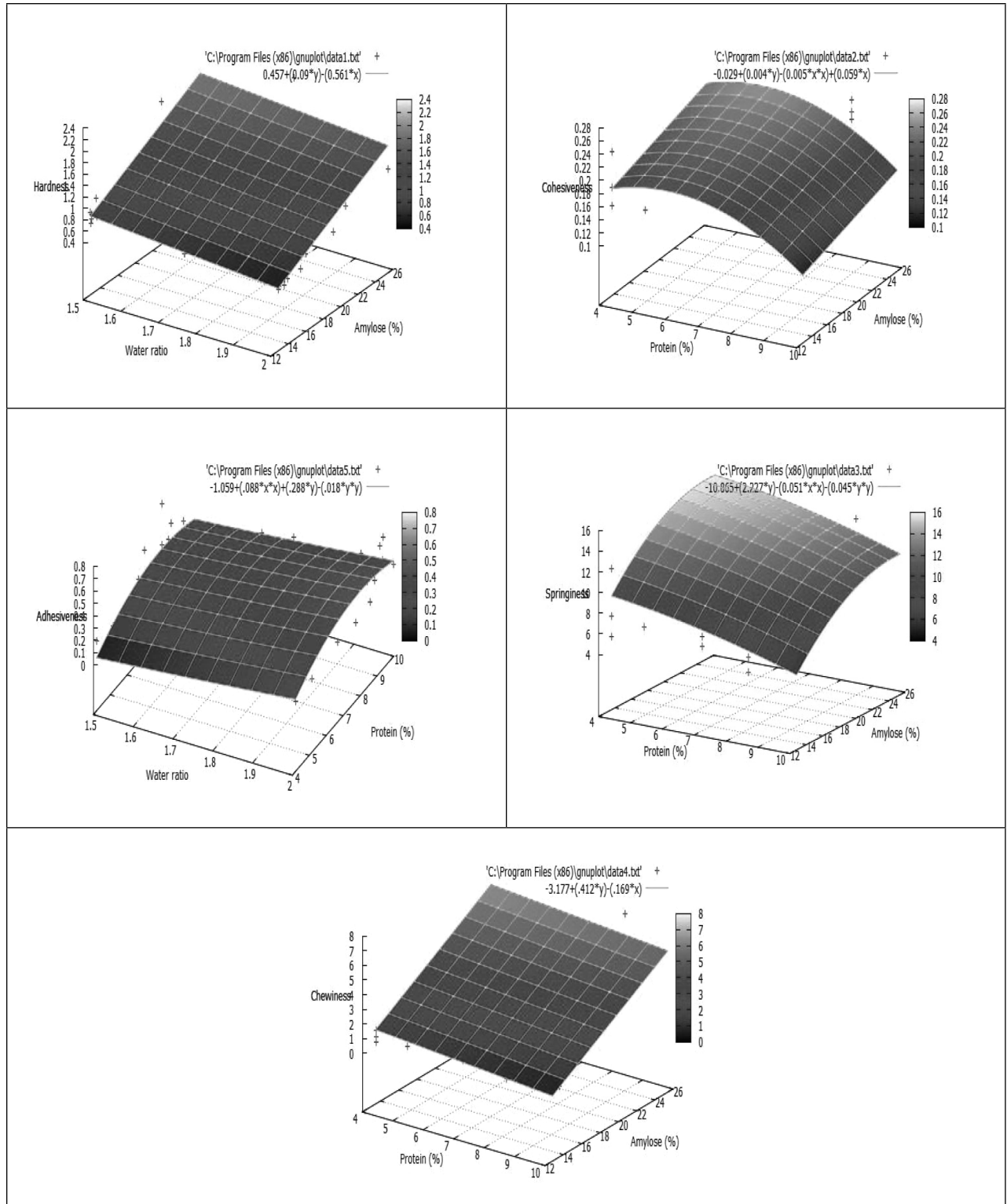


Figure 1 Multiple regression analysis between texture parameters and chemical contents, or rice and water ratio.

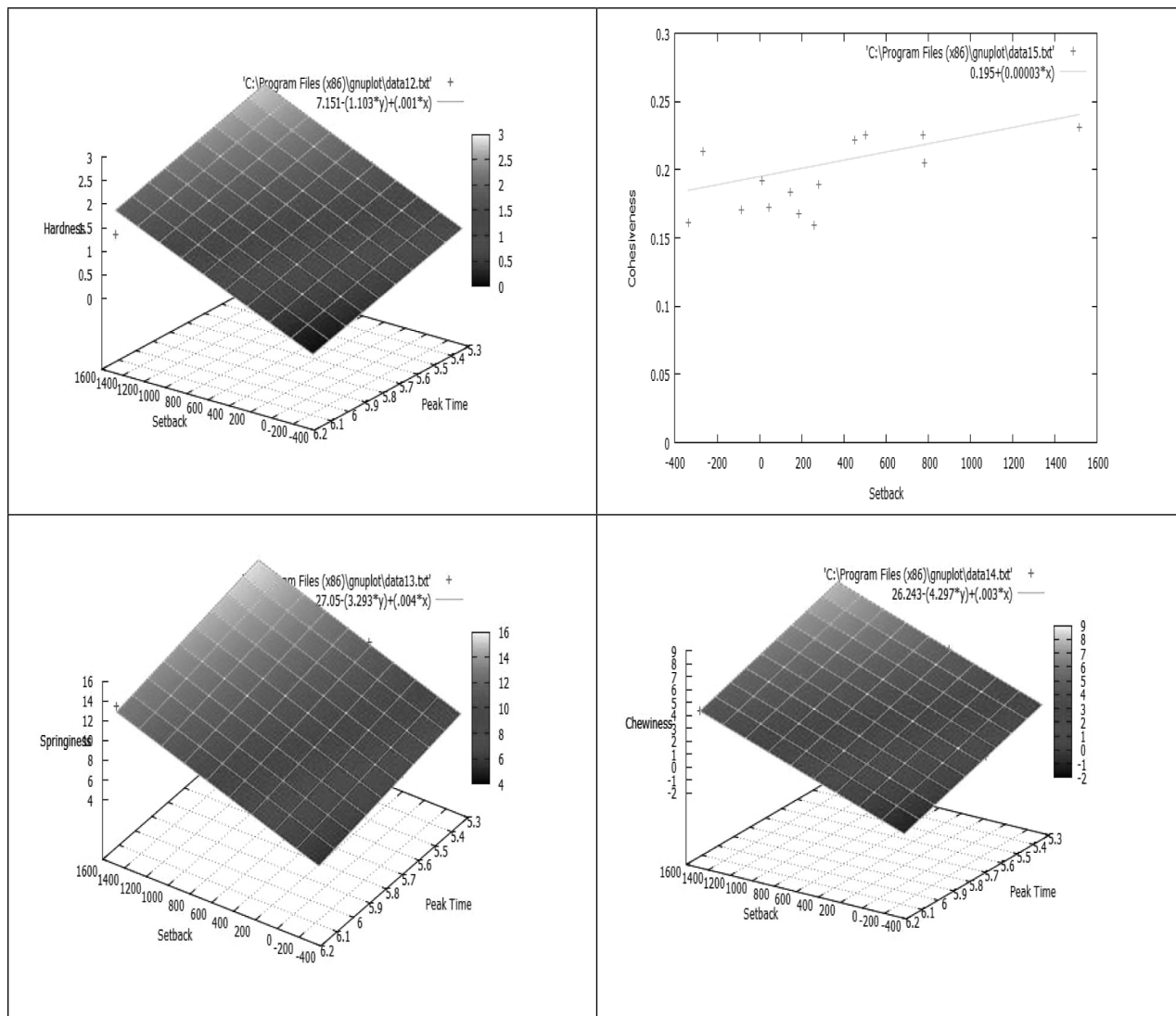


Figure 2 Multiple regression analysis between texture parameters and pasting properties.

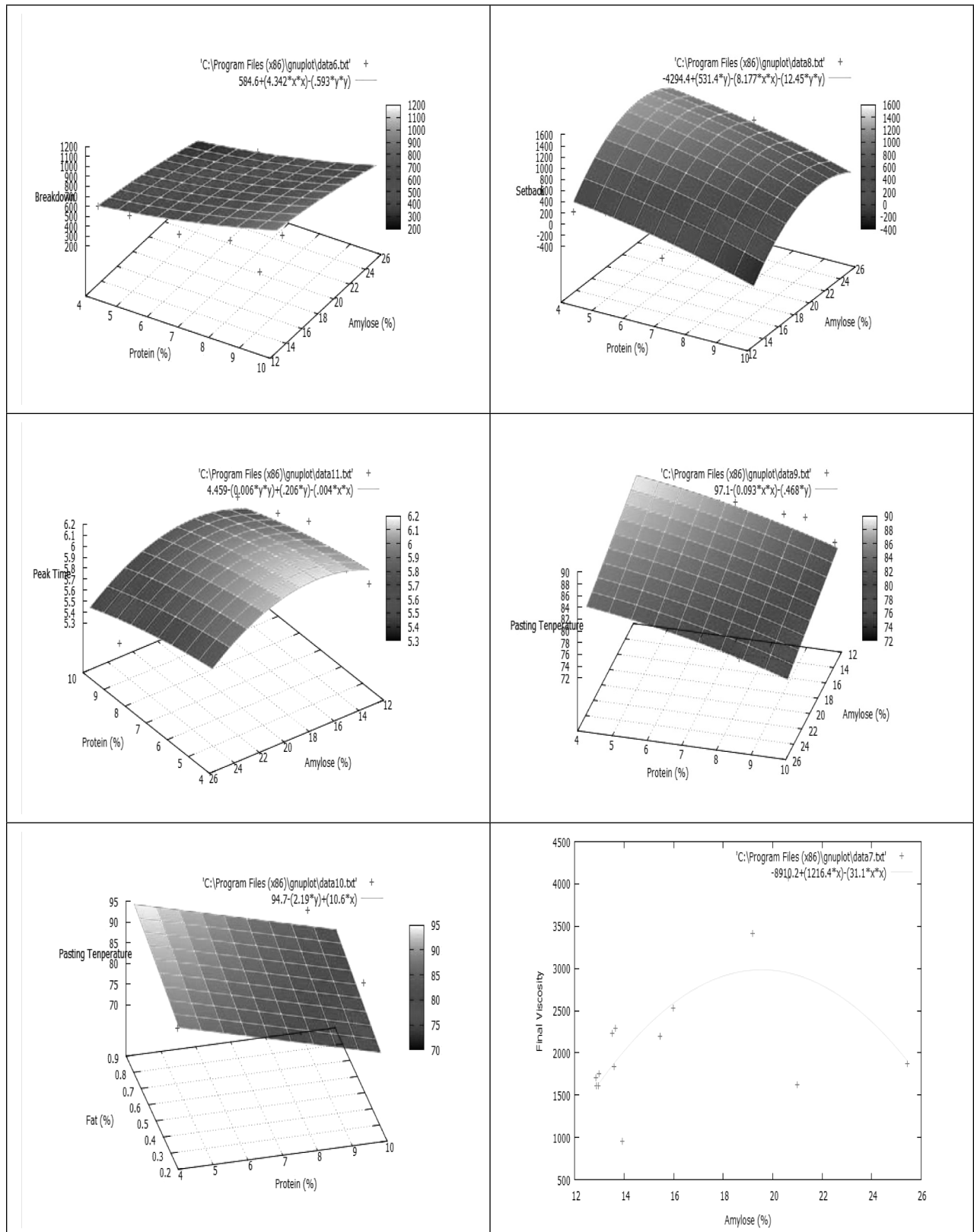


Figure 3 Multiple regression analysis between pasting properties and chemical contents.

Conclusion

Texture parameters of cooked selected KDML 105 rice mutants were related to amylose and protein contents, as well as rice and water ratio. Amylose, protein and fat contents were also related to pasting properties. Setback could be a pasting parameter representing hardness, cohesiveness, springiness and chewiness. This work also showed that peak time could be another variable reflecting texture parameters of cooked rice. Since both texture and pasting parameters have been used for identifying the properties of rice, the correlation between texture and pasting parameters in this work could be useful when the prediction of texture parameters from pasting parameters or vice versa is needed.

Acknowledgement

Authors would like to gratefully acknowledge the Agricultural Research Development Agency (ARDA) for the financial support of this research project.

References

- [1] Technical Advisory Committee and CGIAR Secretariat, Report of the Fifth External Programme and Management Review of International Rice Research Institute (IRRI), Food and Agriculture Organization of the United Nations, 1998. Available from: <http://www.fao.org/wairdocs/tac/x5801e/x5801e08.htmTopOfPage>.
- [2] Rice Department, Khao Dawk Mali 105, ISBN: 978-974-403-692-6, Bureau of Rice Research and Development, Bangkok, 2010.
- [3] Phanchaisri, B., Chandet, R., Yu, L.D., Vilaithong, T., Jamjod, S. and Anuntalabhochai S., Low-energy Ion Beam-induced Mutation in Thai Jasmine Rice (*Oryza sativa* L. cv. KDML 105), *Surface & Coatings Technology*, 2007; 201, 8024–8028.
- [4] Mahadatanapuk, S., Teraarusiri, W., Phanchaisri, B., Yu, L.D. and Anuntalabhochai, S., Breeding for Blast-disease-resistant and High-yield Thai Jasmine Rice (*Oryza sativa* L. cv. KDML 105) Mutants Using Low-energy Ion Beams, *Nuclear Instrument and Methods in Physic Research B*, 2013; 307, 229–234.
- [5] Boonrueng, N., Anuntalabhochai, S. and Jampeetong, A., Morphological and Anatomical Assessment of KDML 105 (*Oryza sativa* L. spp. *indica*) and Its Mutants Induced by Low Energy Ion Beam, *Rice Science*, 2013; 20(3), 213–219.
- [6] Semsang N., Chundet, R. and Phanchisri, B., Development of a SCAR Marker for Discrimination of a Thai Jasmine Rice (*Oryza sativa* L. cv. KDML105) Mutant, BKOS6, and Associated with Purple Color Trait in Thai Jasmine Rice-related Varieties, *American Journal of Plant Sciences*, 2013; 4, 1774-1783
- [7] Semsang, N. and Yu, L.D., Induction of Antioxidant Enzyme Activity and Lipid Peroxidation Level in Ion Beam Bombarded Rice Seeds, *Nuclear Instrument and Methods in Physic Research B*, 2013; 307, 603–609.
- [8] Agricultural Research Development Agency (ARDA), Selection of High Yielding KDML 105 Mutants Obtained From Using Low Energy Ion Beam Bombardment for Planting Areas in the North of Thailand, Final Report, ARDA, Bangkok, 2013.
- [9] Wangcharoen, W., Phanchaisri, C., Daengprok, W., Pocarat, R., Hangsoongnern, T., Insomphun, S. and Phanchaisri, B., Texture Profiles of Selected KDML 105 Rice Mutants Obtained from Using Low Energy Ion Beam Bombardment. *Rajamangala University of Technology Isan Journal, Special Issue 1*, 223-228, 2015.
- [10] Cheng, F.M., Zhong, L.J., Wang, F. and Zhang, G.P., Differences in Cooking and Eating Properties between Chalky and Translucent Parts in Rice Grains, *Food Chemistry*, 2005; 90, 39-46.
- [11] Supakitkanjana, W., RVA with Varieties and Storage Time of Thai Rice, *Chapa E-Magazine*, April 10, 2007. Available from: http://www.charpa.co.th/e_mag/rva_with_thai_rice_aging.htm.
- [12] National Bureau of Agricultural Commodity and Food standards, Thai Agricultural Commodity and Food Standard (TACFS) 4000-2003: Thai Hom Mali Rice, Ministry of Agriculture and Cooperatives, Bangkok, 2003.

- [13] AOAC., Official Methods of Analysis of AOAC International, 18th Edn., AOAC International, Gaithersburg, MD, 2005.
- [14] Fitzgerald, M.A; Martin, M., Ward, R.M, Park, W.D. and Shead, H.J., Viscosity of Rice Flour: a Rheological and Biological Study, Journal of Agricultural and Food Chemistry, 2003: 51, 2295-2299.

Heat Transfer Correlations for Small Closed End Heat Pipe with Special Vapor Chamber

Duangkamon Hemathurin¹, Narong Srihajong¹, Paisan Kumthong¹, Juthamat Silon¹

Received: 12 June 2015; Accepted: 13 July 2015

Abstract

In this paper, the empirical correlations for heat transfer characterizations of a small closed end heat pipe with special vapor chamber (SCEHP/SVC) are carried out. The heat transfer performance was introduced by a correlation function of dimensionless parameters namely Kutateladze number (Ku), Bond number (Bo), Weber number (We), Froude number (Fr), Prandtl number (Pr), Jacob number (Ja), Density ratio (DR) and Aspect ratio (AR). SCEHP/SVCs consists of two main parts such as a small closed end and special vapor chamber (where located at the bottom). Small closed end was made of small copper tubes with 2, 3 and 4.5 mm ID. Number of turns was 10. Special vapor chamber was an ID of 14.5, 17.5 and 20.5 mm. The evaporator, adiabatic and condenser sections were of equal length 50, 100 and 150 mm, with an inclination angle 60° and 90°. Water, ethanol and R-134a were selected as working fluids with filling ratios 30, 40 and 50% of the volume of a special vapor chamber. The operating temperatures were 60, 70 and 80°C that heated by hot water at the evaporator section, while the condenser section was cooled by cold water to 20°C. Experiments were recorded when the system reached a steady state, so as to calculate the heat flux. All experimental results of the heat flux of SCEHP/SVCs at inclined 90° orientation could be correlated in terms of modified Kutateladze number (Ku^*) as follows;

$$Ku_{90}^* = 2.25 \left[Bo^{-1.2} We^{-2.309} Fr^{1.249} Pr^{1.503} Ja^{-4.318} AR^{0.877} DR^{1.232} \right]$$

That correlation was used to predict the heat flux with standard deviations (STD) of $\pm 22.12\%$.

Keywords: Correlation, heat flux, Small closed end heat pipe with special vapor chamber

Introduction

Heat pipes (HP) are efficient heat transfer devices, which utilize working fluid to transfer heat from a heat source to a heat sink within a closed pipe¹. Nowadays, there are many types which depend on various mechanisms such as gravity assisted, capillary force, osmotic membrane or centrifugal force². As is widely know the advantages of a thermosyphon and oscillating heat pipe are high heat transfer performance and a simple structure.

Saehang and Srihajong³ invented a new type of heat pipe called a "Small closed end heat pipe with special vapor chamber" or SCEHP/SVC. Its design is based on an oscillating heat pipe mixed with thermosyphon in the hope to improve its performance. The Proposed SCEHP/SVCs structure is illustrated in (Figure 1)

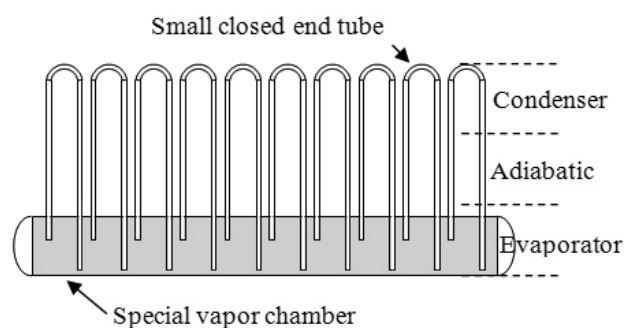


Figure 1 Small closed end heat pipe with special vapor chamber (SCEHP/SVC) using in experiments.

¹ Department of Mechanical Engineering, Faculty of Engineering, Rajamangala University of Technology Isan Khon Kaen Campus, Thailand, 40000
E-mail: dkmhmtr9@hotmail.com

The aim of this paper is to study the effects of dimensionless parameters (i.e. Kutateladze number (Ku), Bond number (Bo), Weber number (We), Froude number (Fr), Prandtl number (Pr), Jacob number (Ja), Density ratio (DR) and Aspect ratio (AR)) on the SCEHP/SVCs heat flux and establish an empirical correlation in order to predict the heat transfer performance in the vertical position (90°).

Materials and Methods

The experimental setup was divided into two parts; a small closed end tube (SCE) and special vapor chamber tube (SVC) (see Figure 1). The SCEs set of 10 copper tubes with 2, 3 and 4.5 mm ID were bent in a U-shape, whereas SVCs were also made of copper tube with 14.5, 17.5 and 20.5 mm ID. The SCEHP/SVCs were conducted with 50, 100 and 150 mm of section lengths (equal length in three sections). The experiments employed water, ethanol and R-134a as working fluid, 30%, 40% and 50% of filling ratio.

The schematic diagram of the experiment is shown in (Figure 2). The evaporator section was heated with hot water at 60°C , 70°C and 80°C but the condenser section was cooled by cold water 20°C . It was conducted at an inclination angle of 90° from horizontal plane.

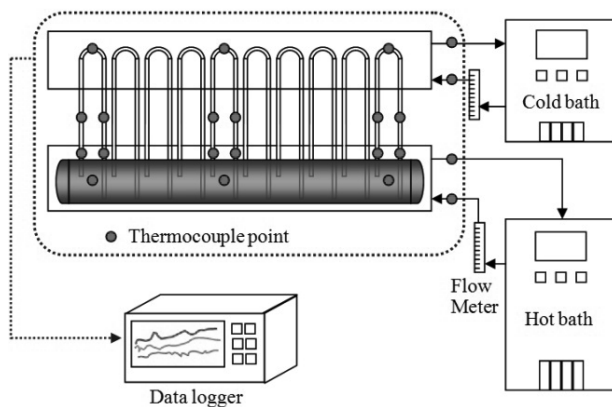


Figure 2 Schematic set up of experiments.

All components of test rig are shown in (Figure 2) They include a Yokogawa MV1000 data logger with $\pm 0.7^\circ\text{C}$ accuracy, Thermocouple type-K with accuracy $\pm 0.5^\circ\text{C}$, EYELA CA-112CE cold bath ($\pm 2^\circ\text{C}$ accuracy),

Thermo Fisher Scientific EX-35 hot bath ($\pm 0.01^\circ\text{C}$ accuracy) and two floating rotameters. the experiment procedure was conducted as follows, firstly, Set experiment on all parameters as shown in (Table 1). Then, set the desired temperature on the hot bath and cold bath. Next, supply the hot water and cold water to the water jacket of the evaporator and condenser respectively. When the system reaches a steady state, the temperature at thermocouple attach points are recording by the data logger in 10 minute interval. Then, loading the recorded data for calculating the heat flux and dimensionless parameters also. Finally, analyze the results.

Table 1 Tested parameters

Parameters	Value
SCEs ID	2, 3 and 4.5 mm
SVCs ID	14.5, 17.5 and 20 mm
Working fluid	Water, Ethanol, R-134a
Filling ratio	30%, 40% and 50%
Section length	50, 100 and 150 mm
Inclination angle	90 degree
Working temp.	60, 70 and 80°C

The heat flux was calculated by using calorific method is defined as;⁴

$$Q_c = \dot{m}_c C_{p_c} (T_{out} - T_{in})_c \quad (1)$$

$$\dot{q}_c = \frac{Q_c}{2\pi D_o L_c N} \quad (2)$$

Where, Q_c : heat transfer at condenser section (W), \dot{m}_c : coolant water mass flow rate (kg/s), C_{p_c} : specific heat of coolant water ($\text{J}/\text{kg}\cdot^\circ\text{C}$), $T_{in,out}$: inlet and outlet temperature ($^\circ\text{C}$), \dot{q}_c : the condenser heat flux (kW/m^2), D_o : the outer diameter of small closed end tube (mm), L_c : the condenser section length (mm) and N : number of turn.

Furthermore, in order to formulate an empirical correlation to predict the heat flux, which derived from dimensionless parameter group, It is necessary to consider all parameters (heat pipe geometric, heat input, volumetric filling ratio, tested orientation and working fluid etc.) that are associated with appropriate dimension-

less numbers. Thus, the dimensionless numbers involved are: Ku, Bo, We, Fr, Pr, Ja, DR and AR.⁵

$$q_c = f \{ Ku, Bo, We, Fr, Pr, Ja, DR, AR \} \quad (3)$$

The Kutateladze number (Ku) is introduced as an measure of the heat transfer performance⁶, so the other numbers could function in terms of Ku defined by;

$$Ku = f \{ Bo, We, Fr, Pr, Ja, DR, AR \} \quad (4)$$

Based on the analysis of the empirical correlation, multi linear regression was applied on Eq.(4) as power series.

$$Ku^* = c_0 \{ (Bo)^{c_1} (We)^{c_2} (Fr)^{c_3} (Pr)^{c_4} (Ja)^{c_5} (DR)^{c_6} (AR)^{c_7} \} \quad (5)$$

Where Ku^* : modified Ku, $c_0 \dots c_7$: regression constants that need to determined..

Then, taking the logarithm on both side of Eq.(5) and thus solved with least square method. Finally, correlation in modified Ku (Ku^*) form can be developed for the heat flux predicts (q_{pre}^*) become by Eq.(6).

$$q_{pre}^* = Ku^* \times \left(h_{fg} \rho_v \left[\frac{\sigma g (\rho_l - \rho_v)}{\rho_v^2} \right]^{0.25} \right) \quad (6)$$

Results and Discussions

Experimental results have been reported as follows;

1. Effect of Kutateladze number (Ku)

The Ku is the ratio of obtained heat flux to critical heat flux of the working fluid at the evaporator section. When Ku has a value of more than one it means the pool boiling phenomena has occurred. Thus, Ku can be expressed as;

$$Ku = \frac{q}{h_{fg} \rho_v \left[\frac{\sigma g (\rho_l - \rho_v)}{\rho_v^2} \right]^{0.25}} \quad (7)$$

Where, h_{fg} : latent heat of vaporization (J/kg), ρ_v : vapor density (kg/m³), ρ_l : liquid density (kg/m³), σ : surfacetension (N/m), g : gravitational acceleration (m/s²).

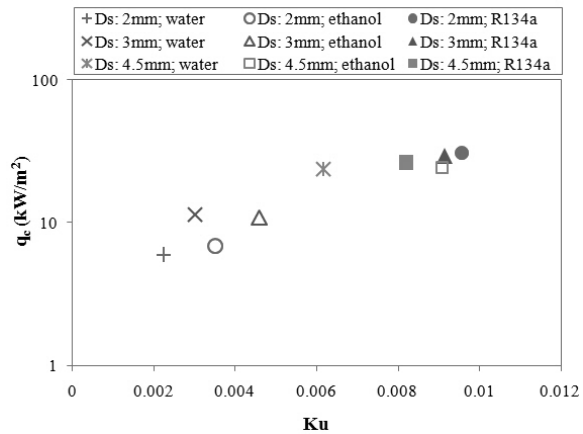


Figure 3 Relationship between heat flux and Kutateladze number. (Le: 50mm, De: 14.5 mm, Filling ratio: 40%, Working temp.: 80°C, Vertical position)

In (Figure 3), it can be seen that the Ku value increases following the working fluid type: R-134a, ethanol and water. The heat flux further increases with increasing Ku value.

2. Effect of Bond number (Bo)

The Bo is the ratio of buoyancy force to working fluid surface tension. It also represents the state of vapor bubbles that occur in nucleate boiling at the evaporator section. If Bo value is high, we can say that working fluid boils.

$$Bo = D_i \left[\frac{g (\rho_l - \rho_v)}{\sigma} \right]^{0.5} \quad (8)$$

Where, D_i : tube inner diameter (mm)

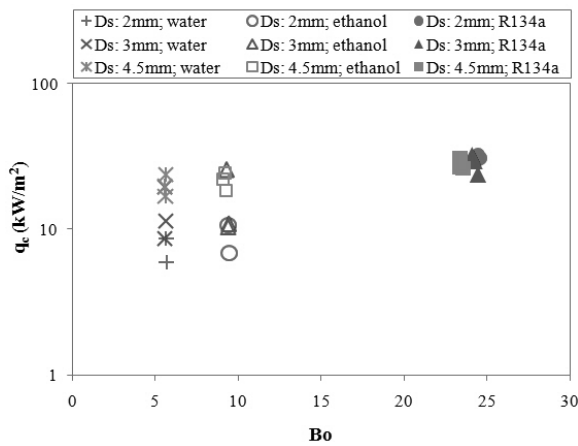


Figure 4 Relationship between heat flux and Bond number. (Le: 50mm, De: 14.5 mm, Filling ratio: 40%, Working temp.: 80°C, Vertical position)

The Ja value can be simply divided in three groups according to working as shown in (Figure 4). The result shows that maximum heat flux achieved when using R-134a.

3. Effect of Weber number (We)

The We is the ratio of dynamic force to surface tension force as expressed is Eq.(9). It represents the counter current interaction between the liquid film and vapor flow which occur inside evaporator and condenser section.

$$We = \frac{Q^2}{\rho_v D_i^3 h_{fg}^2 \sigma} \tag{9}$$

From experiments it was found that the We value increases with decreasing small closed end tube size. In the tested heat pipe, which is charged with water and ethanol, the obtained heat flux slightly decreases as the small closed end tube size decreases as shown in (Figure 5), This is the result of counter current phenomena inside the tube.

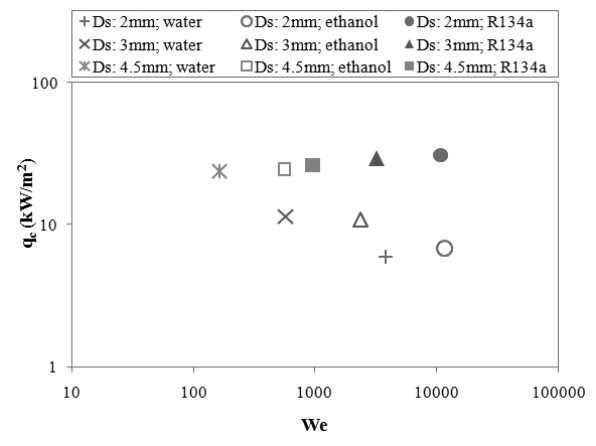


Figure 5 Relationship between heat flux and Weber number. (Le: 50mm, De: 14.5 mm, Filling ratio: 40%, Working temp.: 80°C, Vertical position)

4. Effect of Froude number (Fr)

The Fr is the ratio of the inertia force of vapor to the gravity force of the condensate liquid. It also represents the counter current be the same with We as earlier mentioned. and seen in (Figure 6)

$$Fr = \frac{Q^2}{\rho_v D_i^5 h_{fg}^2 g} \tag{10}$$

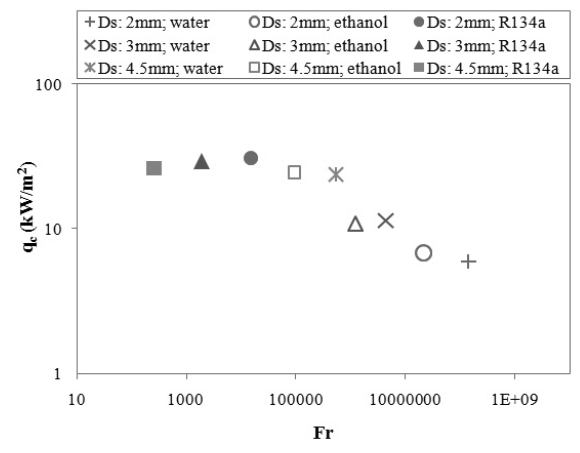


Figure 6 Relationship between heat flux and Froude number. (Le: 50mm, De: 14.5 mm, Filling ratio: 40%, Working temp.: 80°C, Vertical position)

5. Effect of Prandtl number (Pr)

The Pr is the ratio of the momentum diffusivity to thermal diffusivity of liquid as shown in Eq.(11). It

represents convection of heat transfer phenomenon inside the heat pipe.

$$Pr = \frac{\mu_l C_{p_l}}{k_l} \tag{11}$$

Where μ_l : liquid viscosity (Pa.s), C_{p_l} : specific heat capacity of liquid (J/Kg.°C), k_l : liquid thermal conductivity (W/m.K)

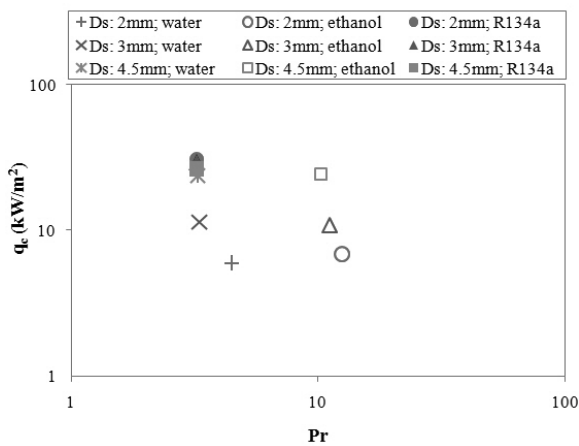


Figure 7 Relationship between heat flux and Prandtl number. (Le: 50mm, De: 14.5 mm, Filling ratio: 40%, Working temp.: 80°C, Vertical position)

In the results shown in (Figure 7), if the Pr value is low, it leads to high heat flux.

6. Effect of Jacob number (Ja)

The Ja is the ratio of latent heat to working fluid sensible heat. It represents the changing phase process of working fluid in the heat pipe.

$$Ja = \frac{h_{fg}}{C_{p_l} T_v} \tag{12}$$

Where T_v : vapor temperature (°C)

As we can see in (Figure 8), the Ja value is clearly classified by working fluid type. Moreover the heat flux gradually decreased when the small closed end tube size decreases.

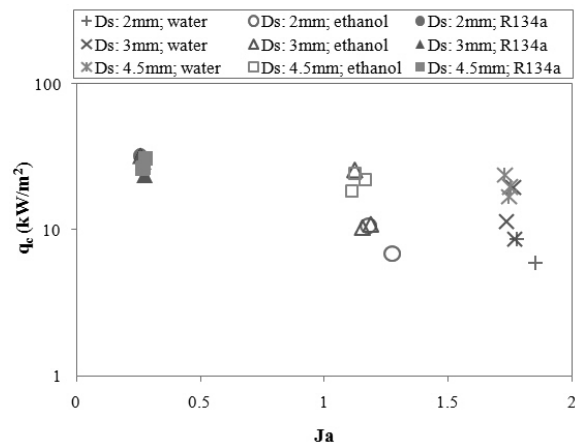


Figure 8 Relationship between heat flux and Jacob number. (Le: 50mm, De: 14.5 mm, Filling ratio: 40%, Working temp.: 80°C, Vertical position)

7. Effect of Density ratio (DR)

The DR is the ratio of vapor density to liquid density of the working fluid.

$$DR = \frac{\rho_v}{\rho_l} \tag{13}$$

Increased DR value is according to working fluid type, The tube size has a significant effect on the heat flux. (see Figure 9)

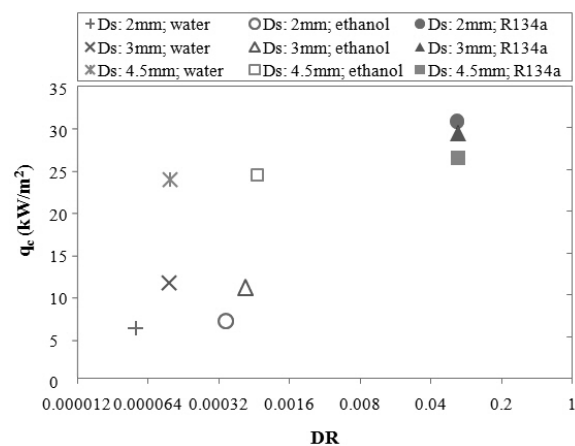


Figure 9 Relationship between heat flux and Density ratio. (Le: 50mm, De: 14.5 mm, Filling ratio: 40%, Working temp.: 80°C, Vertical position)

8. Effect of Aspect ratio (AR)

The AR is a dimensionless parameter which formulate based on the small closed end and special vapor chamber dimension as expressed in Eq.(13).

$$AR = \left(\frac{De}{Ds}\right) \left(\frac{Lv}{Le}\right) \tag{14}$$

Where De : diameter of the SVCs tube (mm), Ds : diameter of SCEs tube (mm), Lv : length of SVCs tube (mm) and Le : evaporator section length (mm). see in (Figure 10)

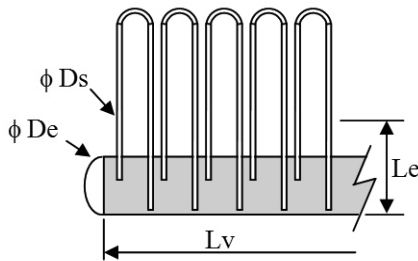


Figure 10 The dimension parameters of the tested heat pipe.

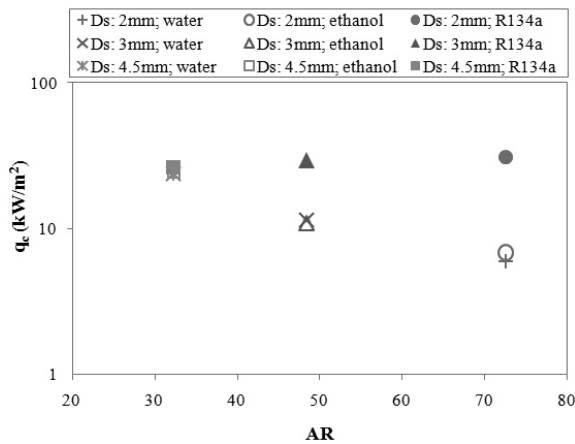


Figure 11: Relationship between heat flux and Aspect ratio. (Le : 50mm, De : 14.5 mm, Filling ratio: 40%, Working temp.: 80°C, Vertical position)

In (Figure 11) it shows that both water and ethanol have the same trend, AR increasing as a result of decreased heat flux but R-134a has no affect to heat flux at all.

9. Correlation equation

From the empirical correlation in terms of modified Ku form of Eq.(4) and Eq.(5) can be determined by the least squares technique as mentioned in section 2. Thus, the heat transfer correlation for SCEHP/SVCs in vertical position (90°) was;

$$Ku_{90}^* = 2.25 \left[\frac{Bo^{-1.2} We^{-2.309} Fr^{1.249}}{Pr^{1.503} Ja^{-4.318} AR^{0.877} DR^{1.232}} \right] \tag{15}$$

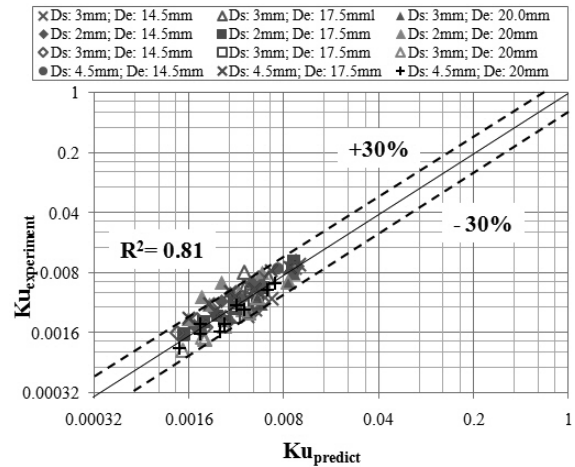


Figure 12 Comparison of experimental Ku vs. predicted Ku.

From (Figure 12), it shows the relationship between the Ku -experiment and Ku^* -predict which obtained from Eq.(15) with the coefficient of determination (R^2) was 0.81. It could be observed that the data were scatted; approximately 85% of deviations are falling within $\pm 30\%$ band.

Conclusion

This paper's study on the empirical correlation for predicts the heat flux of the SCEHP/SVCs in vertical position was investigated. It could be concluded that, the non-dimension parameters namely Ku , Bo , We , Fr , Pr , Ja , DR and AR . established correlation (expressed as Eq. (16)) and can predict the heat flux, has the standard deviation (STD) of $\pm 22.12\%$ as illustrated in (Figure 13).

$$q_{c_{pre}}^* = 2.25 \left[\frac{Bo^{-1.2} We^{-2.309} Fr^{1.249}}{Pr^{1.503} Ja^{-4.318} AR^{0.877} DR^{1.232}} \right] \times \left(h_{fg} \rho_v \left[\frac{\sigma g (\rho_l - \rho_v)}{\rho_v^2} \right]^{0.25} \right) \quad (16)$$

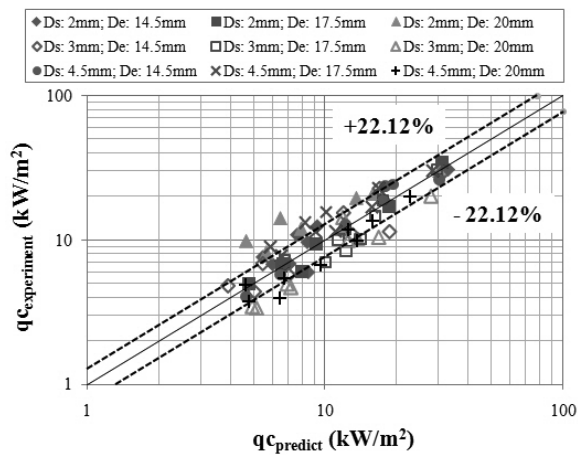


Figure 13 Comparison the heat flux experiment vs. prediction in vertical position.

Acknowledgement

The authors would like to express their appreciation to the Rajamangala University of Technology Isan and Research & Development Institute, Faculty of Engineering Rajamangala University of Technology Isan Khonkaen Campus for providing financial support to attend The 7th International Conference on Science, Technology and Innovation for Sustainable Well-Being 2015 (STISWB-VII).

References

- [1] Arab M. and Abbas A., A model-based approach for analysis of working fluids in heat pipes, *Applied Thermal Engineering*, 2014; 73(1): 751-763.
- [2] Waowaew N., Terdtoon P., Maezawa S., Kamonpet P., Klongpanich W., Correlation to predict heat transfer characteristics of a radially rotating heat pipe at vertical position, *Applied Thermal Engineering*, 2003; 23(8): 1019-1032.
- [3] Saehang K. and Srihajong N., Thermal performance for small closed end heat pipe with special vapor chamber, *Paper presented in The 6th International Conference on Science, Technology and Innovation for Sustainable Well-Being 2014*, Siem Reap, Cambodia.

- [4] Rittidech S., Terdtoon P., Murakami M., Kamonpet P., Jompakdee W., Correlation to predict heat transfer characteristics of a closed-end oscillating heat pipe at normal operating condition, *Applied Thermal Engineering*, 2003; 23(4): 497-510.
- [5] Parametthanuwat T., Rittidech S., Pattiya A., A correlation to predict heat-transfer rates of a two-phase closed thermosyphon (TPCT) using silver nanofluid at normal operating conditions, *Int. J. Heat and Mass Transfer*, 2010; 53(21-22): 4960-4965.
- [6] Qu J. and Wang Q., Experimental study on the thermal performance of vertical closed-loop oscillating heat pipes and correlation modeling, *Applied Energy*, 2013; 112: 1154-1160.

Experimental Investigations on Thermal Performance of Small Closed End Heat Pipes with Special Vapor Chamber

Kittipong Saehang¹, Narong Srihajong¹

Received: 12 June 2015; Accepted: 13 July 2015

Abstract

This article presents a thermal performance of a small closed end heat pipe with special vapor chamber (SCEHP/SVC). This study has carried out the effect of parameters (such as pipe size, filling ratio, working fluids and incline angle etc.) on thermal performance. The SCEHP/SVCs consists of 2, 3 and 4.5 mm ID small closed end pipe and special vapor chamber were 14.5, 17.5 and 20.0 mm ID (at evaporator section). The number of meandering turns was 10. The lengths of the evaporator were 50, 100 and 150 mm (The length of evaporator, adiabatic and condenser sections were equal). R-134a, ethanol and water were used as working fluids with filling ratios of 30, 40 and 50%. The evaporator was heated by hot water to 60, 70 and 80°C, whereas the condenser was cooled with water at 20°C. The inclination angles were 90, 60, 30, 0, -30, -60 and -90 degrees from horizontal plane. The temperatures at significant points (evaporator, adiabatic, condenser, inlet and outlet) were recorded every 10 minutes by data logger. As the result of the experiment, the boiling behaviors of SCEHP/SVCs, which has a small closed end of 2 mm acts like oscillating heat pipe, were like thermosyphon. As inclination angle increases, the heat flux increases. The best working fluid was R134a. The filling ratio, section length and small closed end size increased with decreasing heat flux. In addition, the heat transfer performances were excellent under the condition; the 2 mm of small closed end pipe, 17.5 mm vapor chamber pipe, R134a with filling ratio 30%, and also hot water at 80 °C with inclination angle of 90 degree.

Keywords: thermal performance, small closed end heat pipes, special vapor chamber

Introduction

In recent years, heat pipes have been widely employed as heat exchanger devices in many industries or other fields, owing to their excellent heat transfer performance, non complex structure and low heat input workability also¹. It utilizes the liquid → vapor phase change of working fluid inside the pipe. Nowadays the oscillating heat pipe (OHP) has become popular as has been reported in many literatures.

The oscillating heat pipe can be classified into three types such as, closed end oscillating heat pipe (CEOHP), closed loop oscillating heat pipe (CLOHP) and closed loop oscillating heat pipe with check valves (CLOHP/CV)².

The advantages of this heat pipe for instance; easy to build, fast thermal response and capable of conducting in many positions etc.³, but cannot operate at higher temperature differences. However, we have invented a new OHP in order to overcome its limitation. The new OHP was called “a Small Closed End Heat Pipe with Special Vapor Chamber” or “SCEHP/SVC”. Its structure seems to be the OHP combined with thermosyphon as shown in (Figure 1).

The aim of this study is to investigate the thermal performance of SCEHP/SVCs. The experiments conducted are based on the important thermo-mechanical parameters namely, internal diameter, section length, working fluid, volumetric filling ratio, heat input, and

¹ Department of Mechanical Engineering, Faculty of Engineering, Rajamangala University of Technology Isan Khon Kaen Campus, Thailand, 40000
E-mail: kit-ti-pong004@hotmail.com

tested orientation. The researcher hopes that the experimental results may bring about further information for design and develop the new heat pipe.

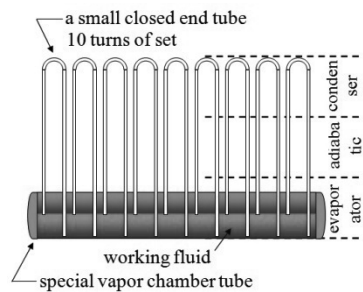


Figure 1 Shows the SCEHP/SVCs structure.

Materials and Methods

In order to built the tested SCEHP/SVCs (see in Figure 1), the upper part is called a small closed end (SCE) tube made of copper capillary tube of 2mm, 3mm and 4.5mm ID. It is bent into 10 meandering turns. At the lower part is a special vapor chamber (SVC) tube also made of copper tube in 14.5mm, 17.5mm and 20.0mm ID with 500mm of length. SCEHP/SVCs are fabricated by weld soldering. The evaporator, adiabatic and condenser sections were 50mm, 100mm and 150mm in equal length. The end of the capillary tube was inserted into the SVCs which can be seen in (Figure 1). Inclination angles were at -90, 60, 30, 0, 30, 60, 90 degree. The working fluids used were R134a, ethanol and water with filling ratios of 30%, 40% and 50% of the SVCs total volume. The working temperature were 60 °C, 70 °C and 80°C the condenser section was cooled by a cold bath at 20°C. The heating, cooling water jacket as well as adiabatic section were well wrapped with insulating sheet.

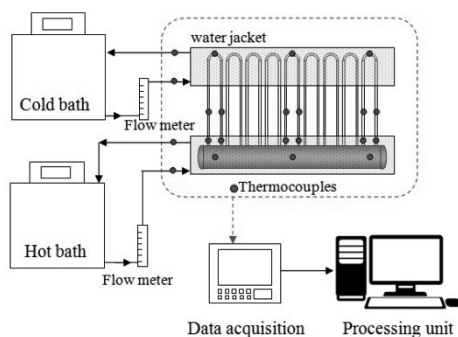


Figure 2 Schematic of experiment

(Figure 2) shows the experimental set up, the tested heat pipe was monitored and recorded by a Yokogawa MV1000 data acquisition with ±0.7°C accuracy, it was used with type-K thermocouple ±0.5°C accuracy (22 points attached). Thermo Fisher Scientific EX-35 hot bath (±0.01°C) was used to supply hot water to the evaporator section with controlled 0.014705 kg/s of flow rate. Moreover, the EYELA CA-112CE cold bath (±2°C) used to pump cool water to condenser section with 0.004643 kg/s of flow rate. All tested parameters are shown in (Table 1)

Table 1 Specifications and experimental conditions

Controlled parameter	Value
Turns	10 turns
Cold bath	20°C
Evaporator flow rate	0.014705 kg/s
Condenser flow rate	0.004643 kg/s
Variable parameters	Values
Small closed end tube	2, 3 and 4.5 mm ID
Vapor chamber tube	14.5, 17.5 and 20mm ID
Section length	50, 100 and 150mm
Working fluid	R134a, ethanol, water
Filling ratio	30%, 40% and 50%
Tested orientation	-90, 60, 30, 0, 30, 60, 90
Working temperature	60, 70 and 80°C

For the experiment procedure, The hot bath and cold bath were maintained at operating temperature steadily. When steady state was reached, the temperatures were recorded in 10 minute intervals by data acquisition. Those recorded values are used to calculate the thermal performance, is obtained by;⁴

$$Q_c = \dot{m}_c C_{p_c} \Delta T_c \tag{1}$$

$$\dot{q}_c = \frac{Q_c}{2\pi D_o L_c N} \tag{2}$$

Where Q_c is heat flux of condenser (W), \dot{m}_c is cooling water mass flow rate (kg/s), C_{p_c} is specific heat of cooling water (J/kg.°C), ΔT_c is difference temperature of cooling water between inlet and outlet (°C), \dot{q}_c is the condenser heat flux (kW/m²), D_o is the outer diameter of small copper tube (mm), L_c is the condenser length (mm) and N is number of turn.

$$Q_e = \dot{m}_e C_{p_e} \Delta T_e \tag{3}$$

$$\dot{q}_e = \frac{Q_e}{\pi D_{ve} L_e + N \left[2\pi D_o (L_e - D_{ve}) - 2\pi \left(\frac{D_o}{2} \right)^2 \right]} \tag{4}$$

In where Q_e is heat flux of evaporator (W), \dot{m}_e is hot water mass flow rate (kg/s), C_{p_e} is specific heat of hot water (J/kg. °C), ΔT_e is difference temperature of cooling water between inlet and outlet at evaporator (°C), D_{ve} is an outer diameter of SVC (mm), L_e is an evaporator length (mm) and \dot{q}_e is the evaporator heat flux (kW/m²).

Results and Discussion

The results of the experiment presented the effects of thermo-mechanical parameters, i.e. geometric dimensions, working fluid, volumetric filling ratio, heat input, and tested orientation.

1. Effect of inner diameter of the SCE

(Figure 3), shows the SCEs tube size affected at variations of inclination angle. The heat flux of SCEHP/SVCs which used SCEs tube of 2 mm ID reached the maximum value at 39.68 kW/m² in 90° orientation.

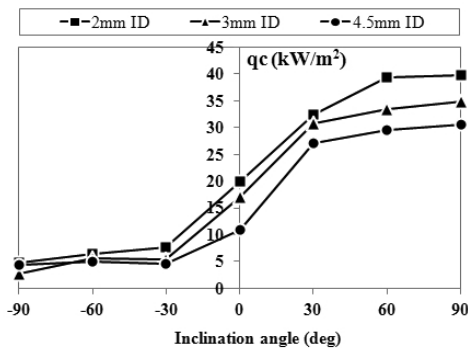


Figure 3 Heat flux with variations of inclination angle for various SCEs sizes. (SVC: 17.5mm ID, R-134a, 30% Fill ratio, section length: 50mm, working temp.: 80°C)

Furthermore, the effect of SCEs size on boiling behavior could be observed in (Figure 4). The thermal oscillations on the outer tube wall relate to the vapor

plug and liquid the slug periodically flushing inside heat pipe⁵. The SCEs size of 2mm ID had short amplitude of temperature fluctuations than others, also acts like an oscillating heat pipe.

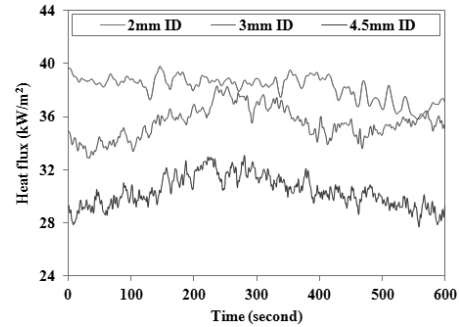


Figure 4 Heat flux fluctuation with time series for various SCEs sizes. (SVC: 17.5mm ID, R-134a, 30% Fill ratio, section length: 50mm, working temp.: 80°C)

2. Effect of inner diameter of the SVC

The SVCs diameters used were 14.5, 17.5 and 20.0mm ID. The effect of SVCs size on the heat flux at varying inclined angle, it found that the heat flux of 17.5 mm of SVCs ID was higher than 14.5 and 20.0 mm. The low heat flux achieved on 20.0mm ID is caused by a few spaces for supplied hot water, while on a 14.5 mm ID is due to smallest heat transfer area.

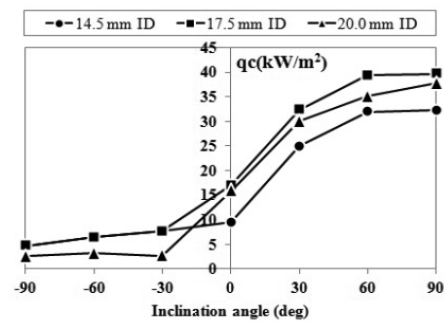


Figure 5 Heat flux with variations of inclination angle for various SVCs sizes. (SCE: 2mm ID, R-134a, 30% Fill ratio, section length: 50mm, working temp.: 80°C)

3. Effect of section length

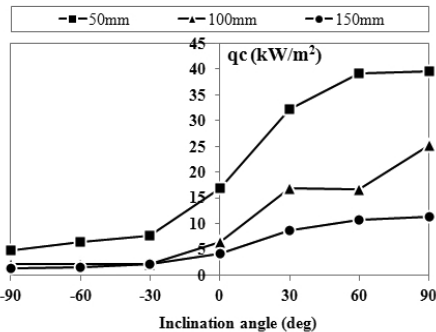


Figure 6 Heat flux with variations of inclination angle for various section lengths. (SCE: 2mm ID, SVC: 17.5mm ID, R-134a, 30% Fill ratio, working temp.: 80°C)

It is clear that the heat flux of the tested heat pipe with 50 mm section length was higher than the other length on every inclination angle. (Figure 6)

4. Effect of working fluid

(Figure 7) presents the relationship between heat flux and inclination angle at different working fluids. The result indicated that the R-134a was an excellent medium when compared with ethanol and water at every oriented angle, owing to R-134a having good properties, namely, low boiling point and a low melting point.

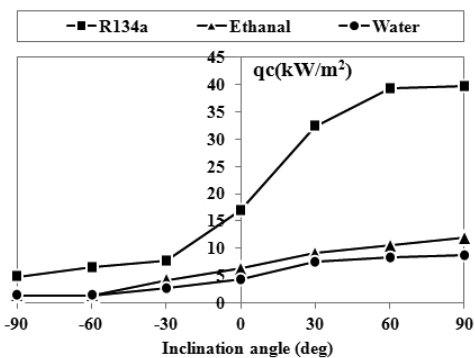


Figure 7 Heat flux with variations of inclination angle for various working fluid types. (SCE: 2mm ID, SVC: 17.5mm ID, section length: 50mm, 30% Fill ratio, working temp.: 80°C)

5. Effect of filled ratio

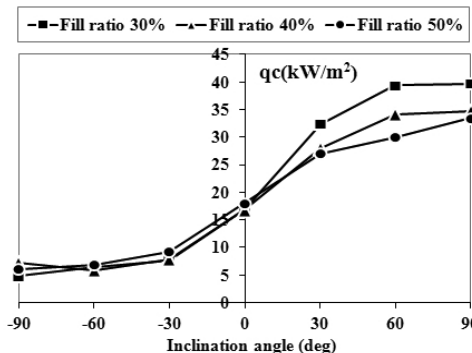


Figure 8 Heat flux with variations of inclination angle for various filling ratio. (SCE: 2mm ID, SVC: 17.5mm ID, section length: 50mm, R-134a, working temp.: 80°C)

As shown in (Figure 8), the 30% of filling ratio by SVCs volume obtained a heat flux more than 40% and 50%. Because, at the 50% filling ratio, the short leg of the capillary tube was touched with working fluid. It might cause a dynamic viscosity of bubble. In case of 40% have found same problem but less.

6. Effect of inclination angle

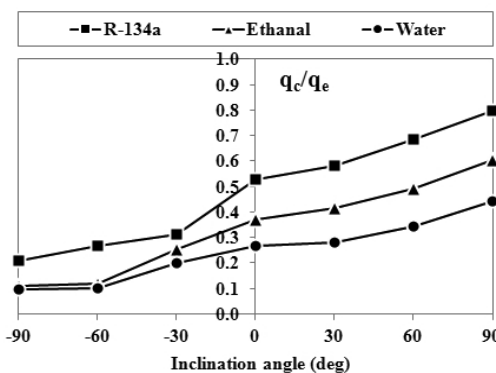


Figure 9 Heat transfer efficiency with variations of inclination angle for various working ratio. (SCE: 2mm ID, SVC: 17.5mm ID, section length: 50mm, filling ratio: 30%, working temp.: 80°C)

According to previous results, the tested heat pipe inclined 90 degree as it obtained maximum heat flux, because of the assisted gravity force and minimum friction

to counter the bubble movement. By increasing inclination angle transfer efficiency increased. The highest its efficiency is about 0.80 in the vertical position shown in (Figure 9).

7. Effect of working temperature

In (Figure 10) illustrated the effect of the operating temperature which circulates hot water by hot bath at various temperatures i.e. 60, 70 and 80 °C. It can be concluded that the heat flux is dependant on the heat input. The heat flux increased as increasing of heat input at inclined orientation range 0-90 degree.

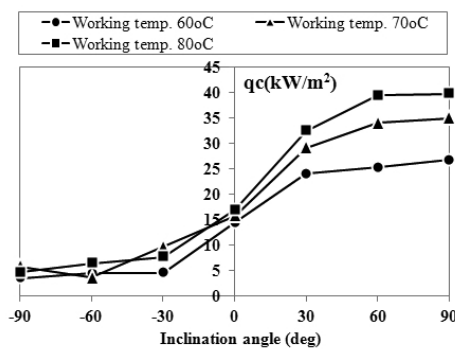


Figure 10 Heat flux with variations of inclination angle for various working temperature. (SCE: 2mm ID, SVC: 17.5mm ID, section length: 50mm, R-134a, filling ratio: 30%)

Conclusions

The conclusions for thermal performance of SCEHP/SVC which affects from parameters (e.g. pipe size, filling ratio, working fluid and inclination angle etc.) can be summarized as;

1. The increasing of the SCEs tube ID goes to remarkably decreasing heat flux. Because of the 2mm ID, the boiling behavior observed as heat flux fluctuations, act like a pulsating heat pipe while 3mm and 4.5 look like thermosyphon.
2. The 17.5 mm of SVCs tube was suited for this experiment.
3. Decreased heat flux when increasing section length, 50 mm is better.
4. The heat flux increases according to working fluid as R-134a, ethanol and water respectively.

5. Filling ratio of 30% by SVCs volume is appropriate in this experiment.

6. Inclination angle and working temperature increasing leads to heat performance increased.

7. The maximum heat flux of this heat pipe was achieved at 39.69 kW/m² on condition as; SCE: 2 mm ID, SVC: 17.5 mm ID, R-134a with filling ratio 30%, working temperature: 80 °C and tested in vertical position.

Acknowledgement

The authors would like to express their appreciation to the Rajamangala University of Technology Isan and Research & Development Institute, Faculty of Engineering Rajamangala University of Technology Isan Khon Kaen Campus for providing financial support for attending The 7th International Conference on Science, Technology and Innovation for Sustainable Well-Being 2015 (STISWB-VII).

References

- [1] Long, Z.Q. and Zhang, P., Heat transfer characteristics of thermosyphon with N₂-Ar binary mixture working fluid, *Int. J. Heat and Mass Transfer*, 2013; 63, 204-215.
- [2] Miyazaki, Y., Polasek, F., and Akachi, H., Oscillating heat pipe with check valves, *Paper presented in The 6th International Heat Pipe Symposium 2000*, Chiang Mai, Thailand.
- [3] Anuchitchanchai, P., Wongratanaphisan, T., Kamonpet, P., Terdtoon, P., Effect of aspect ratios and internal diameter on performance limit of a closed end oscillating heat pipe using refrigerant blend as working fluid, *Paper presented in The 7th International Heat Pipe Symposium 2003*, Jeju, Korea.
- [4] Wannapakhe, S., Rittidech, S., Bubphachot, B., Watanabe, O., Heat flux of a closed-loop oscillating heat pipe with check valves using silver nanofluid as working fluid, *Mechanical Science and Technology*, 2009; 23(6): 1576-1582.
- [5] Xu, J.L., Li, Y.X., Wong, T.N., High speed flow visualization of a closed loop pulsating heat pipe, *Int. J. Heat and Mass Transfer*, 2005; 48(16):3338-3351.

Study of Heat Transfer Characteristics of Bent Heat Pipe with Multiple Heat Sources by Using Finite Element Method

Nampon Sangpab¹, Phrut Sakulchangsattajai¹, Niti Kammuang-lue¹, Pradit Terdtoon¹

Received: 15 June 2015; Accepted: 13 July 2015

Abstract

Incompressible flow simulation of bent heat pipes with multiple heat sources at steady state is presented in this paper. The thermal performance was simulated in two dimension to predict the distribution of temperature, velocity and pressure in heat pipes. The fluid flow and heat transfer are determined from continuity, Navier-Stokes, and energy equations and they were analyzed by using Finite Element Method (FEM). The results from simulation of heat pipes have been compared to the experiments data from other researchers.

Keywords: finite element method, heat pipe, simulation

Introduction

Heat pipe is a heat transfer device that combines the principles of both thermal conductivity and phase transition to efficiently manage the transfer of heat between two solid interfaces. Heat pipes are widely used for thermal management in laptop and other applications. Heat sources from a CPU chip and VGA card is rapidly transferred to a heat sink via heat pipe. To decrease weight and size of laptop. Heat pipe must occupy less space in laptop. Tube bending is an unavoidable process and a heat pipe must uses with multiple heat sources to reduce the space in laptop. As in other applications, shape of heat pipe must be varied. Many researchers have developed similar heat pipes²⁻⁴. Most of them studied straight shape of heat pipe with one heat source and having a few simulations that use finite element method. Finite element method can be used in any shape so this

work will study bent heat pipes with multiple heat sources. In this study, simulation of heat pipe operation will simulate fluid flow and heat transfer of a bent heat pipe with multiple heat sources. The governing equations and boundary conditions were solved by using finite element method.

Governing Equations

The heat pipe domains consist of 3 parts: First is the vapor of working fluid in the vapor core. Second is the liquid of the working fluid in the wick. Last is the wall of the container. Under normal operation, the working fluid in the evaporator section transformed into a vapor, which flows to the condenser section. Working fluid in vapor phase subsequently condensed to a liquid, and returned back to the evaporator section through capillary forces in the wick.

¹ Department of Mechanical Engineering, Faculty of Engineering Chiang Mai University, Chiang Mai, Thailand 50200.
Email: nampon.s@hotmail.com

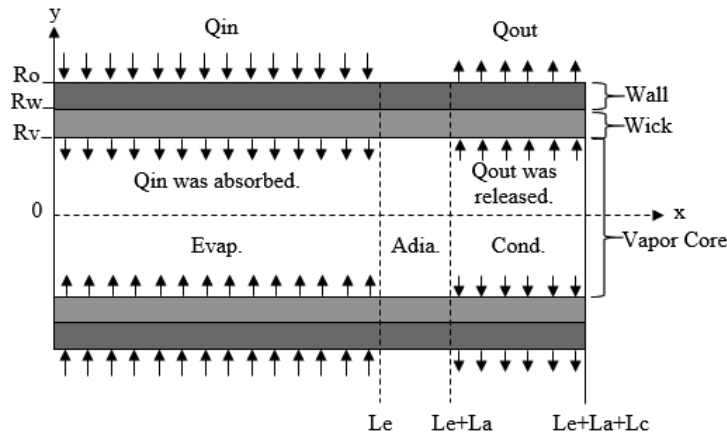


Figure 1 The schematic diagram of the heat pipe and the coordinate system.

In this simulation, Heat transfer and fluid flow were assumed to be incompressible flow, laminar flow and steady state.

1. Governing equations in vapor core

Continuity equation

$$\frac{\partial u_v}{\partial x} + \frac{\partial v_v}{\partial y} = 0 \tag{1}$$

Navier-Stokes equation

$$\rho_v \left(u_v \frac{\partial u_v}{\partial x} + v_v \frac{\partial u_v}{\partial y} \right) = -\frac{\partial p_v}{\partial x} + 2\mu_v \frac{\partial^2 u_v}{\partial y^2} + \mu_v \left(\frac{\partial^2 u_v}{\partial y^2} + \frac{\partial^2 v_v}{\partial x \partial y} \right) \tag{2}$$

$$\rho_v \left(u_v \frac{\partial v_v}{\partial x} + v_v \frac{\partial v_v}{\partial y} \right) = -\frac{\partial p_v}{\partial y} + 2\mu_v \frac{\partial^2 v_v}{\partial y^2} + \mu_v \left(\frac{\partial^2 u_v}{\partial x \partial y} + \frac{\partial^2 v_v}{\partial x^2} \right) \tag{3}$$

Energy equation

$$\rho_v c_{v,v} \left(u_v \frac{\partial T_v}{\partial x} + v_v \frac{\partial T_v}{\partial y} \right) = k_v \left[\frac{\partial^2 T_v}{\partial x^2} + \frac{\partial^2 T_v}{\partial y^2} \right] \tag{4}$$

2. Governing equations in wick

The governing equation in vapor core was defined as follows. The Darcy's law was apply to momentum equation.

Continuity equation

$$\frac{\partial u_l}{\partial x} + \frac{\partial v_l}{\partial y} = 0 \tag{5}$$

Navier-Stokes equation

$$\rho_l \left(u_l \frac{\partial u_l}{\partial x} + v_l \frac{\partial u_l}{\partial y} \right) = -\frac{\partial p_l}{\partial x} + 2\mu_l \frac{\partial^2 u_l}{\partial y^2} + \mu_l \left(\frac{\partial^2 u_l}{\partial y^2} + \frac{\partial^2 v_l}{\partial x \partial y} \right) - \frac{\mu_l u_l \varepsilon}{K} \tag{6}$$

$$\rho_l \left(u_l \frac{\partial v_l}{\partial x} + v_l \frac{\partial v_l}{\partial y} \right) = -\frac{\partial p_l}{\partial y} + 2\mu_l \frac{\partial^2 v_l}{\partial y^2} + \mu_l \left(\frac{\partial^2 u_l}{\partial x \partial y} + \frac{\partial^2 v_l}{\partial x^2} \right) - \frac{\mu_l u_l \varepsilon}{K} \tag{7}$$

Energy equation

$$\rho_l c_{p,l} \left(u_l \frac{\partial T_l}{\partial x} + v_l \frac{\partial T_l}{\partial y} \right) = k_{eff} \left[\frac{\partial^2 T_l}{\partial x^2} + \frac{\partial^2 T_l}{\partial y^2} \right] \tag{8}$$

3. Governing equations in container wall

The energy equation in the wall is the steady heat conduction equation as follows.

$$\frac{\partial^2 T_s}{\partial x^2} + \frac{\partial^2 T_s}{\partial y^2} = 0 \tag{9}$$

Boundary Conditions

The boundary conditions at both pipe ends are;

$$x = 0; \quad u_v = v_v = u_l = v_l = \frac{\partial T_v}{\partial x} = \frac{\partial T_l}{\partial x} = \frac{\partial T_s}{\partial x} = 0, \quad P_v = P_{ref} = 20.51 \text{ kPa}, \quad T_v = T_{ref} = 333.15 \text{ K}$$

$$x = L; \quad u_v = v_v = u_l = v_l = \frac{\partial T_v}{\partial x} = \frac{\partial T_l}{\partial x} = \frac{\partial T_s}{\partial x} = 0, \quad P_v = P_l$$

The boundary conditions at centerline are;

$$y = 0; \quad u_v = 0, \quad P_v = P_{sat}, \quad T_v = T_l = T_{sat}(P_v)$$

$$\rho_v v_v = \rho_l v_l = \begin{cases} -\frac{Q}{2\pi R_v L_e h_{fg}} \\ +\frac{Q}{2\pi R_v L_c h_{fg}} \end{cases}$$

The boundary conditions at liquid-wall interface are;

$$y = R_w; \quad u_v = v_v = u_l = v_l = 0$$

The boundary conditions at outer wall are;

$$y = R_o; \quad \frac{\partial T_s}{\partial y} = \begin{cases} -\frac{Q}{k_s 2\pi R_o L_e} \\ -\frac{Q}{k_s 2\pi R_o L_c} \end{cases}$$

Materials and Methods

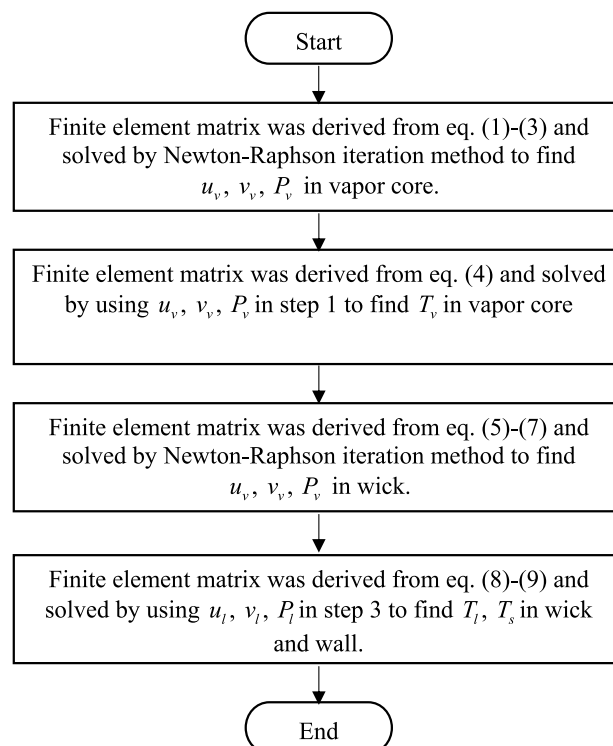


Figure 2 Flow diagram of methodology.

The methodology procedure is illustrated in (Figure 2). The conservation equations and boundary conditions were solved using the finite element method that matrices were derived by using the standard Galerkin approach and used the six-node triangle element. The velocity and pressure distributions in the vapor core were calculated from the equation of continuity and the momentum equations, Eqs. (1) - (3). Next, the temperature distribution in the vapor core was calculated from the energy equation, Eq. (4). The velocity and pressure distributions of liquid in wick were calculated from the equation of continuity and the momentum equations, Eqs. (5), (6), (7). Finally, the temperature distribution of the wick and the wall of container were calculated from the energy equations, Eqs. (8) and (9).

Result and Discussions

To verify this simulation, the results from this simulation were compared with the simulation from N. Thuchayapong¹. The specifications of bend heat pipe used in this simulation are shown in (table 1), with two heat sources (15 Watts and 15 Watts) in the evaporator section that separates by the adiabatic section.

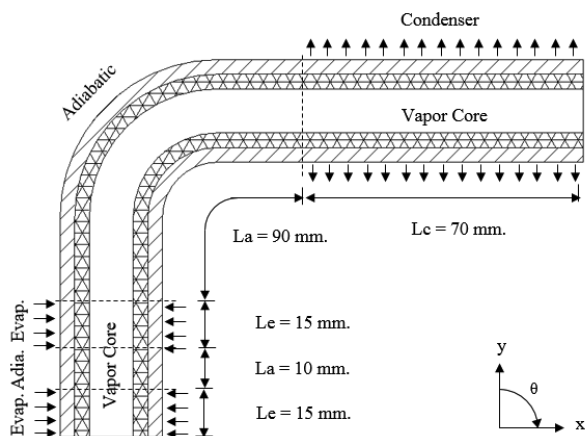


Figure 3 The schematic diagram of the heat pipe and dimension in this simulation.

Table 1 The specifications of bend heat pipe that used in this simulation.

Parameter	Value
Wall Material	Copper
Wick	Screen
Porosity	0.57
Permeability	$1.5 \times 10^{-9} \text{ m}^2$
k_{eff}	1.965 W/mK
Working Fluid	Water
L_e, L_a, L_c	40, 90, 70 mm
R_v, R_w, R_o	2, 2.66, 3 mm.
Bending Angle	90°
$Q_{\text{input}}, Q_{\text{output}}$	30 W

1. Pressure profile

(Figure 4) shows the pressure distributions along the heat pipe in vapor core. The pressure distribution was calculated from the continuity equations, the momentum equations, and the boundary conditions. The vapor pressure in the vapor core was constant at 20.51 kPa that was equal to the saturated pressure at the operating temperature along the heat pipe. From the results, it was shown that the pressure gradient in the vapor core was very small, because the viscosity of vapor is low. And it was founded that the pressure profile trends are in good agreement with the simulation results from N. Thuchayapong¹ that the vapor pressure in vapor core are constant along the heat pipe and equal to the saturated pressure at the operating temperature.

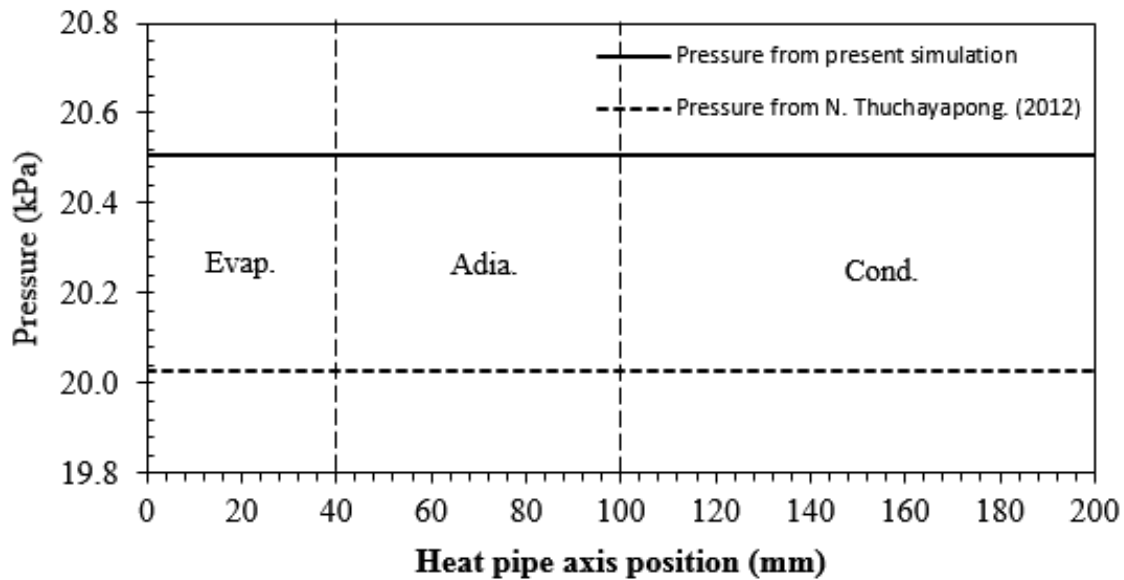


Figure 4 The vapor pressure along the heat pipe.

2. Velocity profile

The average axial velocity of vapor in the vapor core is shown in (Figure 5). The average axial velocity of vapor in the vapor core was calculated from the continuity equations, the momentum equations, and the boundary conditions. The vapor velocity increases from 0 to 7.17 m/s and 7.17 to 14.34 m/s from the end of the evaporator section to the interface between the evaporator and the adiabatic section because of increasing vapor mass from the evaporation of working fluid. The vapor velocity is constant in the adiabatic section because this section doesn't have heat input and output and decreases in the condenser section from 14.34 to 0 m/s

because of decreasing vapor mass from the condensation of working fluid. The vapor velocity at the end of the evaporator section increase quickly from 0 to 7.17 m/s in 15 mm, because the evaporation rate is in proportion to the capillary pressure. But it decrease linearly in the condenser section, because the condensation rate at the liquid-vapor interface in this section is constant at the liquid-vapor interface. It was founded that, the velocity profile trends are in good agreement with the simulation results from N. Thuchayapong¹ that the axial vapor velocity is increased in the evaporator section, constant in the adiabatic section and decrease in the condenser section.

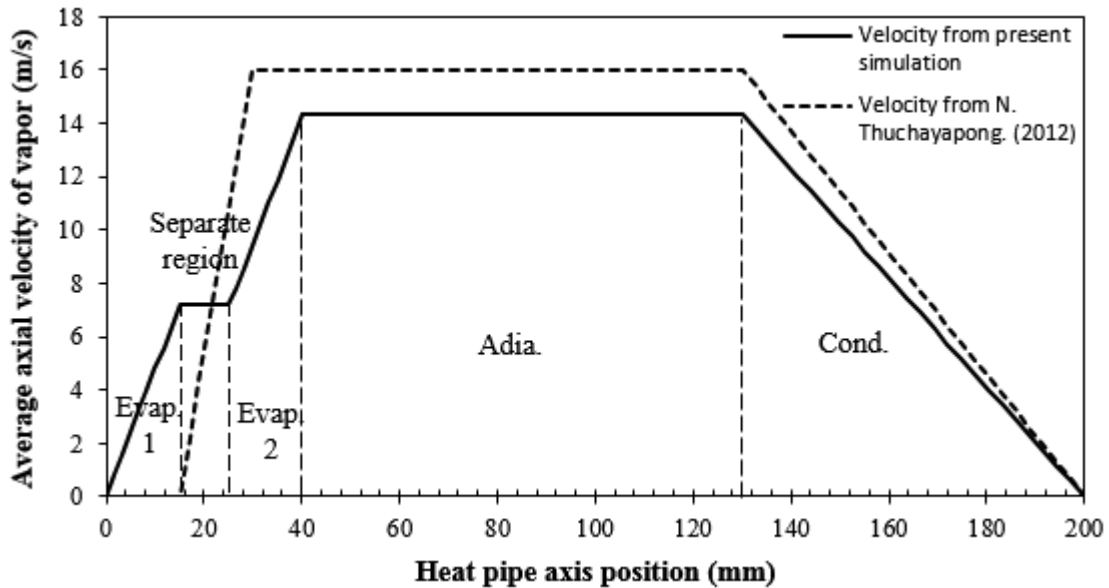


Figure 5 The average axial velocity of vapor along the heat pipe.

Conclusion

The vapor pressure in the vapor core are constant along the heat pipe and equal to the saturated pressure at the operating temperature. Axial vapor velocity increases in the evaporator section, is constant in the adiabatic section and decrease in the condenser section. This simulation was compared with data from from N. Thuchayapong, (2012) and in good agreement.

Acknowledgement

The authors gratefully acknowledge the Chiang Mai University Ph.D. Program (contract number PHD/006/2556) for funding this research.

References

- [1] N. Thuchayapong, Effect of tube bending on heat transfer characteristics of miniature heat pipe with sintered porous media,, 2012, Chiang Mai University, Thailand.
- [2] N. Thuchayapong, P. Terdtoon, P. Sakulchangsattajai, Simulation of Heat Pipe Performance by Using Finite Element Method, International Conference on Science, Technology and Innovation for Sustainable Well-Being (STISWB), 23-24 July 2009, Mahasarakham University, Thailand.
- [3] N. Thuchayapong, A. Nakano, P. Sakulchangsattajai, and P. Terdtoon, Effect of capillary pressure on performance of a heat pipe: Numerical approach with FEM, Applied Thermal Engineering, 32, January 2012, 93-99.
- [4] K.A.R. Ismail, M.A. Zanardi, A steady-state model for heat pipes of circular orrectangular cross-sections, Appl. Therm. Eng. 1996; 16 (8-9) 753-767.
- [5] S.V. Patankar, Numerical Heat Transfer and Fluid Flow. Hemisphere, New York, 1980.

Effect of Working fluids on Thermal Performance of Vertical Closed-loop Pulsating Heat pipe

Piyapong Suvunnajun¹, Niti Kammuang-lue¹, Phrut Sakulchangsattajai¹, Pradit Terdtoon¹

Received: 15 June 2015; Accepted: 13 July 2015

Abstract

This research aims to experimentally investigate the effect of working fluids on thermal performance of vertical closed-loop pulsating heat pipe (VCLPHP) at normal operating conditions. The tested VCLPHP is made from copper capillary tubes with the internal diameter of 2.03 mm. The length of the evaporator, adiabatic and condenser section are equally set as 50 mm. Number of turn are 4 and 12. The evaporator section of the VCLPHPs is heated by a hot bath. The heat is removed from the condenser section by cold bath. The inlet evaporator temperature is controlled at 80 °C. The adiabatic section temperature is controlled at 50 °C. The working fluids used within the VCLPHPs are distilled R141b, Acetone and Ethanol with 50% of the filling ratio. The thermal performance of the VCLPHP is evaluated by calculating the rate of heat transferred to cold bath at condenser section. It is found that, for 4 turn numbers, when working fluid is changed from R141b ($h_{fg} = 267$ kJ/kg) to Acetone ($h_{fg} = 526$ kJ/kg) and Ethanol ($h_{fg} = 1000$ kJ/kg), heat flux continuously increases from 24 to 42 and 54 kW/m² respectively. This might be because with the higher latent heat, the evaporation rate at evaporator section and condensation rate at condenser section are increased. The heat flux is accordingly increased. For 12 turn numbers, when working fluid changes from R141b ($h_{fg} = 267$ kJ/kg) to Acetone ($h_{fg} = 526$ kJ/kg), heat flux continuously increases from 41 to 50 kW/m². In contrast, when working fluid changes from Acetone ($h_{fg} = 526$ kJ/kg) to Ethanol ($h_{fg} = 1000$ kJ/kg), heat flux continuously decreases from 50 to 46 kW/m². Since there may be other factors besides latent heat involved.

Keywords: Vertical closed-loop pulsating heat pipe, Working fluids, Thermal performance

Introduction

A pulsating heat pipe (PHP) is a heat transfer device that can work without external power. The working fluid inside the pulsating heat pipe is a medium of the heat transfer. The PHPS can provide high thermal performance. Therefore PHP are used in industrial and electronic equipment. The PHP was firstly invented by Akachi, et al.¹. The PHP is made from capillary tube with meandering bent. The PHP is evacuated and filled with working fluids. The arrangement of the working fluid inside forms into liquid slugs alternating with vapor plugs along the entire length of the tube. The operation of the PHP is Pulsating movement of working fluid and phase change phenomena when heat input at evaporator section and heat remove at condenser section. The PHP can be

divided into three types. The first close-end pulsating heat pipe (CEPHP) as shown in (Figure 1(a)). The second closed-loop pulsating heat pipe (CLPHP) as shown in (Figure 1(b)). The third closed-loop pulsating heat pipe with check valve as shown in (Figure 1(c)). This research will study closed-loop pulsating heat pipe due to heat transfer performance being more than a closed-end pulsating heat pipe, and easier to produce than closed-loop pulsating heat pipe with check valve.

Charoensawan et al.², studied experimentally a wide range of pulsating heat pipes thereby providing vital information on the parameter dependency of their thermal performance. The influence characterization has been done for the variation of internal diameter, number of turns, working fluid and inclination angle of the device.

¹ Department of Mechanical Engineering, Faculty of Engineering, Chiang Mai University, Chiang Mai, Thailand, 50200
Tel: +66 86 9140818, Fax: +66 53 226014, E-mail: kongpiyaponk@gmail.com

CLPHPs are made from copper tubes of internal diameters 2.0 and 1.0 mm. The number of turns in the evaporator is varied from 5 to 23. The working fluids used within the CLPHPs are distilled water Ethanol and R123. The results indicate a strong influence of gravity and number of turn on the performance. The thermodynamic properties of working fluids affect the performance which also strongly depends on the boundary conditions of PHP operation.

On-ai et al.⁴, studied experimentally the effect of working fluid types on thermal performance of closed-loop pulsating heat pipe. CLPHPs are made from copper tubes of internal diameters 1.50, 1.78 and 2.16 mm. The number of turns is 26. The working fluids used within the CLPHPs are distilled R123, R141b, Acetone, Ethanol and Water. It was found that Karman number (Ka), Aspect ratio (L_e / D_i) and Prandtl number (Pr_{liq}) can reasonably represent the effect of working fluid types on thermal performance of the CLPHPs through a term of kutateladze number (Ku). From relations between these dimensionless numbers and Ku , the correlation was successfully established.

Sriwiset et al.⁵, study evaluation of optimum turn numbers for closed-loop pulsating heat pipe. CLPHPs are made from copper tubes of internal diameters 2.03 mm. Number of turns are 5, 10, 16 and 30. It was found that the CLPHP operation depends on many factor's parameters. They have conducted an analysis to evaluate the thermal performance in the form of dimensionless parameters, e.g. are Ku , Pr_{liq} , Ja , Ka , N . They analyzed experimental data combined with Charoensawan et al.², Khandekar et al.³ and On-ai et al.⁴ as shown in Equation (3). It was found that when dimensionless parameter on horizontal axis, namely $f(ka^{0.47} Ja^{1.43} N^{-0.27})$, is 50000. CLPHP can operation optimum at its highest thermal performance.

Pulsating heat pipe design can provide better thermal performance depending on many variables. In the past study, it was found that there was a lack of information of the effect of working fluids. In this research, therefore, we aimed to experimentally investigate the effect of working fluids on thermal performance of a vertical closed – loop pulsating heat pipe.

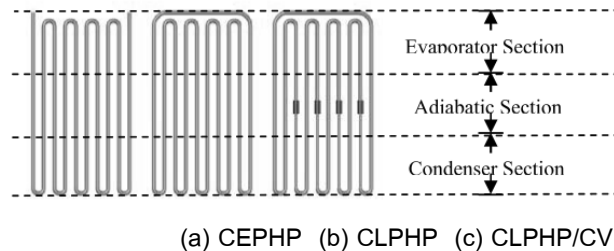


Figure 1 Three types of Pulsating heat pipe

Experimental Setup and Procedure

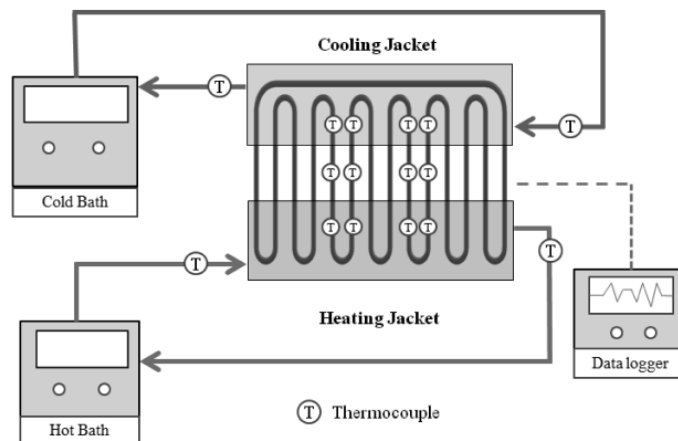


Figure 2 Experimental Setup

The CLPHPs used in the experimental were made of long capillary tubes with inner diameters 2.03 mm. The length of the evaporator, adiabatic and condenser section were equally set as 50 mm. Number of turns were 4 and 12. The inlet evaporator temperature were maintained at 80 °C (Haake, N6, accuracy ± 0.01 °C). The heat was removed from the condenser section by cold bath (Bitzer, D7032, accuracy ± 1 °C). The adiabatic section temperature was maintained at 50 ± 5 °C. The working fluids used within the VCLPHPs were distilled R141b, Acetone and Ethanol with 50% to the filling ratio. A schematic diagram of the experimental setup is shown in (Figure 2). Twenty thermocouples (Omega, type k, accuracy ± 0.5 °C) are installed on the outer surface of the capillary tube to measure the variation in temperature. The temperature was monitored by a data logger (Brainchild VR18, accuracy ± 0.1 °C). Setup thermocouple 4 points on the middle on each tube in the evaporator section, 4 point in the adiabatic section, 4 points in the condenser section. Two points are installed on each inlet and outlet tube of the heating and cooling jacket. By record every 1 second. The thermal performance of the VCLPHP was evaluated by calculating the rate of heat transferred at cooling jacket in the condenser section When the operation into steady state condition. By Calorific Method as equation (1).

$$\dot{q} = \frac{\dot{m} C_p (T_{out} - T_{in})}{A_c} \quad (1)$$

Where \dot{q} is heat flux, \dot{m} is mass flow rate of the cooling, C_p is the specific heat, $(T_{out} - T_{in})$ is the difference in the temperature of the cooling, A_c is the inner surface area of the tube in the condenser section.

Because of these values received from the instruments. It is important to check for errors due to this measure to analyze the results correctly. The error of the heat flux can be calculated by equation (2).

$$d\dot{q} = \sqrt{\left(\frac{\partial \dot{q}}{\partial \dot{m}} d\dot{m}\right)^2 + \left(\frac{\partial \dot{q}}{\partial T_{out}} dT_{out}\right)^2 + \left(\frac{\partial \dot{q}}{\partial T_{in}} dT_{in}\right)^2} \quad (2)$$

Where $d\dot{q}$ is the error of the heat flux, $d\dot{m}$ is the accuracy from measuring the mass flow rate of the cooling, dT_{out} and dT_{in} are the accuracy from measuring the outlet and inlet of water cooling. In this study, the heat flux of which the error calculated from equation (2) was lower than 30% of calculated heat flux from equation (1) which defined the criteria to be analyzed in the next step.

Results and Discussions

1. Effect of Working fluids

In a study on effect of working fluids on heat flux, it is necessary to identify each of the working fluids by quantitative parameters They are the thermodynamic properties of the working fluid such as latent heat of evaporation, specific heat, surface tension, viscosity, thermal conductivity, etc. Since the CLPHP transfers heat by the evaporative and condensation mechanism of the working fluids, the most suitable parameter to identify the difference of the working fluid in this topic is the latent heat of evaporation (h_{fg}). R141b, Acetone and Ethanol were chosen to be variable parameters with the latent heat of evaporation of 267, 526 and 1000 kJ/kg respectively.

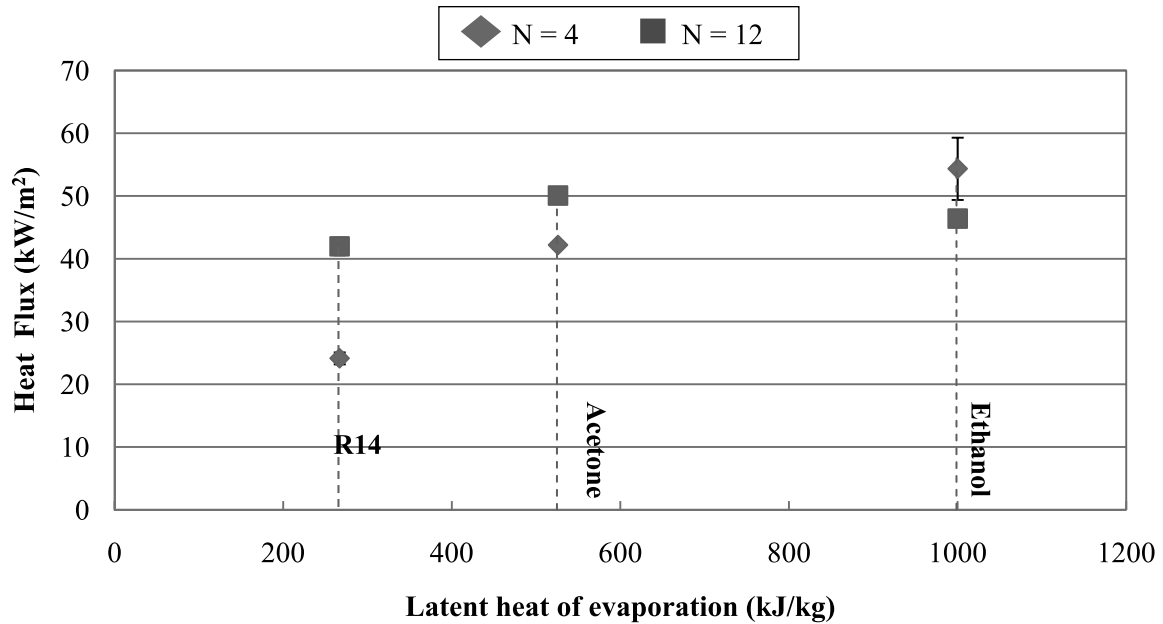


Figure 3 Effect of latent heat on heat flux (Vertical CLPHP, $D_i = 2.03\text{mm}$, $L_e = 50\text{ mm}$)

(Figure 3) shows effect of latent heat on the heat flux of the CLPHP. It can be seen from the experimental results that, for number of turns is 4 when working fluid changes from R141b ($h_{fg} = 267\text{ kJ/kg}$) to Acetone ($h_{fg} = 526\text{ kJ/kg}$) and Ethanol ($h_{fg} = 1000\text{ kJ/kg}$), heat flux continuously increases from 24 to 42 and 54 kW/m^2 respectively.

This might be because when the latent heat increases, the evaporative rate, and also the condensation rate, is increased. The heat flux is accordingly increased.

This trend is quite similar to those obtained by On-ai et al.⁴ as they did the experiments with R141b Acetone Ethanol as working fluids and tubes internal diameter of 1.50 mm. They found that, the heat flux increases with the increasing of latent heat.

(Figure 3) shows the effect of latent heat on the heat flux of the CLPHP. It can be seen from the experimental results that, when number of turns is 12 when working fluid changes from R141b ($h_{fg} = 267\text{ kJ/kg}$) to Acetone ($h_{fg} = 526\text{ kJ/kg}$), heat flux continuously increases from 41 to 50 kW/m^2 . In contrast, when working fluid changes from Acetone ($h_{fg} = 526\text{ kJ/kg}$) to Ethanol ($h_{fg} = 1000\text{ kJ/kg}$), heat flux continuously decreases from 50 to 46 kW/m^2 .

This might be because there are other factors involved besides latent heat. When the latent heat increases it does not mean that thermal Performance will increase always.

This trend is quite similar to those obtained by On-ai et al.⁴ as they did the experiments with R141b Acetone Ethanol as working fluids and tubes with internal diameter of 2.16 mm. They found that, when working fluid changes from R141b to Acetone, heat flux is increased. And when working fluid changes from Acetone to Ethanol, heat flux is decreased.

From the experimental data it is found that, when working fluid changes from R141b ($h_{fg} = 267\text{ kJ/Kg}$) to Acetone ($h_{fg} = 526\text{ kJ/Kg}$), heat flux continuously increases from 41 to 50 kW/m^2 . In contrast, when working fluid changes from Acetone ($h_{fg} = 526\text{ kJ/kg}$) to Ethanol ($h_{fg} = 1000\text{ kJ/kg}$), heat flux continuously decreases from 50 to 46 kW/m^2 .

2. Correlation to Predict Thermal Performance

Verification of the experimental data

The CLPHP depends on many parameters. In past studies, Sriwiset et al.⁵ conducted an analysis to evaluate the thermal performance in the form of dimensionless parameters, e.g. are Ku , Pr_{liq} , Ja , Ka , N . Sriwiset et al.⁵ analyzed experimental data with Charoensawan et al.²,

Khandekar et al.³ and On-ai et al.⁴ as shown in Equation (3). In this work have to analyzie. The verification of recent experimental data with previously existing data is shown in (Figure 4).

$$Ku = f(ka^{0.47} Pr_{liq}^{0.27} Ja^{1.43} N^{-0.27}) \quad (3)$$

Where Ku is Kutateladze number, Ka is Karman Number, Pr_{liq} Prandtl Number of liquid, Ja is Jacob Number, N is number of turn.

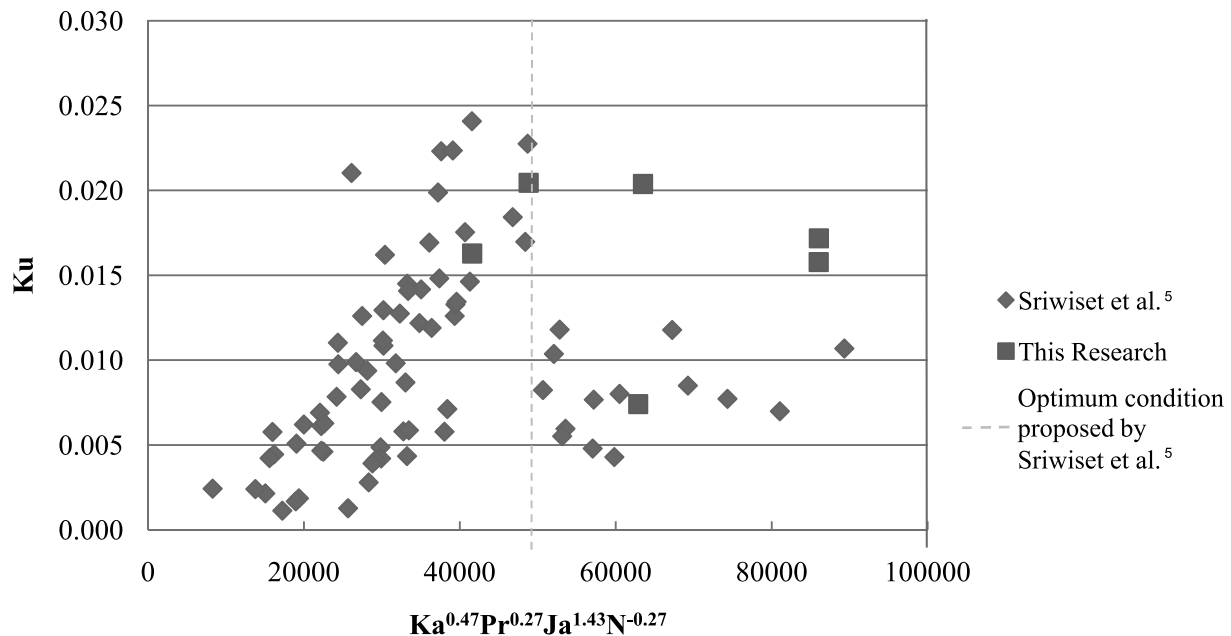


Figure 4 function of dimensionless in Equation (3) use to evaluation thermal performance

(Figure 4) shows the function of verification of experimental data in dimensionless form suggested in Equation (3). It can be seen that, from the results of past studes and combined with this research, when dimensionless parameter on horizontal axis, namely $f(ka^{0.47} Ja^{1.43} N^{-0.27})$, is 50000 (the optimum condition proposed by Sriwiset et al.⁵), CLPHP can operate optimum at its highest thermal performance. Since dimensionless parameter $f(ka^{0.47} Ja^{1.43} N^{-0.27})$ is 50000, Ku has a maximum value. This trend is quite similar to those obtained by Sriwiset et al.⁵ as they used their equation (3) and they found that, when dimensionless $f(ka^{0.47} Ja^{1.43} N^{-0.27})$ is 50000 the CLPHP can operate at optimum thermal performance. Since Ku has a maximum value.

Conclusion

1. Effect of working fluids on thermal performance of vertical closed-loop pulsating heat pipe. It was

found that for 4 turn numbers when latent heat increases, heat transfer flux increases. This might be because when the latent heat increases, the evaporative rate, and also the condensation rate, is increased. The heat flux is accordingly increased. For 12 turn numbers when latent heat increases, the heat transfer flux increased and then decreased. This might be because other factors involved besides latent heat. When the latent heat increases it does not mean that thermal Performance will always increase.

2. Because the CLPHP depends on many factors. In past studies, Sriwiset et al.⁵ have analyzed to evaluate the thermal performance in the form of dimensionless are Ku, Pr_{liq}, Ja, Ka, N as shown in Equation (3). It can be seen from the results of the past study and combined with this research, when dimensionless $f(ka^{0.47} Ja^{1.43} N^{-0.27})$ is 50000, CLPHP can operation optimum thermal performance. Since Ku has a maximum value.

Acknowledgement

This research has been supported by Faculty of Engineering, Chiang Mai University, Heat Pipe and Heat System Laboratory, Research and Researcher for Industry (Contract number MSD57I0158), Fujikura Electronics (Thailand).

References

- [1] Akachi, H., Polasek, F. and Stulc, P., Pulsating Heat Pipe. Proc. of the 5th International Heat Pipe Symposium. Melbourne Australia, 1995; 208-217.
- [2] Chareonsawan, P., Khandekar, S., Groll, M. and Terdtoon, P., Closed-Loop Pulsating Heat Pipe Part A: Parametric Experimental Investigations. Applied Thermal Engineering. 2003; 23: 2009-2020.
- [3] Khandekar, S., Chareonsawan, P., Groll, M. and Terdtoon, P., Closed-Loop Pulsating Heat Pipe Part B: Visualization & semi-empirical modeling. Applied Thermal Engineering. 2003; 23: 2021-2033.
- [4] On-ai, K., Kammuang-lue, N., Terdtoon, P., and Sakulchangsattajai, P., Effect of Working Fluid Types on Thermal Performance of Vertical Closed-Loop Pulsating Heat Pipe. Proc. of the 5th International Conference on Science. Luang Prabang Lao PDR. 2013; 5: 24.
- [5] Sriwiset, C., Kammuang-lue, N., Sakulchangsattajai, P. and Terdtoon, P., Evaluation of Optimum Turn Number for Closed-Loop Pulsating Heat Pipe at Normal Operation. Proc. of the 5th International Conference on Science. Luang Prabang Lao PDR. 2013; 5: 26.

Performance of Carbide Cutting Tool Coated DLC and TiAlN to Wear Protection on Cutting Edge

Paramet Baowan¹

Received: 23 June 2015; Accepted: 13 July 2015

Abstract

Cutting edge is one of the major factors affecting the tool life of cutting tools. To increase the tool life of cutting tools, keeping the slowest wear of cutting edge must be focused. Hard coating is one of popular wear protection methods on cutting edge, which aims to increase the efficiency of cutting tools, such as increasing cutting speed, resisting tool wear and high thermal, increasing tool life and high quality surface roughness. The main objectives of this work are to present the analysis of influences of the coating materials affecting the surface roughness and wear protection on cutting edge by comparison between the cutting tools coated by DLC and TiAlN. The research found that these of coating materials influence to the surface roughness and wear protection on cutting edge in stainless steel machining.

Keywords :Stainless steel, Tool life, Surface roughness

Introduction

Cutting edge is one of the major factors affecting the tool life of cutting tools¹. To increase the tool life of cutting tools, keeping the slowest wear of cutting edge must be focused. Hard coating is one of popular wear protection methods on cutting edge, which aims to increase the efficiency of cutting tools, such as increase cutting speed, resistant tool wear and high thermal, increase tool life and high quality surface roughness. This method has been used since the 1960 for increasing tool life of cutting tool². Several research have been conducted to find coatings techniques and coating materials for improving cutting tools in machining process. Biermann, al et³ investigation of different material coatings CrN, TiN, AlCrN, AlTiN and TiAlN on carbide cutting tool, It was found that the TiAlN and AlCrN were the most efficient wear resistant. Liew⁴ compared carbide cutting tool coated between TiAlN single-layer and TiAlN/AlCrN nano-multilayer and found that TiAlN/AlCrN increased the tool life more than TiAlN single-layer. Aramcharoen et al⁵ represent the different coating material TiN, TiCN, TiAlN, TiAlCrN for increasing wear resistant and improving surface quality in machining hard material. It showed that the types

of coating materials influence to the wear rate when compared with uncoated materials.

However, the previous research did not compare the performance of carbide cutting tool coated by DLC with TiAlN. The main objectives of this work are to present the analysis of influences of the coating materials affecting to the surface roughness and wear protection on cutting edge by comparison between the cutting tools coated with DLC and TiAlN.

Materials and Methods

Material used was stainless steel grade 304L. Flank end mill carbide having a nominal diameter 10 mm, 4 cutting edges in (Figure 1), and coated with DLC and TiAlN are the properties in (Table 1). Side milling machining by high speed vertical machining centre Haas VM02 and experiment setup in (Figure 2). Cutting conditions were : cutting speed $V_c = 120 \text{ m min}^{-1}$; axial depth of cut = 20 mm ; radial depth of cut = 0.2 mm ; feed = 0.05 mm/tooth ; cooling with air. Surface roughness measuring by Mitutoyo SJ210 stylus and tool wear examined by the scanning electron microscope (SEM).

¹ Department of Industrial Engineering, Faculty of Engineering, Rajamungala University of Technology IsanKhonKaen Campus, E-mail: paramet_ie@hotmail.com

Table 1 Coating properties

Coating materials	TiAlN	DLC
Film thickness (μm)	2.87	1.12
Hardness (Hv)	2300	3000
Friction	0.45	0.1

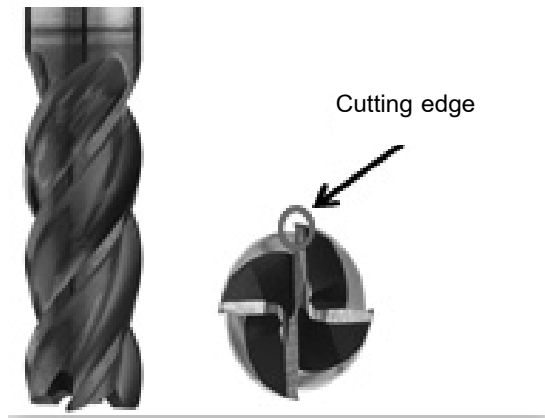


Figure 1 Flank end mill carbide geometry

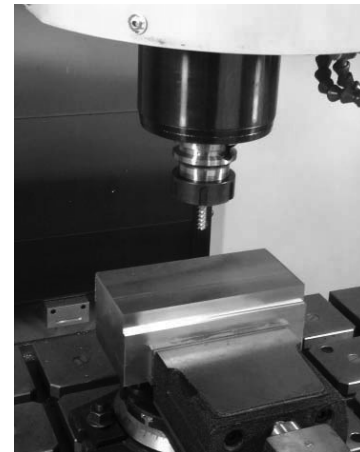


Figure 2 Experiment setup

Results and Discussions

1. Surface roughness

(Figure 3) shows the comparison of surface roughness machining by flank end mill carbide coated with DLC and TiAlN during cutting length 10-50 m. Measuring surface roughness in parallel feed direction by

Mitutoyo SJ210 stylus ISO 1997. It can be seen that surface roughness of flank end mill carbide with DLC better than TiAlN and uncoated, due to friction and film thickness properties of DLC was better than TiAlN leading to high performance in machining stainless steel

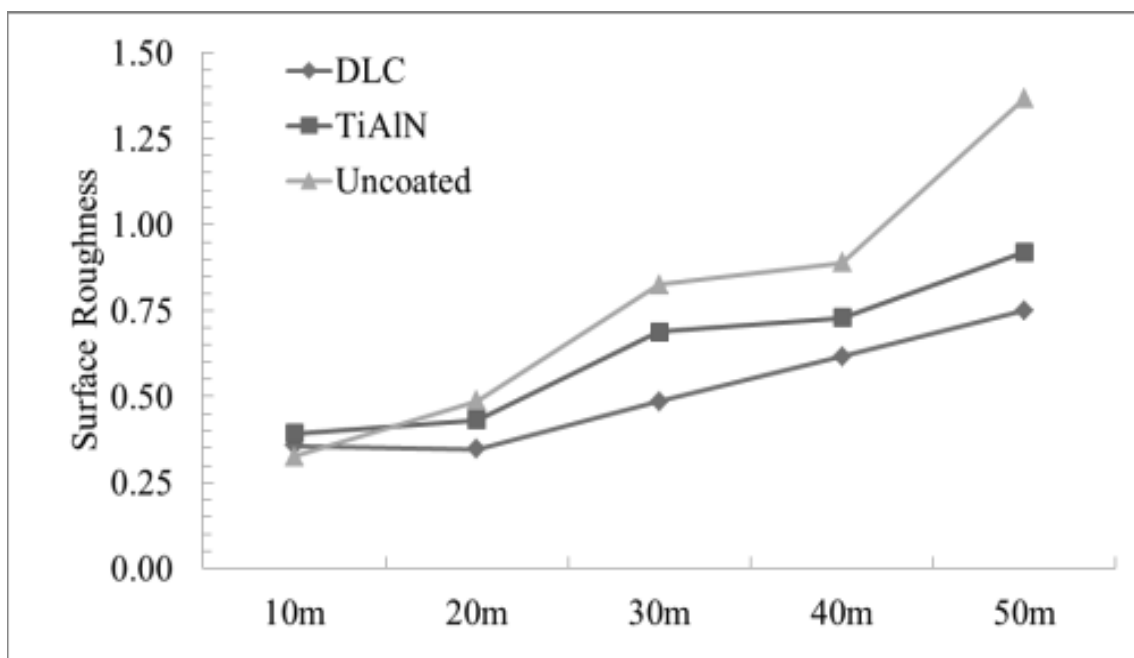


Figure 3 Comparison of surface roughness

2. Tool wear

From (Figure 4) the wear on cutting edge examined by SEM expanding 800x after cutting length 50 m., It was found that the severity of wear was not equal. This indicates that the kind of coating material influence to wear protection on cutting edge. It was also found that the chipping on cutting edge of uncoated and DLC,

has the ability to prevent less chipping than TiAlN, which causes the short tool life. However, it was found the flank wear on flank face, but it has less intensity. Due to good adhesion properties of TiAlN³⁻⁷ which leading to increase tool life. Therefore, the TiAlN can perform the wear protection on cutting edge better than DLC and uncoated in the stainless steel machining.

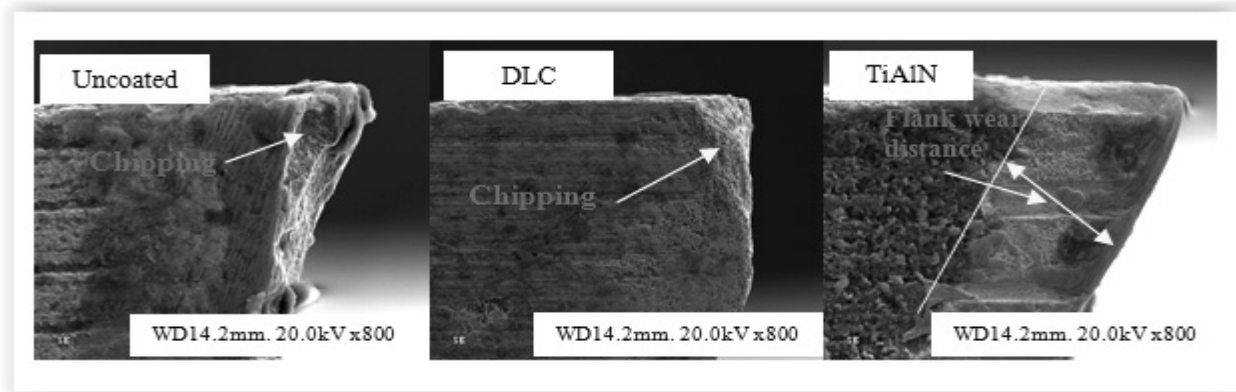


Figure 4 Wear on cutting edge after cutting length 50 m

Conclusion

The comparison of cutting performance off the flank end mill carbide coated with DLC, TiAlN and uncoated on quality of surface roughness and wear protection on cutting edge. The following results are obtained.

1. Types of coating materials influence to the surface roughness and wear protection on cutting edge in stainless steel machining.

2. Flank end mill carbide coated with DLC when machining stainless steel. The surface quality will be better than the TiAlN and uncoated.

3. The TiAlN can perform the wear protection on cutting edge better than DLC and uncoated in the stainless steel machining.

From above summary the DLC-coated cutting tools are suitable for applications required good surface roughness. But the TiAlN-coated are suitable for applications required to increase tool life.

Acknowledgement

The authors are grateful to the Faculty of Engineering, Rajamungala University of Technology Isan Khon Kaen Campus for their valuable support.

References

- [1] Bouzakis, K.D., S.Makrimalakis, G.Skordaris, E.Bouzakis, S. Kombogiannis, G. Katirtzoglou, G.Maliaris. 2013. Coated tools' performance in up and down milling stainless steel, explained by film mechanical and fatigue properties. *Wear*. 303; 546–559.
- [2] Veprek, S., Maritz, J.G., Veprek-Heijman. Industrial applications of super hard nanocomposite coatings. *Surface & Coatings Technology*. 2008; 202; 5063–5073.
- [3] Biermann, D., Markus Steiner, Eugen Krebs. Investigation of Different Hard Coatings for Micromilling of Austenitic Stainless Steel. *CIRP Conference on Manufacturing Systems. Procedia CIRP* 7; 2013; 246 – 251.
- [4] Liew, W.Y.H. Low-speed milling of stainless steel with TiAlN single-layer and TiAlN/AlCrN nano-multi-layer coated carbide tools under different lubrication conditions. *Wear*. 2010; 269; 617–631.
- [5] Aramcharoen, A., Mativenga, Yang, P.S., Cooke, K. and Teer, D. Evaluation and selection of hard coatings for micro milling of hardened tool steel, *International Journal of Machine Tools and Manufacture*. 2010; 48 (14) 1578–1584

- [6] Aramcharoen, A., Mativenga P. and Yang, S. 2007.
The contribution CrTiAlN coatings in micromilling of hardened die steel, in: Proceedings of the 40th CIRP International Seminar on Manufacturing Systems. Liverpool. UK.
- [7] Aramcharoen, A., Mativenga, P. and Yang, S. 2007.
The effect of AlCrTiN coatings on product quality in micro-milling of 45 HRC hardened H13 die steel, in: Proceedings of the 35th International Matador Conference. Taipei.

FEM Study of Velocity Profile of Flattening Heat Pipe with Multiple Heat Sources

Sophon Sinsang¹, Niti Kammuang-lue¹, Phrut Sakulchangsatajai¹, Pradit Terdtoon¹

Received: 15 June 2015; Accepted: 13 July 2015

Abstract

A heat pipe is a simple device that can transfer large quantities of heat over fairly long distances at nearly a constant temperature. The application of heat pipes in thermal management of electronics has increased enormously in recent years due to the limited space existing on printed circuit board (PCBs) and increasing power density. Formerly, a single heat pipe designed is used for heat transfer from both a central processing unit (CPU) and a graphics processor unit (GPU). Normally, because of the limited space for cooling, flattened heat pipes have been widely used, but the problem is that as heat pipes become thinner the heat transfer rate is reduced making it difficult to cope with smaller, thinner equipment. Thus, in this research, we numerically study the effect pipe flattening on heat transfer characteristics of miniature sintered porous media heat pipe with multiple heat sources by using Finite Element Method (FEM). The governing equations, i.e. continuity, momentum, and energy equations, and boundary conditions, were solved by using the Finite Element Method (FEM), while matrices were derived from these equations using the Galerkin approach. In the mathematical model, vapor flows are assumed to be steady, laminar flow and incompressible. The wick is assumed isotropic and saturated with the working liquid. The final flattened thickness was 2.5, 3 and 4 mm when the original diameter of the heat pipe was 6 mm. Total length of heat pipe was 200 mm. The operating temperature was 60 °C. The model of the flattened heat pipe was composed of the evaporator section with two heaters which have distance between the heat sources were 0, 25, 50, and 75 mm, respectively. The ratios of heat input power were controlled at 10W:10W, 20W:10W and 30W:10W. It was noted that, when power input of first heater was increased from 10W to 30W, the vapor velocity increased from 21.93 to 44.24 m/s at the end of the second evaporator section due to the mass transfer of vapor was the highest. When the tubular heat pipe is flattened to 4, 3 and 2.5 mm, the vapor velocity profile highest increased were 30.16 m/s, 43.87 m/s, and 75.91 m/s, respectively. Due to the cross section area of vapor core was smaller. And, when the first evaporator section overlapped with second evaporator section (distance 0 mm), the vapor velocity increases to 42.43 m/s due to the heat accumulated from both heat sources.

Keywords: finite element method, flattened heat pipe, final thickness, multiple heat sources

Introduction

The heat pipe is a simple device of very high thermal conductance. It can transmit heat at high rate over considerable distances with extremely small temperature drop. The decreasing size of electronic devices and their increasing power has led to the need for higher heat fluxes to be dissipated in a small space. Heat pipes are also attracting more and more attention as promising devices to meet electronic cooling requirements. This is

due to the ability of heat pipes to transfer large amounts of heat over long distances at low temperature drops¹. Recently, most electronic equipment tends to be thinner and lighter, so a heat pipe, which is used as thermal solution to cool down heat source, needs to be thinner and lighter too. But heat pipes have unfavorable features that thermal performance becomes worse when heat pipe is flattened. When heat pipe is flattened, pressure drop originated in vapor and liquid flow are increased remark-

¹ Department of Mechanical Engineering, Faculty of Engineering, Chiang Mai University, Thailand 50200. Tel. +66-53-944151 Fax. +66-53-226014
E-mail: sophon_sin@hotmail.com

ably because of narrow space for vapor and liquid flow²⁻³. Conventionally, heat pipe has been installed on each heater individually. However recently, only one heat pipe may be installed on multiple heaters^{1,4}.

Many studies for heat pipe with multiple heat sources have been performed by Chen and Faghri⁵ they investigated the behavior of heat pipe with two heat sources. Faghri and Buchko⁶ studied the dry-out condition of the heat pipe with four heat sources. In reviews of above literature, researches were mostly limited to fixed multiple heat sources and could not even cover the heat source on flattened heat pipe. In this research, we studied the Velocity Profile of Flattening Heat Pipe with Multiple Heat Sources using the Finite Element Method (FEM).

Materials and Methods

In this study, the mathematical model of heat pipe was established by using the finite element method. Assumptions of mathematical model simulation were shown as follows, to find vapor velocity, pressure and temperature.

- The working fluid was Newtonian fluid.
- Wick was saturated with liquid.
- The vapor was incompressible and had laminar flow
- Flow and heat transfer were at a steady state.

1. Governing equations

The governing equations in the vapor core region include the conservation of mass, momentum and energy equations as follows :

Conservation of mass equation:

$$\frac{\partial u_v}{\partial x} + \frac{\partial v_v}{\partial y} + \frac{\partial w_v}{\partial z} = 0 \quad (2)$$

Momentum equation:

$$0 = -\frac{\partial P_v}{\partial x} + 2\mu_v \frac{\partial^2 u_v}{\partial x^2} + \mu_v \left(\frac{\partial^2 u_v}{\partial y^2} + \frac{\partial^2 u_v}{\partial z^2} + \frac{\partial^2 v_v}{\partial x \partial y^2} + \frac{\partial^2 w_v}{\partial x \partial z^2} \right) \quad (2)$$

$$0 = -\frac{\partial P_v}{\partial y} + 2\mu_v \frac{\partial^2 v_v}{\partial y^2} + \mu_v \left(\frac{\partial^2 u_v}{\partial x \partial y^2} + \frac{\partial^2 v_v}{\partial y \partial z^2} + \frac{\partial^2 v_v}{\partial x^2} + \frac{\partial^2 w_v}{\partial y^2} \right) \quad (3)$$

$$0 = -\frac{\partial P_v}{\partial z} + 2\mu_v \frac{\partial^2 w_v}{\partial z^2} + \mu_v \left(\frac{\partial^2 u_v}{\partial x \partial z^2} + \frac{\partial^2 v_v}{\partial y \partial z^2} + \frac{\partial^2 w_v}{\partial x^2} + \frac{\partial^2 w_v}{\partial y^2} \right) \quad (4)$$

Conservation of energy includes conductive and convective heat transfer of fluid flow.

In vapor core:

$$\rho_v C_{v,v} \left(u_v \frac{\partial T_v}{\partial x} + v_v \frac{\partial T_v}{\partial y} + w_v \frac{\partial T_v}{\partial z} \right) = k_v \left[\frac{\partial^2 T_v}{\partial x^2} + \frac{\partial^2 T_v}{\partial y^2} + \frac{\partial^2 T_v}{\partial z^2} \right] \quad (5)$$

In wick and wall:

$$0 = k_{eff} \left[\frac{\partial^2 T_s}{\partial x^2} + \frac{\partial^2 T_s}{\partial y^2} + \frac{\partial^2 T_s}{\partial z^2} \right] \quad (6)$$

The governing equations in wick and wall regions were the steady state heat conduction equations. Therefore, the convective heat transfer was neglected in the wick region.

2. Boundary conditions

The boundary conditions of the vapor flow in flattened heat pipe were observed that at the liquid-vapor

interface, a non-slip condition ($u_v = v_v = w_v = 0$) was assumed. The heat input of each heater was received by evaporation at liquid-vapor interface in each evaporation section. Total heat output (Q_{HT1}, Q_{HT2}) was released by condensation at liquid-vapor interface in the condenser section. Then, the average vapor velocity of flattened heat pipe with double heat sources was given as follows:

Evaporator section:

$$v_{e,1} = \frac{Q_{HT1}}{\rho_v \times W_s \times L_{e,1} \times h_{fg}} \tag{7}$$

$$v_{e,2} = \frac{Q_{HT2}}{\rho_v \times W_s \times L_{e,2} \times h_{fg}} \tag{8}$$

Condenser section:

$$v_c = \frac{Q_{HT1} + Q_{HT2}}{\rho_v \times W_s \times L_c \times h_{fg}} \tag{9}$$

Where:

Q_{HT1}, Q_{HT2} = Heat power input, W

$v_{e,1}, v_{e,2}$ = Average vapor velocity at evaporator section, m/s

v_c = Average vapor velocity at condenser section, m/s

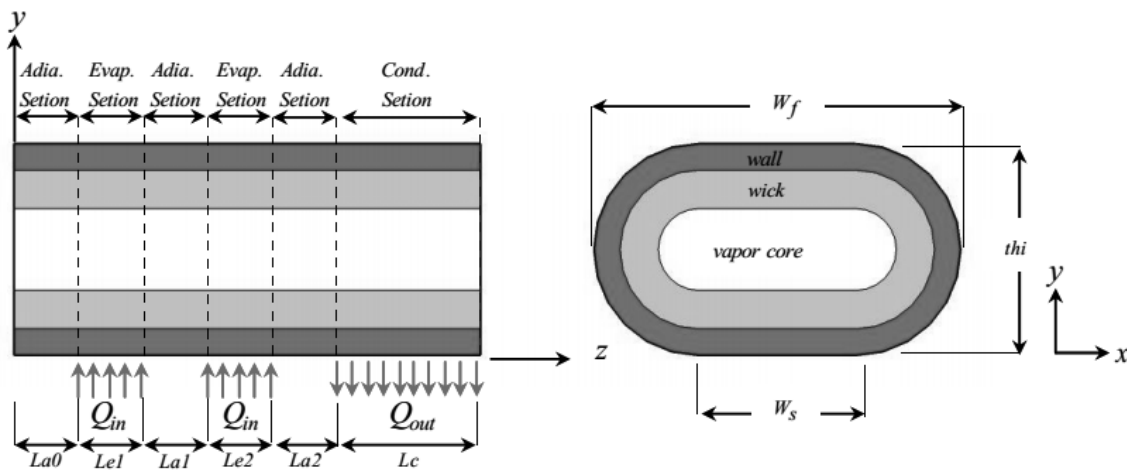


Figure 1 Schematic of a flattened heat pipe and the coordinate system

The specifications of the heat pipes used are shown in (Table 1.) the outside diameter and the total length of the heat pipe were 6 mm and 200 mm, respectively. The lengths of the evaporator section, and condenser section, were 15 mm, and 70 mm respectively. Water is chosen as the working medium. The wick and wall are made of copper. The wick porosity of 0.57 with the voids being saturated with water. The thickness of the wick is 0.70 mm. The thickness of the wall is 0.30 mm. The effective thermal conductivities of the composite wick and copper are 5.97 W/mK and 400 W/mK, respectively. The operating temperature is controlled at 60 °C. W_f is

the wide of flattened heat pipe, this is the final thickness of flattened heat pipe, W_s is the width of surface that contacted the heat source or heat sink. In this study, the final thickness of flattening heat pipe was 2.5, 3 and 4 mm. The method for solving equations started from generating the grids of domains. Next, the governing equations are solved by using the FEM. The conservation of mass, and momentum energy equations in equation (1) to equation (4) are solved in the vapor core region. Finally, the vapor velocity distribution of the flattening heat pipe is obtained.

Table 1 Specifications of heat pipe used for model verification.

Specification	value
Container material	Copper
Wick material	Copper
Wick type	Groove + Powder sintered wick
Working fluid	Water
Total length	200 mm
Outside diameter	6 mm
Number of heaters	2
Evaporator length	15 mm
Condenser length	70 mm
Wick porosity	0.57
Wick thickness	0.70 mm
Wall thickness	0.30 mm
Effective thermal conductivity of wick	5.97 W m ⁻¹ K ⁻¹
Effective thermal conductivity of copper	400 W m ⁻¹ K ⁻¹
Operating temperature	60 °C

The uniform temperature condition ($T_v = T_l$) was assumed at the liquid-vapor interface, in both the evaporator and condenser sections. The temperature at this interface is equal to the saturated temperature of vapor pressure ($T_v = T_l = T_{sat@P_v}$). At both pipe ends, the insulated boundary condition was assumed ($\partial T_v / \partial n = \partial T_l / \partial n = \partial T_s / \partial n$) and the fluid velocity was equal to zero ($u_v = u_l = v_v = v_l$). The end of the evaporator section was defined to be a reference by setting the reference temperature to be equal to the operating temperature of the heat pipe.

The reference pressure was also assumed to be equal to the saturated pressure at the operating temperature ($p_v = P_{sat@T_v}$). At the wick-wall interface, the non-slip boundary condition was assumed ($u_v = v_v = 0$), and the following energy balance was at the interface, $k_s (\partial T / \partial n)_{wall} = k_{eff} (\partial T / \partial n)_{wick}$. At the outer wall of heat pipe, the evaporator section was uniformly heated and the condenser section was cooled by heat sink with fan. Then,

the boundary condition at the outer wall in the evaporator, the adiabatic, and the condenser section can be given by $q_{in} = k_s (\partial T / \partial n)_{wall}$, $(\partial T / \partial n)_{wall} = 0$ and $q_{out} = k_s (\partial T / \partial n)_{wall}$, respectively.

3. The numerical procedure

The numerical procedure is illustrated in (Figure 2). The conservation equations and conditions were solved using the FEM, while matrices were derived from these equations using the Galerkin approach. The overall numerical procedure for the investigated problem is:

1. Specify geometric dimensions, thermo-physical properties, initial conditions, and boundary conditions in the interfaces.
2. The simulation program generated the grids.
3. The pressure and the velocity distributions in the vapor core were then calculated from the equation of continuity and the momentum equations.

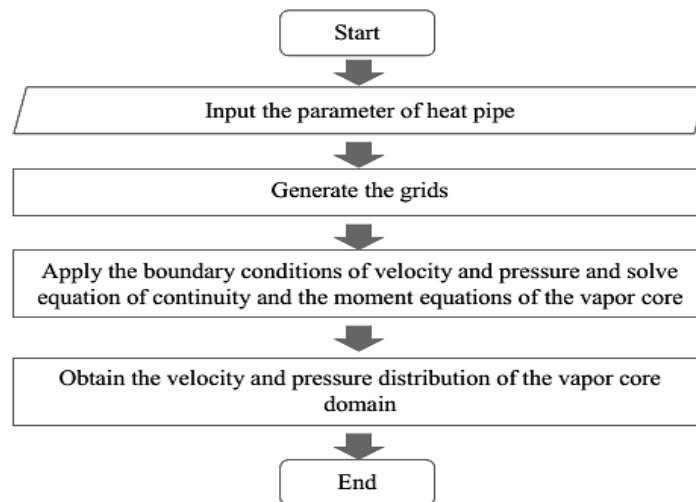


Figure 2 Schematic diagram of the numerical procedure

Results and Discussion

1. Effect of power input patterns on velocity

The effect of power input pattern is obtained by setting two different heater inputs at different positions. Vapor velocity profile in vapor core of three different power input patterns, i.e., 10W:10W, 20W:10W, and 30W:10W, (Heater 2 is fixed at 10W) is shown in (Figure 3). The vapor velocity was zero at the end of the heat pipe before entering the evaporator section. And the vapor velocity was increased through the first evaporator section. Vapor velocity was constant at the adiabatic section. The speed was increased again when entering the second evaporator section until it reached the end of this evapo-

rator section and the highest vapor velocity was found in this position. After that, vapor velocity was maintained along the adiabatic section. Then, vapor flows to the condenser section resulting in vapor velocity being reduced to zero at the end of the heat pipe, because of the lower temperature of the condenser section. Finally, working fluid was condensed to liquid phase.

The differences of vapor velocity in three cases, i.e., 10W:10W, 20W:10W and 30W:10W. It was note that, when power input of heater 1 was increased from 10W to 30W, the vapor velocity increased from 21.93 to 44.24 m/s at the end of the second evaporator section due to the mass transfer of vapor was the highest.

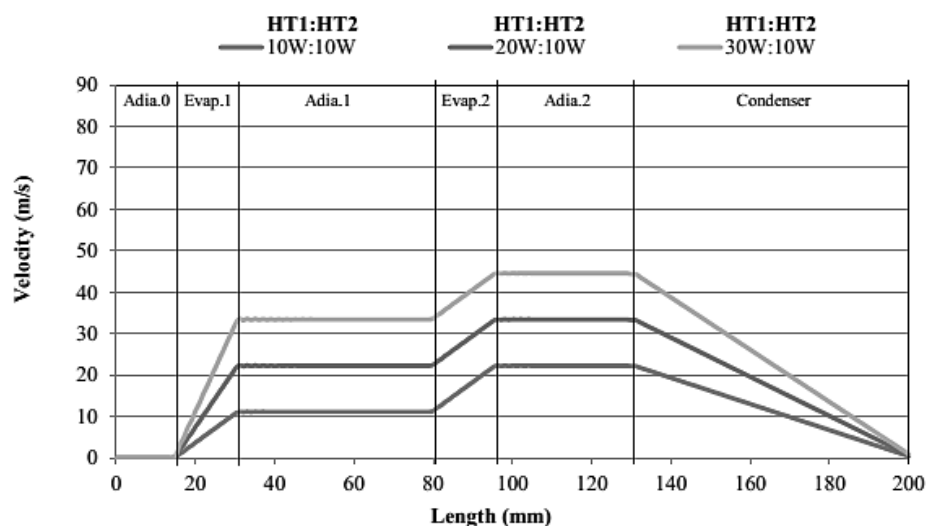


Figure 3 Longitudinal velocity profiles at different power input patterns (distance between heaters=50 mm, final thickness=3 mm)

2. Effect of pipe flattening on vapor velocity

(Figure 4) shows the vapor velocity profile along the length of the heat pipe. The velocity profile was shown in three different final thickness, i.e., 4, 3 and 2.5 mm. Power input of each heater was set at 20W. Distance between heaters is 50 mm. The longitudinal vapor velocity of 2.5 mm final thickness was the highest velocity as shown in (Figure 4) It was noted that the velocity would gradually increase from the end of both heaters. The vapor velocity was both constant at the adiabatic section

and gradually decreased from beginning to the end of condenser section. The maximum vapor velocity along heat pipe length was found at center vapor core of the flattened heat pipe. The maximum vapor velocity of the flattened heat pipe. The maximum vapor velocity of the final thickness of 4, 3 and 2.5 mm were found to be equal to 30.16 m/s, 43.87 m/s, and 75.91 m/s, respectively. It was observed that the maximum vapor velocity within vapor core at final thickness of 2.5 mm due to the cross section area of vapor core was smaller.

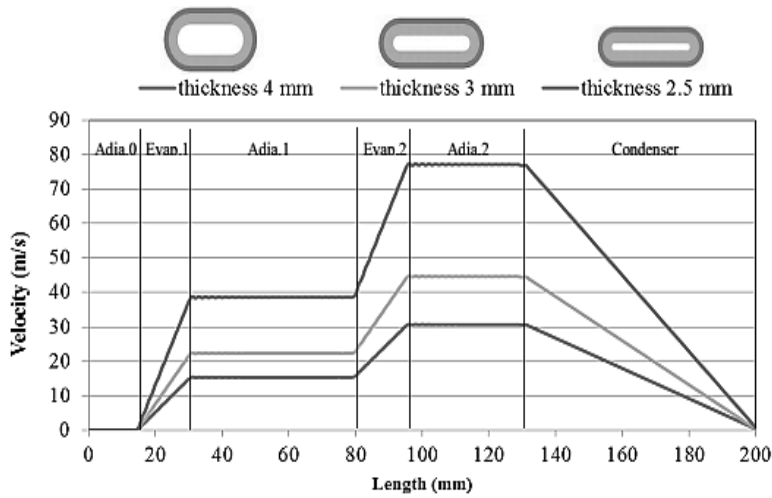


Figure 4 Longitudinal velocity profiles at vapor core of flattened heat pipe (power input each of heater=20 W, distance between heaters=50 mm)

3. Effect of distance between two heaters on velocity

(Figure 5) shows the vapor velocity at longitudinal position of different distance between heaters. The vapor velocity profile was shown in four different distances between two heaters, i.e., 0, 25, 50 and 75 mm. Power input of each heater was set at 20 W. It was found that, when first evaporator section overlapped with second

evaporator section (distance 0 mm), the vapor velocity increases to 42.43 m/s due to the heat accumulated from both heat sources. When distance between two heater increased from 0 to 75 mm. Maximum speed within the vapor core at about 44.43 m / s due to the amount of power supplied to the constant. As a result, the highest vapor velocity of each case was also approximately 44 m/s at the center of a vapor core.

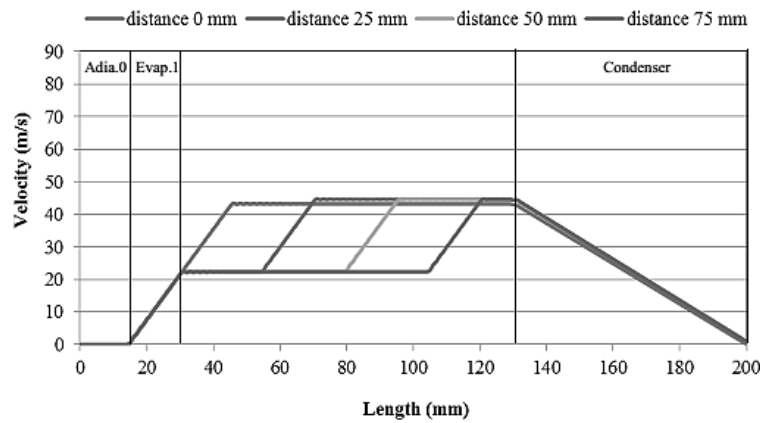


Figure 5 Vapor velocity profiles at various distances between two heaters (power input each of heater=20 W, final thickness=3 mm)

4. Comparison of Present Model Results

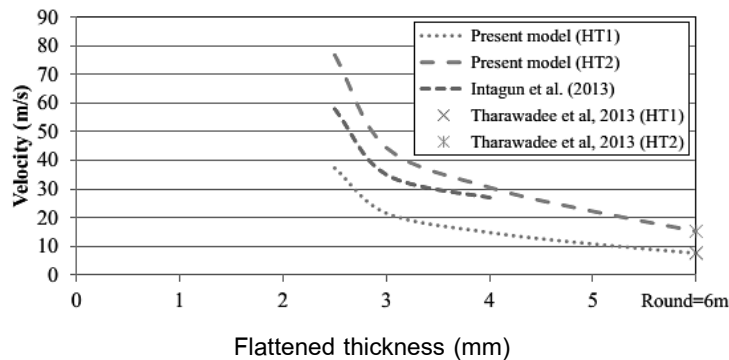


Figure 6 Vapor velocity profiles at various distances between two heaters (power input each of heater=20 W, distance between heaters=50 mm)

From (Figure 6), the x-axis is the flattened thickness and the y-axis is the velocity. Power input of each heater was set at 20 W. Distance between heaters is 50 mm. It was noted that, when the flattened thickness was increased from 2.5 mm to 6 mm, the velocity was decreased due to when the cross-section area of heat pipe was increased, heat load easily transferred to the condenser section because of the larger size of vapor core. The trend of velocity profile from this present model agreed with Tharawadee *et al.*⁷ and Intagun *et al.*³

Conclusion

The conclusions of this research are as follows.

- The mathematical model using the Finite Element Method to predict velocity have been established.

- Power input of heater 1 increases had been increased from 0 to 30 W; the vapor velocity increased from 21.93 to 44.24 m/s at the end of the second evaporator section.
- When heat pipe was flattened to the smaller final thickness, the cross sectional area of vapor core was reduced resulting in the highest vapor velocity along heat pipe length. The highest vapor velocity of the final thickness of 2.5 mm were approximately 75.91 m/s, which it was higher than final thickness of 4 and 3 mm.
- When the distance between heaters increases from 0 to 75 mm, the vapor velocity will slightly increases was approximately 44 m/s at the end of the second evaporator section.

The trend of vapor velocity from this mathematical model agreed with Tharawadee et al,⁷.

Acknowledgement

This work was supported by the heat pipe and heat systems laboratory, Faculty of Mechanical Engineering Chiang Mai University and Graduate school, Chiang Mai University. Thailand

References

- [1] Faghri, A., Heat Pipe Science and Technology, 1st ed., Taylor & Francis, Washington, DC, 1995.
- [2] Hirofumi Aoki, Masami Ikeda and Yuichi Kimura., 2011, "Ultra Thin Heat Pipe and its Application" 10th IHPS, Taipei, Taiwan, pp. 35-40.
- [3] Intagun, W., Terdtoon, P, and Sakulchangsattajai, P. (2013). Flattening effect on heat transfer characteristics of a sintered-wick heat pipe, American Journal of Applied Sciences 2013; 10(7): 760-766.
- [4] P.D. Dunn, and D.A. Reay, Heat Pipes, 4th ed., Pergamon, New York, 1994, 120-250.
- [5] M.M. Chen, and A. Faghri, "An Analysis of the Vapor Flow and the Heat Conduction through the Liquid-Wick and Pipe Wall in a Heat Pipe with Single or Multiple Heat Source," Int'l Journal of Heat Mass Transfer, 1990; 33(9): 1945-1955.
- [6] A. Faghri, and M. Buchko, "Experimental and Numerical Analysis of Low-Temperature Heat Pipes with Multiple Heat Sources," Journal of Heat Transfer, 1991; 113: 728-734.
- [7] Tharawadee, N., Terdtoon, P. and Kammuang-lue, N. (2013). An investigation of thermal characteristics of a sintered-wick heat pipe with double heat sources, American Journal of Applied Sciences 2013; 10(9): 1077-1086.

Snubber Circuit Used as the Temperature Dissipation of Mosfet for Electric Car Drive System

Sakrawee Reweekul¹

Received: 29 June 2015; Accepted: 13 July 2015

Abstract

This article presents a method to reduce the temperature of a mosfet by using a snubber circuit as the electric current dissipation of the switching current for motor speed control. The switching current during $t_{on\ state}$, and $t_{off\ state}$ of the mosfet can cause high power dissipation. This can damage the mosfet. In addition, in the $t_{off\ state}$ the mosfet is not conducted, there are some voltages across the mosfet that also can damage it when the voltage exceeds the mosfet voltage rating. This research therefore aims to study how to reduce temperature of the mosfet for an electric car drive system that employs paralleled mosfet in order to control motor speed continuously under a heavy load.

Keywords: snubber circuit, mosfet, parallel connected, electric drive, chopper, power dissipation.

Introduction

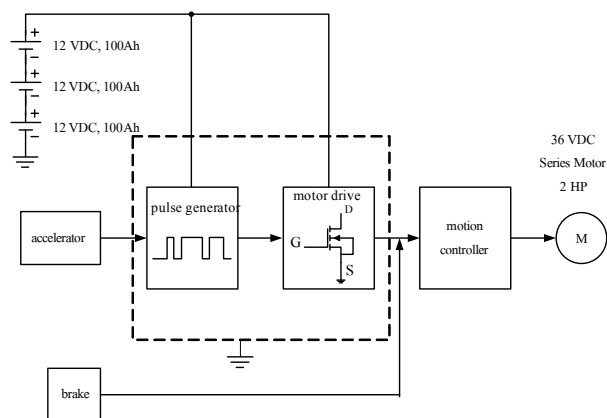


Figure 1 Block diagram of Electric car drive system

To control the speed of a direct current motor, there are many methods¹⁻³ for example by adjusting the value of a large current capacity resistor. This method is durable and needs fewer devices; This method requires high current capacity power electronic switch which can resist the instantaneous current during the switching times. The often used power electronic switches at present are mosfet and IPM. At present, the IPM is a module that is mostly used in the electric car drive system;

however, the drive circuit is expensive as well as the module itself.

Consequently, this research is to present an 8 – paralleled mosfet electronic switch used as the drive circuit which is inexpensive and durable.

However, a major problem of the paralleled mosfet is the limitation of the current tolerant. To carry the load current for a long time by each mosfet switch alone can damage the whole drive system and cause overheat, or burst^{4,5}.

This research is to study how to dissipate current for reducing temperature of the mosfet at the switches current during $t_{on\ state}$ and $t_{off\ state}$. By using a snubber circuit for a motor drive system employing paralleled mosfet for the speed control³. For the motor however, the high power loss is its disadvantage. Another method commonly used is to employ power electronic equipments as depicted in (Figure 1) drive system is inexpensive, requires less maintenance, and can be operated continuously when using a 2HP 36 VDC motor⁶. This article is divided into 4 parts, 1. Analysis of the drive system, 2. Design of snubber circuit, 3. Experiment, and 4. Conclusion.

¹ Rajamangala University of Technology Isan (Khon Kaen Campus), Department of Electrical Engineering, 150 Srichan Road, Muang District, Khon Kaen, 40000, Thailand *corresponding author: Email: mr_sakrawee@yahoo.com

Drive system

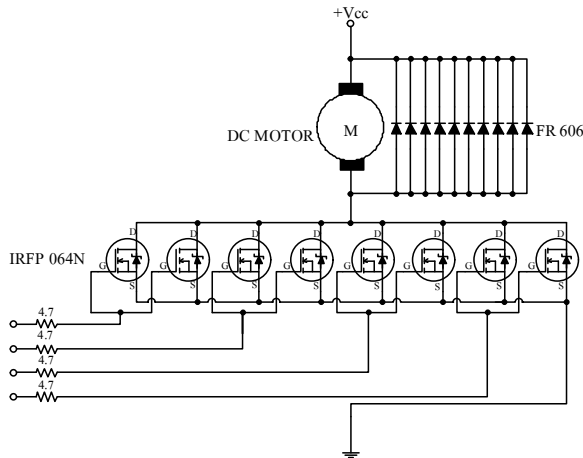


Figure 2 Switching mosfet switches

A switching power electronic circuit used as the direct current motor speed control is depicted in (Figure 2). The 8 mosfet switches are paralleled to control the electric car speed.

However, the driving system has a major problem at the high load at $t_{on\ state}$ and $t_{off\ state}$. While the mosfet conducts current as depicted in (Figure 3), a large current flowing through the mosfet can cause damage due to the overheating. At the off state, a large amount of voltage is across mosfet, if the voltage across the mosfet is for too long a time, damage due to the overheat can occur. Especially, for the paralleled case, each switch has a limitation of current tolerant; so, damage in one switch that can affect the whole drive system.

Snubber Circuit Design

Due to the problem mentioned above, the research aims to study and design a snubber circuit that is tolerant to over current or over voltage, and when there is the instantaneous change in both amplitude and rate of change. The designed snubber circuit has been divided into 2 sections: the over current protection and the over voltage protection. The details of each section are as follows;

The over voltage protection (turn-off snubbers) is depicted in (Figure 4). To protect the circuit from the instantaneous voltage, a resistor is series with a capacitor and then paralleled with the mosfet which is called a snubber circuit. The resistor and capacitor parameters can be calculated by

$$\text{capacitor } C_{S1} = \frac{I_o t_{fi}}{2V_d}, \text{ resistor } R_S < \frac{t_{onstate}}{2.3C_S}$$

where

- C_{S1} Snubber Circuit Capacitor
- I_o Motor current at starting of a 200 kilograms load, 60 A
- $t_{fi} \approx t_{ri} t_{off\ state}$ of the mosfet which is around the starting time
- V_d Motor rated voltage 36 volt
- R_S Snubber circuit resistance
- $t_{onstate}$ Current conducting period
- 2.3 Time interval the capacitor can totally discharge

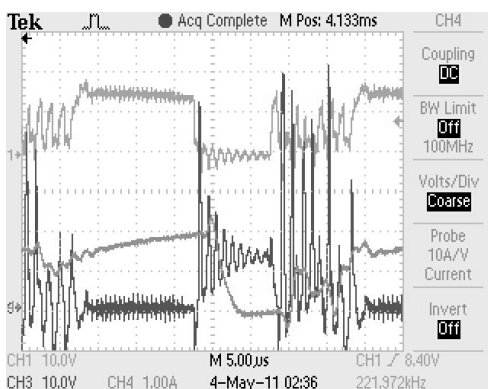
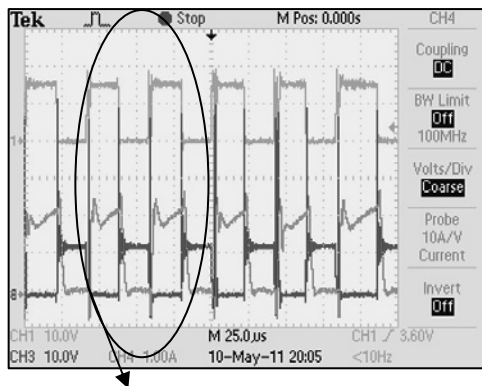


Figure 3 Voltage and current signals of Vgs, Vds, and Id from the experiment

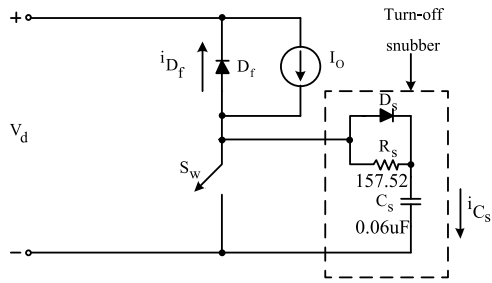


Figure 4 Over voltage protection circuit

However, a diode should be connected parallel with the resistor for the recovery time of the snubber circuit.

Under the surge voltage, the diode will conduct the current to pass through the capacitor. The capacitor will then behave like it is operating under the short circuit, which help reduce the voltage in the snubber circuit by allowing the voltage to be over itself. Under a normal operation when the capacitor is charged, the current will pass through the mosfet. When the capacitor is fully charged, the current will stop passing through the capacitor but it will flow through the whole circuit,

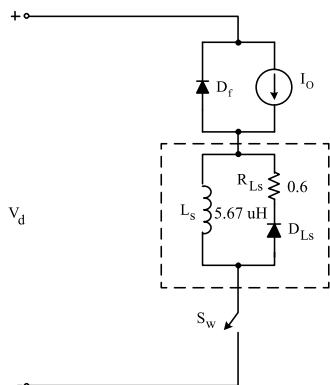


Figure 5 Over current protection circuit

the diode, and the resistor. The resistor helps reduce the current oscillation and limits the current under the current conducting period. However, at initial the capacitor will discharge the current into the circuit and the diode will help reduce the instantaneous current at the recovery.

To design the over current protection circuit (Turn-On Snubbers), the initial current (di/dt) is high and greatly damages the circuit system, therefore, as depicted in (Figure 5), an inductance (L_s) is serried with

a drain gate to reduce the rate of current. The energy is stored in the inductance and then will be transformed into heat. The inductance value can be calculated by

$$\text{resistor } R_{LS} = \frac{V_d}{I_o}, \text{ inductor } L_S < \frac{t_{\text{offstate}}}{2.3} R_{LS}$$

where

L_S Snubber Circuit Inductance

t_{offstate} Current conducting period

$t_{\text{fi}} \approx t_{\text{ri}}$ $t_{\text{off state}}$ of the mosfet which is around the starting time

R_{LS} Snubber Circuit Resistance

V_d Motor rated voltage 36 volt

I_o Motor current at starting of a 200 kilograms load, 60 A

2.3 Time interval the capacitor can totally discharge

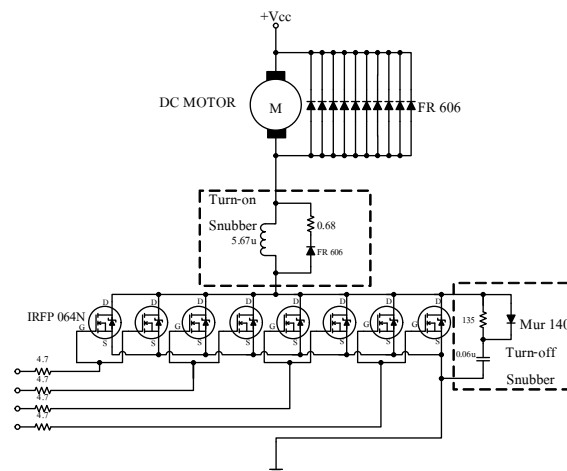


Figure 6 The equivalent circuit of the system

As you can see the depicted in (Figure 6) above, using snubber circuit can dissipate the over current in over shoot during during $t_{\text{on state}}$ and in under shoot during $t_{\text{off state}}$ for reducing temperature of the mosfet.

Materials and Methods

The experiment is conducted by connecting a snubber circuit with a motor speed control circuit of an 2 HP electric car rated (Figure 6) and (Figure 7) The duty cycle of a square wave pulse generating circuit can be adjusted through the 10kW resistor. The output pulse of the circuit then will be

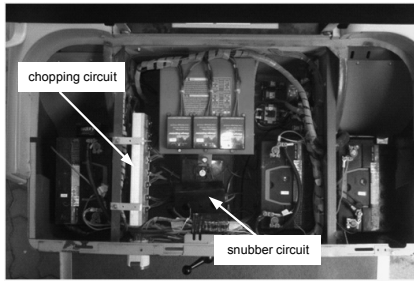


Figure 7 The electric car drive system of 2 HP 36 VDC rated

amplified and used to control the switching circuit; therefore, the motor voltage is able to change and vary according to the duty cycle of the square wave pulse generating circuit.

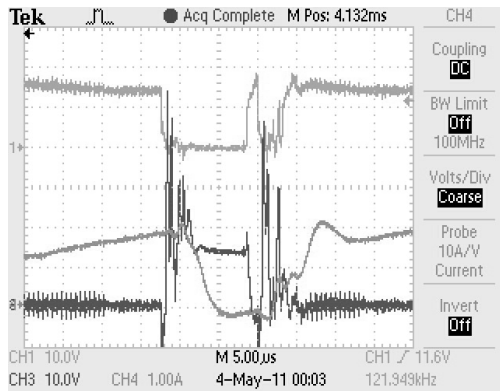


Figure 8 Signals of Vgs, Vds, and Id after connecting Turn on, Turn off Snubber circuits.

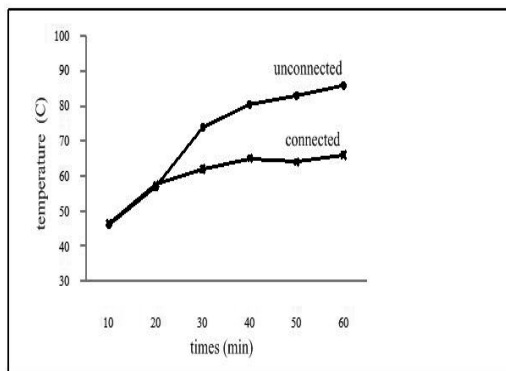


Figure 9 Comparison of temperature (heat) on the mosfet

The experiment results of adjusting the duty cycle of motor are depicted in (Figure 8) and the comparison of heat stored in the mosfet is depicted in (Figure 9).

Conclusion

From the experiment of the system after connecting the designed circuit, Turn On Snubber and Turn Off Snubber Circuits were observed for the Vgs and Vds of the mosfet under various duty cycles. The result of the experiment shows that whether the designed circuits are connected the overlapping of the voltages is low. However, the signals Vgs, Vds, and Id perform better responses when the designed circuit is connected, especially the Id that is decreased apparently, which helps reduce loss in mosfet while conducting the current. Besides, the voltage Vp that is able to damage the mosfet can also be reduced. Consequently, it can be concluded that to yield the best efficiency of the switching circuit, both of the snubber circuits should be connected.

Acknowledgement

Following the research was funded from Rajamangala University of Technology Isan, (RMUTI) Khon Kaen Campus. The purposes of the project are promotion and sustainable development in the industrial sector of Thailand and effective results. I would like to express my sincere appreciation for my co-researcher and my assistant researcher for contributing enormous intellectual and emotional support which led to the project’s success. Moreover, I would also like to express my gratitude to Electrical Engineering of the Faculty of Engineering for ure of their equipment and instruments.

References

- [1] C.W. Lander. *Power Electronic*.McGraw – Hill, England,3rd edn, 1997.
- [2] Rahim,N.A, Operating of Single-Phase Induction Motor as Two-Phase Motor, *IEEE Trans. On Industry Applications*, 2002; 38(6) 1566–1571.
- [3] Correa, M.B.R. Jacobina, C.B. Lima, A.M.N. and da Silva.E.R.C. Single-phase induction motor Drives systems, *IEEE Applied Power Electronics, Conference and Exposition(APEC '99.)*,Vol. 1, 1999, 403 – 409.
- [4] B.W. Williams. *Power Electronic*, The Macmillan Press,England 2nd edn, 1992.
- [5] M.H. Rashid. *Power Electronics : Circuits, Devices and Applications*. Prentice-Hall, USA,2nd edn,1993.
- [6] Krishnan,R. *Electric Motor Drives Modeling, Analysis and Control*, Prentice Hall, 2001.

Design and Development of a Small 3D Scanner

Sivapong Phetsong¹

Received: 30 June 2015; Accepted: 13 July 2015

Abstract

This research designed a simple 3D Scanner. The machines dimensions are 500x500x500 millimeters. The scanning area is 50x50x50 millimeters. The system has been integrated with C# language to create interface software, microcontroller for control stepping motor, webcam camera for capture reflection from laser, math algorithm to calculate coordinate between several types of coordinate and also integrate with image processing algorithm. In the experiments, we use laser shoot directly to object and take a picture of the reflection. We can then calculate the distance and point on surface. The machine take about 3 minutes to complete the scanning process. We also use the mesh formation software to create point cloud from data that we collect. And we also let that software to reconstruct point cloud to model surfaces. The result show that 3D Scanner has 1 millimeter accuracy with 4.6% error.

Keywords: 3D Scanner, Stepping motor, Laser, Microcontroller, Point Cloud

Introduction

The reverse engineering technique in the present day uses several techniques to reconstruct a 3D model in a computer. It used several techniques to make a copy of the original model, but the most relied on image processing. A vary famous technique uses laser to measure the distance from point to point in the two local coordinate systems. With these steps, the reconstruction process of the model becomes very fast and easy. The three famous techniques used in a 3D Scanner are Laser Scan, photogrammetric and the combined technique of Laser Scan and photogrammetric¹⁻⁶. The machine places a laser line on the object and uses a webcam to capture the laser line caused by the reflection on the object surface. The laser line displacement from the reference line will be measured by pixel count from photo^{1,3-7}. This distance will reflect the distance from the axis in a polar coordinate. When software collects enough surface points from the calculation, it can create surface related to these point clouds. Finally, the system can reconstruct the 3D model in the computer. The user can use these 3D models to modify the original model or even pass it to other software.

By the way, the quality of the model also relied on laser and camera quality.

Background and Fundamentals

1. Image Processing

There are two type of picture files in the computer, vectors or raster. Vector image contain pixel position and surface information. With vector image, user can easily modify 3D model and also unlimited scale the image. Raster is always used with the photo because it collects every point in the pictures as a color pixel. When the system combines the individual pixel together, it becomes a photo. Each pixel can contain only one color level which the color level has been defined by file description, such as 8-bit or 24-bit color depth; the more color the more realistic. In the displaying process, Data in the files must be processed and applied to any image processing technique. First of all, Data will be changed to color at each pixel. Then it will be processed to improve the quality such as sharpen, smooth or noise removal. The technique required in the 3D scanner is to eliminate noise from picture and remove everything except the laser from

¹ Department of Mechanical Engineering, Faculty of Engineering and Industrial Technology, Silpakorn University Sanamchandra Campus, MuangNakornPatom, Thailand 73000 sivapong@su.ac.th, +6634 259025, +6634 219367

the pictures and convert to black color.

2. The Grey Scale

Grey Scale is one type of color depth. It contains several shades of color from white to black. It explains any pixel as a level of grey shade by white gradient. The user will notice the different color levels but grey scale uses less data than the color image. The color consist of three primary colors, Red, Green and Blue. Each primary can made 256 different shades. Converting the color image to grey scale, each pixel must be divided into three primary colors. Equation 1 is used to convert the color image to grey scale^{8,9}. With this equation, the image looks as smooth as in color. (Figure 1) shows the converting process.

$$grey = (blue \times 0.11) + (green \times 0.59) + (red \times 0.30) \quad (1)$$

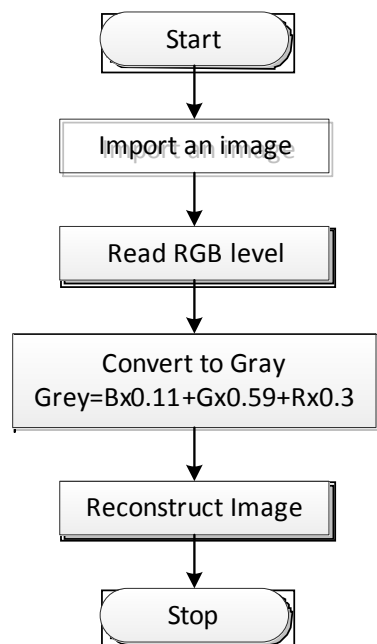


Figure 1 Converting color images to grey scale.

3. Assembly point to picture

The coordinates we have can be assembled together to make a small surface called a polygon. Polygon requires at least 3 points in space to create. A model with a lot of polygons can create a 3D model. The more polygon the more realistic the 3D-Model. This can be easy explained by curvature surface¹⁰⁻¹². If the curve has been divided in a few pieces, the polygons (or face), which are created by these points, are coarse. The

model will also be coarse. If this curve has been divided in a lot of piece, the polygons are small. The model will also be fine and realistic.

Materials and Methods

1. The distance estimation

The process to create the 3D-Model back from the object and pictures. In this research, we use the distance calculation technique from the reflection of light. At first, we spot the laser to the object and take a picture of the reflection. Without any object in the experiment, the reflection of the laser line will be the vertical line at the reference point in x-direction. When we put the object in the experiment, the reflection shifts from the reference point to the right. We can then count back the distance from the reference point in x-direction in the unit of pixels. It is the distance from reference point.

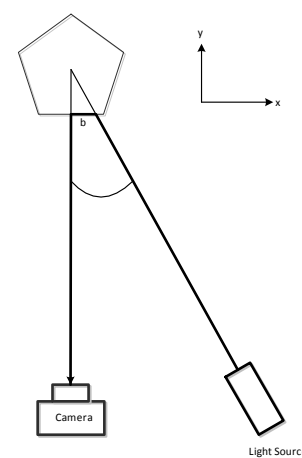


Figure 2 Position of camera, object and laser.

The structure of the machine fixed the angle between the axis of the camera and the direction of the laser line to alpha (a) as shown in (figure 2). The value of rho (r) is the thing we need. It is the real distance in the cylindrical coordinate but we cannot measure it directly. We can calculate the (b) distance from the picture. As we know the distance in pixels between the reference points to laser point in the picture we took. We can calculate the pixel distance to the distance of b in millimeters^{2,3,13-15}. With the assumption that the nonlinearity of distance to pixel is negligible. After that, apply Equation 2 to transform distance b to rho (r) which is the position in cylindrical coordinate.

$$\rho = \frac{b}{\sin(\alpha)} \tag{2}$$

Software will help us to calculate distance of every laser point in the pictures to surface position. Then the object will be turned around in a small angle. The process will be started again and recalculated at every point again. This process happens until the object has made a 360 degree turn. Then the scanning process is complete. Then Software recalculate all point into the rectangular coordinate by using the equation 3.

$$\begin{aligned} x &= \rho \cos(\alpha) \\ y &= \rho \sin(\alpha) \\ z &= z \end{aligned} \tag{3}$$

2. Machine Development

The development of the 3D Scanner can be separated into three parts, Machine Structure and hardware, Controlling Software and the image processing software. These three parts work independently of each other but are integrated in the same software to centralize control for the user. The device has a rotat base that can be rotated in z-direction to follow the cylindrical coordinates. The object size is 50x50x50 millimeters maximum allowance. It can turn 0.8 degree in each step. In the experiments, we use the red laser line to specified location. The results show that the machine can make detail up to 1 millimeter. (Resolution will be better with finer laser line and better camera.)

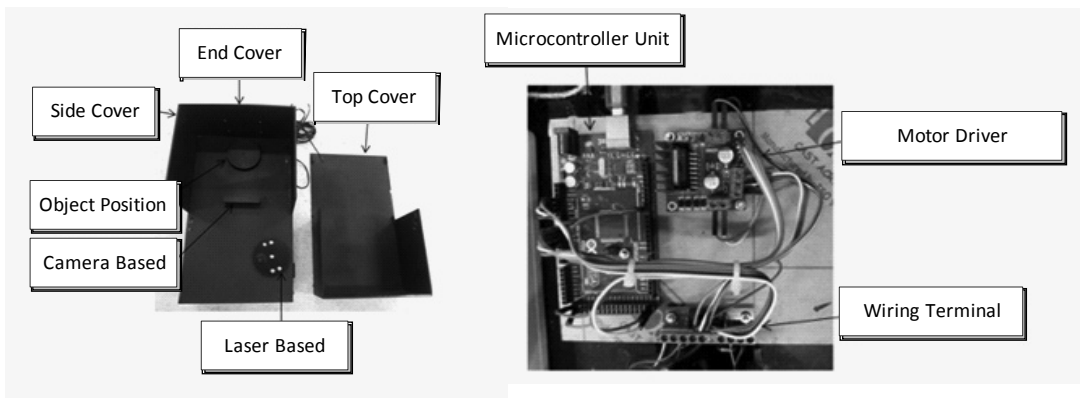


Figure 3 inside the scanner.

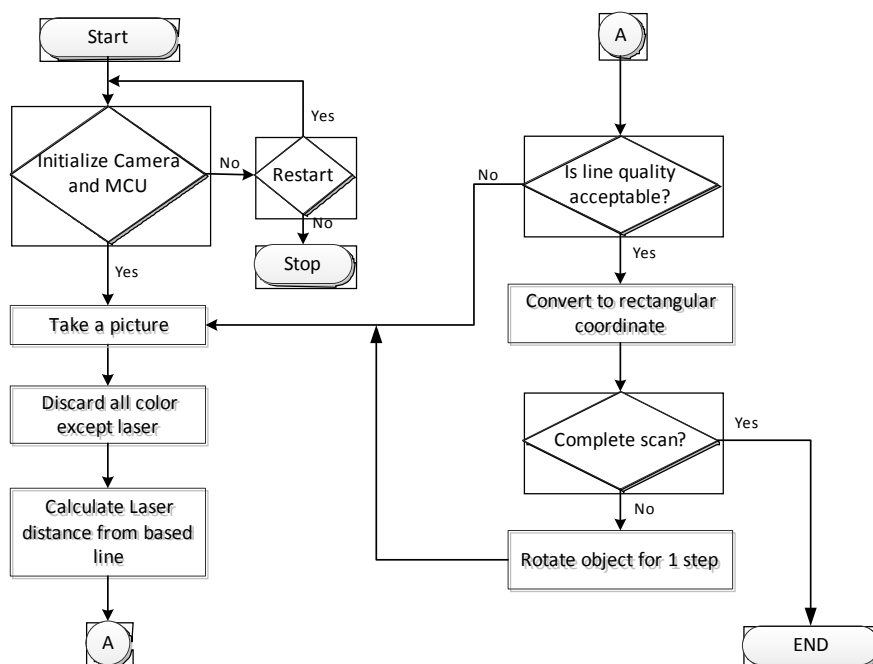


Figure 4 Flowchart of the Control software

The control software is used to control and interconnect the applications developed in C# with the software in microcontroller to control the camera, laser and the scanning machine. Software tries to connect to every device needed in the scanning process when it started. Then software get the picture from the camera and follows the process in the flowchart in (figure 4). The image processing technique has been applied at this point based on the laser color. Every color in the picture will be discarded except the laser color by using this image processing technique. At this point there is only one color left in the picture. Software will convert the picture to grey scale to reduce the processing time making it easy to analyze.

3. Calibration

Because of the differences of the picture makes from different camera model software has to be configured to make it suitable for the system. It requires user setting to the right color of the laser color. Then we have to make a reference point in the pictures and reference to the real position to make a reference for software calculation. These value are different in each camera because of the camera structure and camera lens^{16,17}. In addition, we have to adjust the laser position and direction including the laser color, according to (figure 5), so that the reference position of the laser does not distort the laser line has to be sharp. This will directly affect the accuracy of coordinates obtained from the calculation.



Figure 5 Software interface in color setting

Results

After the adjustment of the laser and camera. In the experiment with 360 degree angle with 0.8 degree per step, the machine take about 3 minutes to complete a scan. We try to plot the result coordinate and create polygon with point cloud software. The results show that

it is close to the original model. There are some errors in the result because of the relationship of the distance between pixels is proportional to the distance from the camera to the subject, which is not linear. When tested at various distances, we found a relationship of these two distance as in (figure 6).

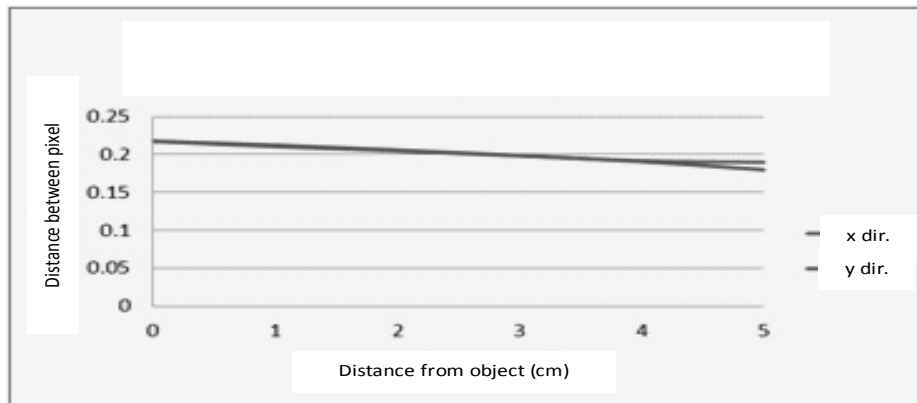


Figure 6 the variation of the distance between pixels at different stages.

The result from the simple object geometry scanning which we know dimension exactly. We founded that there is the slightly distorted due to the uncertainty

of the surface width per pixel. It was found that the maximum error of 9.42% on flat surface and the maximum error of 23% for hole size 1 mm.

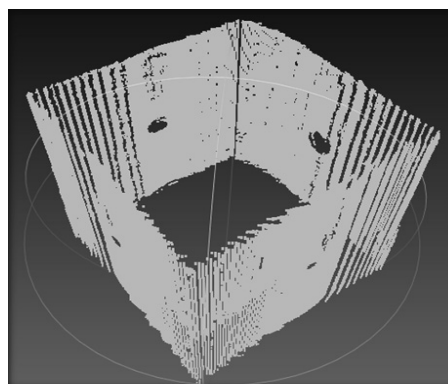
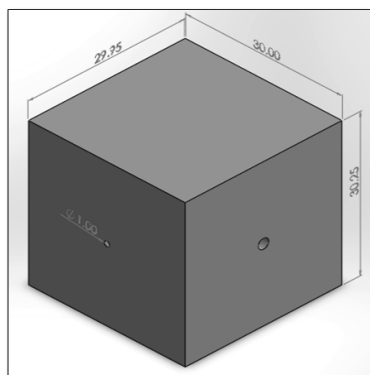


Figure 7 rectangular object. Compared with the scanned model.

When compensation at various stages with the value from the chart in (Figure 6). We founded that the model is more accurate. The error of the pyramid shape

model is about 6.8% in the wide side. The cone model has maximum error about 4.6%

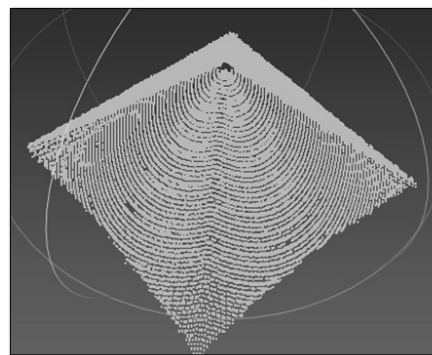
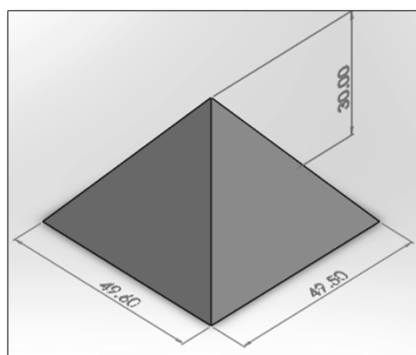


Figure 8: pyramid shaped object. Compared with the scanned model.

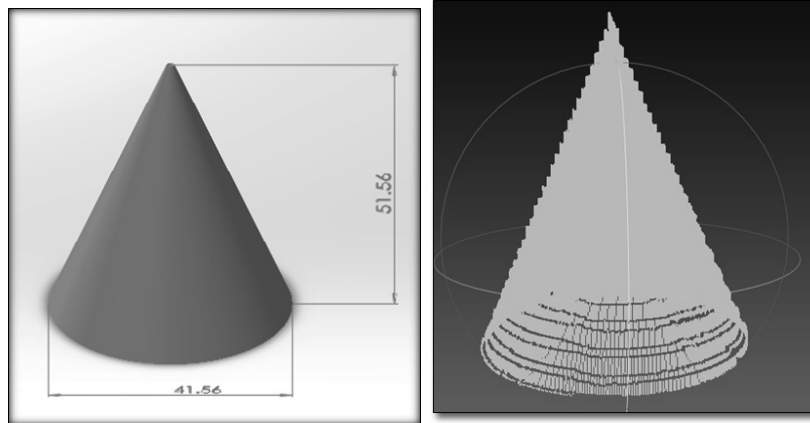


Figure 9 cone-shaped object. Compared with the scanned model.

In addition, the external light can interfere with the system and has a large effect on the laser reflection due to lower contrast. The laser line in the picture is much

more diffuse and leads to the more difficulty to calculate the exact coordinate. Scanning in the dark without any interference from ambient light will make the better result.



Figure 10 Ambient light affect the contrast

The result from the experiment with the freeform object show the better result. The 3D model created from the point cloud from the result make the better model.

The dimension is almost the same as the original model and also easy to modify in computer.

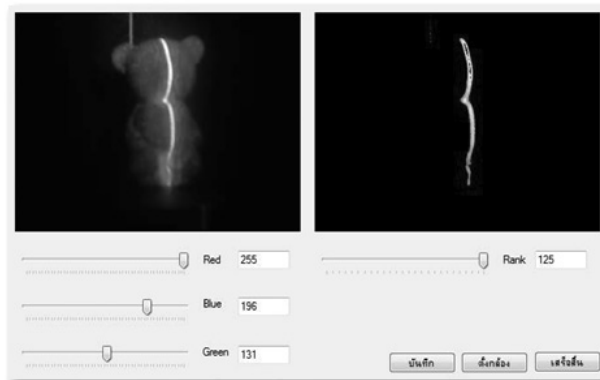


Figure 11 The suitable contrast allow easily calculated.

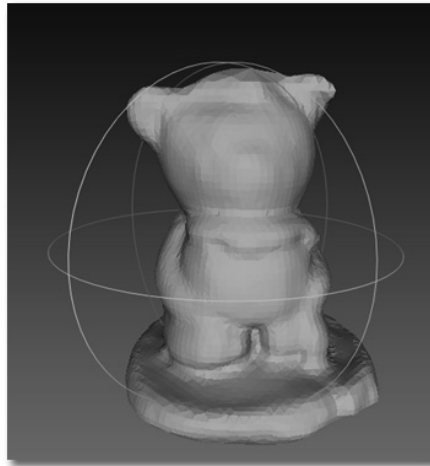


Figure 12 The 3D model prototypes from machine with error compensate.

Conclusion

The 3D scanner machine can reproduce the data and create a 3D model from real objects. The machine has a 1 millimeter accuracy due to the limitation of the device, laser and camera. The machine still has some problems with external light interference because of the type of camera. This problem can be solved by using other camera types such as infrared or implemented some image processing algorithm. The nonlinearity of camera picture and lens distortion still affect the result. When we neglect the nonlinearity, it lead to 9.42% result error in normal surface and as high as 23% in a very small surface. When integrate with nonlinearity, the result error reduce to 4.6%. In addition, the research did not consider the results of statistical data^{10,18-22}

“type” : “article-journal”,
 “volume” : “66” }, { “uris” : [“http://www.mendeley.com/documents/?uuid=700d3d45-4e51-4d88-85d7-ce75c-c65615e”] }, { “id” : “ITEM-3”, “itemData” : { “DOI” : “10.1016/j.optlaseng.2008.09.003”, “ISSN” : “01438166”, “author” : [{ “dropping-particle” : “”, “family” : “Shiou”, “given” : “Fang-Jung”, “non-dropping-particle” : “”, “parse-names” : false, “suffix” : “” }, { “dropping-particle” : “”, “family” : “Liu”, “given” : “Min-Xin”, “non-dropping-particle” : “”, “parse-names” : false, “suffix” : “” }], “container-title” : “Optics and Lasers in Engineering”, “id” : “ITEM-3”, “issue” : “1”, “issued” : { “date-parts” : [[“2009”, “1”]] }, “page” : “7-18”, “title” : “Development of a novel scattered triangulation laser probe with six linear charge-coupled devices (CCDs). If we change the direction of the laser to

the landscape as well as increase the number of lasers and scan each plane will coordinate overlapping. The result will be more accurate.

Reference

- [1] S. Al-kheder, Y. Al-shawabkeh, and N. Haala, Developing a documentation system for desert palaces in Jordan using 3D laser scanning and digital photogrammetry, *J Archaeological Science*, 2009; 36(2): 537-546.
- [2] J. Chen, X. Wu, M. Yu Wang, and X. Li, 3D shape modeling using a self-developed hand-held 3D laser scanner and an efficient HT-ICP point cloud registration algorithm, *Optic and Laser Technology*, 2013; 45: 414-423.
- [3] G. Fu, A. Menciassi, and P. Dario, Development of a low-cost active 3D triangulation laser scanner for indoor navigation of miniature mobile robots, *Robotics and Autonomous System*, 2012; 60: 1317-1326.
- [4] H. González-Jorge, B. Riveiro, P. Arias, and J. Armesto, Photogrammetry and laser scanner technology applied to length measurements in car testing laboratories, *Measurement*, 2012; 45(3): 354-363.
- [5] A. Pesci, M. Fabris, D. Conforti, F. Loddo, P. Baldi, and M. Anzidei, Integration of ground-based laser scanner and aerial digital photogrammetry for topographic modelling of Vesuvio volcano, *J. Volcanology and Geothermal Research*, 2007; 162, 3-4, 123-138.

- [6] C. Sahin, A. Alkis, B. Ergun, S. Kulur, F. Batuk, and A. Kilic, Producing 3D city model with the combined photogrammetric and laser scanner data in the example of TaksimCumhuriyet square, *Optics and Lasers in Engineering*, 2012; 50(12), 1844–1853, Dec.
- [7] A. V. Leonov, M. N. Anikushkin, A. V. Ivanov, S. V. Ovcharov, A. E. Bobkov, and Y. M. Baturin, Laser scanning and 3D modeling of the Shukhov hyperboloid tower in Moscow, *J. Cultural Heritage*, 2014; 16(4): 551-559.
- [8] T. Horiuchi, F. Nohara, and S. Tominaga, Accurate reversible color-to-gray mapping algorithm without distortion conditions, *Pattern Recognition Letters*, Vol. 2010; 31(15): 2405-2414.
- [9] M. Song, D. Tao, C. Chen, J. Bu, and Y. Yang, Color-to-gray based on chance of happening preservation, *Neurocomputing*, 2013; 119: 222-231.
- [10] M. Torabi, S. M. Mousavi G., and D. Younesian, A new methodology in fast and accurate matching of the 2D and 3D point clouds extracted by laser scanner systems, *Optical and Laser Technology*, 2015; 66, 28–34, 2015.
- [11] Y. Liu, Automatic registration of overlapping 3D point clouds using closest points, *Image and Vision Computing*, 2006; 24(7), 762–781.
- [12] B. He, Z. Lin, and Y. F. Li, An automatic registration algorithm for the scattered point clouds based on the curvature feature, *Optical and Laser Technology*, 2013; 46, 53–60.
- [13] V. V. Lehtola, J.-P. Virtanen, A. Kukko, H. Kaartinen, and H. Hyypä, Localization of mobile laser scanner using classical mechanics, *ISPRS J. Photogrammetry and Remote Sensing*, 2015; 99, 25–29.
- [14] V. Lombardo and T. Marzulli, A time-of-scan laser triangulation technique for distance measurements, *Optics and Lasers Engineering*, Vol. 2003; 39, 247–254.
- [15] A. L. Reyes, J. M. Cervantes, and N. C. Gutiérrez, Low Cost 3D Scanner by Means of a 1D Optical Distance Sensor, *Procedia Technology*, 2013; 7, 223–230.
- [16] A.-I. García-Moreno, D.-E. Hernández-García, J.-J. González-Barbosa, A. Ramírez-Pedraza, J. B. Hurtado-Ramos, and F.-J. Ornelas-Rodríguez, Error propagation and uncertainty analysis between 3D laser scanner and camera, *Robotics and Autonomous System*, 2014; 62(6) 782–793.
- [17] B. Muralikrishnan, W. Ren, D. Everett, E. Stanfield, and T. Doiron, Performance evaluation experiments on a laser spot triangulation probe, *Measurement*, 2012; 45(3) 333–343.
- [18] L. Zeng, F. Yuan, D. Song, and R. Zhang, A two-beam laser triangulation for measuring the position of a moving object, *Optics and Lasers Engineering*, 1999; 31, 445–453.
- [19] F.-J. Shiou and M.-X. Liu, Development of a novel scattered triangulation laser probe with six linear charge-coupled devices (CCDs), *Optics and Lasers Engineering*, 2009; 47(1): 7-15.
- [20] Ş. Ozan and Ş. Gümüştekin, Calibration of double stripe 3D laser scanner systems using planarity and orthogonality constraints, *Digital Signal Processing*, 2014; 24:231-243.
- [21] R.-T. Lee and F.-J. Shiou, Multi-beam laser probe for measuring position and orientation of freeform surface, *Measurement*, 2011; 44(1): 1-10.
- [22] F. J. Brosed, J. Santolaria, J. J. Aguilar, and D. Guilomía, Laser triangulation sensor and six axes anthropomorphic robot manipulator modelling for the measurement of complex geometry products, *Robotics and Computer Integrated Manufacturing*, 2012; 28(6): 660-671.

The Continuous Process of Biodiesel Production with Water Heater Assist

Thibordin Sansawang¹, Chanjira Chimmanee¹, Trakan Butsing¹

Received: 12 June 2015; Accepted: 13 July 2015

Abstract

The paper is to design a lab-scale biodiesel production machine with continuous process. This machine consists of a 25 liter - tank of used cooking oil and a 6.5 liters - tank of methanol. The used cooking oil and methanol flow to the reactor with the designed flow rate so that the complete reaction occurs at the end of the reactor. The production rate is 1.817 liter/hour for normal operation mode. Then, this machine is modified equipped with a hot water system. The temperature of hot water is set to 40, 50 and 60°C. The production rate is increased to 3.15, 3.24 and 3.37 liter/hour respectively. The properties of biodiesel are tested and found that there are according to the ASTM D6751.

Keyword: biodiesel, biodiesel production, use cooking oil, transesterification

Introduction

Since the internal combustion diesel engine was invented in the early 20th century by Rudolf Diesel. It used vegetable oil as fuel. Then, petroleum was discovered a few years later, and replaced vegetable oil due to its higher engine efficiency¹. Currently, diesel fuel has become an important factor in our modern life. Due to the latest oil crisis, most countries realize the importance of alternative fuel resources, especially in diesel engines. Vegetable oil contains fatty acid vary with the type of them. These fatty acid may cause the problems of combustion and emissions due to the worse physical and chemical properties than that of diesel. There are four techniques to modify the raw vegetable oil to use in diesel engine; pyrolysis, micro-emulsion, transesterification and blending¹⁻³. Transesterification is wide accepted to be the best method to modify the raw vegetable oil into biodiesel to be used in a compression ignition (CI) engine without modification.

The biodiesel production is the reaction between fatty acid and alcohol such as methanol and ethanol. Generally, batch production is used in the commercial scale⁴⁻⁷. The continuous process is study to produce more biodiesel at a time. The problem of continuous process

is time of reaction⁸⁻⁹. In this study, the lab-scale of biodiesel production is designed and test. The test experiment is performed at the ambient temperature and higher to compare the production yield and time of reaction.

Materials and Methods

1. Material and Transesterification

Transesterification is the reaction between fatty acid and alcohol. Fatty acid will change to ester as seen in (Figure 1).¹⁰

Biodiesel is a product of reaction of a triglyceride and alcohol to form ester (-O-C-O-), biodiesel and by product, glycerol as shown in (Figure 1). This reaction is reversible and the excess alcohol is used to force the equilibrium to the product side. The stoichiometric molar ratio of oil to methanol is 1:3.¹⁰ This can be converted into mass ratio is 10:1. In this experiments, the batch production done by the authors manually showed that the 10:2 is the best ratio. So this study uses 10:2 for all experiments.

Triglyceride are often found in natural fat from plants or animals^{11,12}. Therefore, used cooking oil was selected to use in this experiment because of it is the waste from food production.

¹ Department of Mechanical Engineering Faculty of Engineering and Industrial Technology Silpakorn University
E-mail: sangsawang_t@su.ac.th

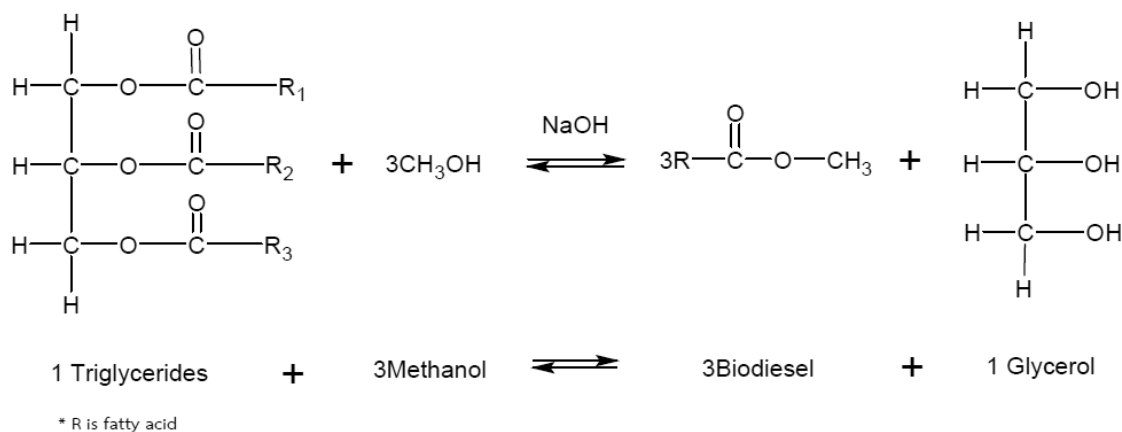


Figure 1 Transesterification[10]

2. Design and Experimental Procedure

The preliminary experiment begins with the batch production manually. Used cooking oil for 1.0 kg and 0.20 kg of methanol were mixed in the reactor tank. NaCl of 1% by mass of used cooking oil is used as catalyst. Firstly, there was no heat input to the reaction. The biodiesel from the reaction could be occurred at ambient temperature. Time of complete reaction in this case was 1 hour approximately.

Another experiment was batch production, but the heat from the heating coil was used to increase the temperature of used cooking oil. Temperature was controlled to be 40, 50 and 60°C. Time of complete reaction were found to be only 30 minute approximately for all cases.

Yield of biodiesel was a very important parameter. In manual batch production, the yield of biodiesel is up to 90%. This continuous process was expected for 1.5 litre/hour and yield was not less than 50%. So that the quantity of the used cooking oil tank was 25 liters for 7 hour operation for one sample. The methanol tank was 6.5 liters and NaCl was 1% of used cooking oil. The diagram of this machine is shown in the (Figure 2).

Time of reaction were used to design the flow rate of used cooking oil and methanol. Firstly, this

machine was not equipped with the hot water heater. So that the time of complete reaction would be 1 hour and then the mixture flowed to the separator tank continuously. The mixture stayed in the separate tank for 3 hours and flows continuously to the 1st cleaning tank. The hot water, 60°C, flowed from the hot water tank to wash the mixture in the 1st cleaning tank for 1 hour. The waste such as glycerin, moisture and catalyst were removed and the mixture flowed to the 2nd cleaning tank. The cleaning process was repeated so that biodiesel was purified.

Afterward, the water heater was equipped at the reactor to increase the reaction rate. The both flow rate of used cooking oil and methanol were adjust by "trial and error" with the information from the preliminary test by manual batch production. The data of time of reaction were repeated for at least 3 times and collected as the results of this investigation.

(Figure 3) shows the lab-scale biodiesel production machine. The fuel and methanol tank are placed on the top of the machine. Gravity and flow control valve are used to control the flow rate of both raw materials. The result from the preliminary test are used to control the rate of reaction. The experiment results are analyzed by the test of hypothesis.

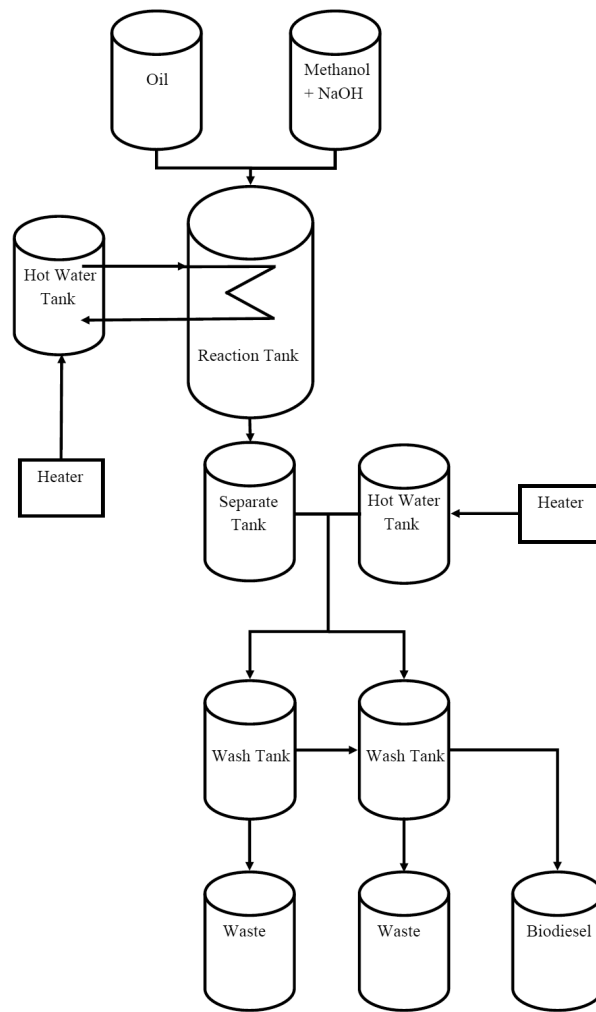


Figure 2 Diagram of Biodiesel Production Process

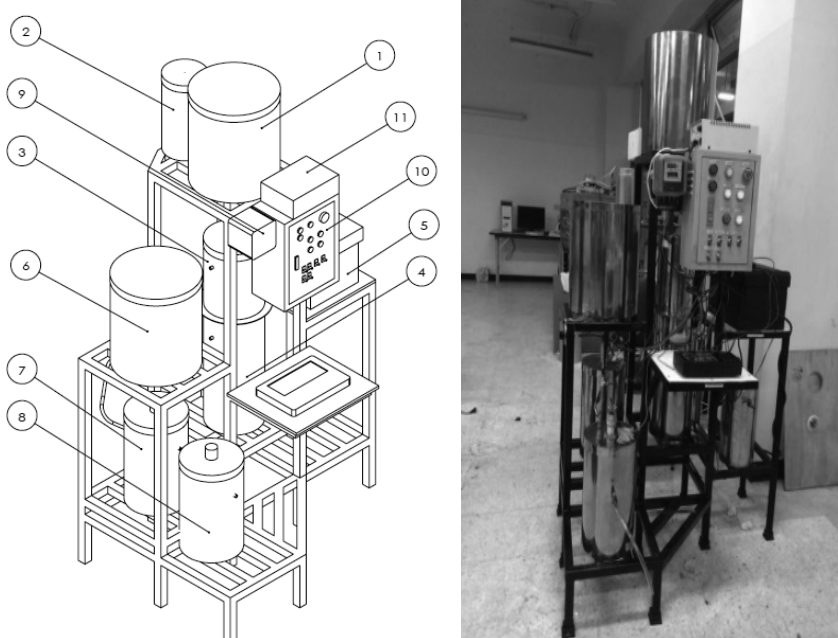


Figure 3 Biodiesel production machine 1. Oil tank, 2. Methanol tank, 3. Reactor, 4. Separator, 5. Hot water tank, 6. 1st cleaning tank, 7. 2nd cleaning tank, 8. Biodiesel reservoir, 9. kW-hr meter, 10. Control box, 11. Inverter

Results and Discussion

(Table 1) shows the time in each station of the biodiesel production machine. The ambient temperature mode uses the time to complete the reaction within 54

minutes. The higher temperature presents the shorter reaction time. The experiments shows that the temperature of 40°C to 60°C reduces the reaction time to 30 minute approximately

Table 1 Experiments result

time	temperature				unit
	Ambient temp.	40°C	50°C	60°C	
Reaction tank	54	32	32	31	minute
Separation tank	293	227	221	212	minute
1 st cleaning tank	54	53	53	51	minute
2 nd cleaning tank	59	58	57	55	minute
Total time of production	642	462	452	428	minute
Production rate	1.817	3.15	3.24	3.37	liter/hour
% yield	73.18	82.4	86	88.8	%

The separation time is shorter for the higher temperature mode due to the lower viscosity of oil. The lower viscosity leads to the higher rate to reaction with methanol. The separation times are reduced from 293 minute to about 220 minute. The time of cleaning process

are not significantly different. The total production time of the water heater mode is reduced for 30% approximately. The shortest production time is 428 minutes for the temperature of 60°C of hot water.

Table 2 Statistical Analysis by Test of Hypothesis

Temperature	Production rate			% yield		
	t	v	P-value	t	v	P-value
40°C	20.00	2.87	0.0017	4.69	2.23	0.023
50°C	22.13	2.58	0.001	6.66	2.06	0.012
60°C	21.25	3.56	0.0005	7.15	3.12	0.0038

The hypothesis of this experiments in (Table 2) is set as follows; H_0 the temperature effect to the production rate and yield. H_1 ; the temperature does not effect to the production rate and yield. According to the table of Navidi¹³, the t and v value in the Table 2 shows

that P-value is under 0.05. At least 3 sample in each experiment were collected. It is found that H_0 is accepted. That means the higher temperature contributes the higher production rate and yield.

Table 3 Biodiesel specification

No.	Item	unit	Standard	Production temperature				Method
				Ambient	40°C	50°C	60°C	
1	Density at15°C	kg/m ³	0.86 - 0.90	0.885	0.881	0.881	0.881	ASTM D 4052-11
2	Viscosity at 40°C	cSt	3.5 – 5.0	5.612	5.0	4.8	4.7	ASTM D 445-12
3	Flash Point	°C	> 120	> 120	> 120	> 120	> 120	ASTM D 93-11
4	Cu Corrosion	-	No.1	1a	1a	1a	1a	ASTM D 130-10
5	Acid	mg KOH/g	< 0.50	0.36	0.177	0.168	0.147	ASTM D 664-09
6	Heating Value	kJ/kg	-	39,444	39,634	39,687	39,701	ASTM D 240-02

(Table 3) present the properties of biodiesel from the biodiesel production machine. All item are agreed with the ASTM standard. However, the viscosity of biodiesel from the ambient mode is out of range for 10%.

Table 4 Cost of Production

Item	Production Temperature				Unit
	Ambient	40°C	50°C	60°C	
Used Cooking Oil	25	25	25	25	Liter
Methanol	6.41	6	6.03	6.08	Liter
NaCl	208.2	110	110	110	gram
Electricity Consumption	1.33	3.33	3.43	3.37	Unit
Total Cost	466.33	566.45	567.47	568.51	Baht
Product	18.87	20.6	21.5	22.2	liter
Production Cost	30.74	27.49	26.39	25.61	Baht/liter

(Table 4) shows the details of biodiesel production. The higher temperature increases the production rate and lower energy consumption. The lowest cost is 25.61 Baht/liter at 60°C of reaction tank. The highest cost is 30.74 Baht/liter for ambient temperature of the reaction. The table shows that the highest cost is from the raw materials. In this experiments, electric oil is used to heat up the water in the reactor tank. Cost of electricity are about 25% of total cost. The electricity of production could be reduced from another method which are not mentioned here.

Conclusion

The transesterification of used cooking oil yield biodiesel is an effective way to reduce the waste from

food production and pollution. The major drawback is the production cost. The one way to reduce process cost is change from batch production to continuous production. This study is to built the continuous process of biodiesel production machine in lab-scale. The water heater is equipped to increase the production rate. The experiments show that the production rate is increased for 73.36, 78.32 and 85.47% for the hot water temperature of 40, 50 and 60°C respectively. The production cost is reduced up to 16.69%. The properties of biodiesel are meet the requirement of ASTM 6751.

The next step of this investigation is to reduce the production cost by using a solar water heater. This could lower the energy usage and reduce the production cost.

Acknowledgement

The authors would like to thank the Department of Mechanical Engineering, Faculty of Engineering and Industrial Technology, Silpakorn University for their financial support.

References

- [1] Agarwal, A.K., *Biofuels (Alcohols and Biodiesel) Applications as fuels for Internal Combustion Engines*, *Progress in Energy and Combustion Science*, 2007; 33, 233 – 271.
- [2] Ma, F. and Hanna, M., *Biodiesel Production: a Review*, *Bioresource Technology*, 1999; 70: 1-15.
- [3] Fukuda, H., Kondo A. and Noda, H., *Biodiesel Fuel Production by Transesterification of Oils*, *Journal of Bioscience and Bioengineering*, 2001; 92(5): 405-416.
- [4] Jantaban, N. and Supapu, N., *Design and Built Biodiesel Production Equipment from Used Cooking Oil*. Bachelor Project, Department of Mechanical Engineering, Faculty of Engineering, Khonkan University. 2549.
- [5] Sukhrom, S., *Study and Design of Lab-Scale Biodiesel Production*, Department of Engine, Lampang Technical College, 2556.
- [6] Surampai S., *Biodiesel Production with Combine Energy*, Clinic Technology, Ubolrachathani Technical College, 2554.
- [7] Buaphumi, W., Tapa, S. and Sudprasert K., *Biodiesel Production with Solar Assist*, Energy Technology Division, School of Energy, Environment and Material. King Mongkut's University of Technology Thonburi, 2550.
- [8] Vedalou, M.F. and Mekbutr, S., *Design and Build the Continuous Biodiesel Production Process*, Department of Mechanical Engineering, Faculty of Engineering and Industrial Technology, Silpakorn University, 2554.
- [9] Sorndee, J. and Skulpram, P., *Design and Build the Continuous Biodiesel Production Process*, Department of Mechanical Engineering, Faculty of Engineering and Industrial Technology, Silpakorn University, 2555.
- [10] Peng, B.X., Shu, Q., Wang, J.F. and Wang, G.R., *Biodiesel Production from Waste Oil Feedstock by Solid Acid Catalysis*, *Process Safety and Environment Protection*, 2008; 86: 441-447
- [11] Hernandez, D., Astudillo, L., Gutierrez, M., Tenreiro, C., Retamal, C. and Rojas, C. *Biodiesel Production from an Industrial Residue: Alperujo*, *Industrial Crops and Products*, 2013; 52: 495-598.
- [12] Costa, J.F., Almeida, M.F., Alvim-Ferraz, M.C.M. and Dias, J.M., *Biodiesel Production using Oil from Fish Canning Industry Wastes*, *Energy Conversion and Management*, 2013; 74: 17-23.
- [13] Navidi, W. *Tables. Statistics for Engineers and Scientists*, 3rded. New York: McGraw-Hill, 809, 2010.

Heat Transmission of Double-Pane Windows with Horizontal Slats in Thailand

Vichuda Mettanant¹, Pipat Chaiwiwatworakul¹

Received: 12 June 2015; Accepted: 13 July 2015

Abstract

An automated blind can provide energy saving and better comfort. To obtain these benefits a computer program that is able to calculate interior illuminance, heat gain, glare discomfort and thermal comfort has been developed. The thermal performance of the window system was investigated. From the study it is found that installing a venetian blind in between the double-pane glass window causes a significant reduction in heat gain compared to the plain glass window. The heat gain through the window system in the shortwave part of the radiation is analyzed. The slat reflectance, slat angle and solar profile angle are the major affect on the shortwave part of solar heat gain coefficient. The blind using a lower value of slat reflectance has a lower shortwave part of solar heat gain coefficient. The effective solar heat gain coefficient (SHGC) and the effective overall heat transfer coefficient (U) for the double-pane glassed window with enclosed horizontal slats was developed. These SHGC and U value can be used with the equation to calculate the Overall Thermal Transfer Value (OTTV) of Thailand's building energy code to evaluate a building that use the double-pane glassed window with enclosed venetian blind.

Keywords: automated blind, solar heat gain coefficient, overall heat transfer coefficient

Introduction

Venetian blinds are popular shading devices used in commercial buildings. Blinds facilitate daylight into building by blocking excessive light while views are still possible. Utilization of daylight increases worker satisfaction and productivity. For tropical climate or summer conditions daylight is highly available and buildings are cooling load dominated. Daylight can be used to replace electric light; reduce electricity consumption for lighting and cooling system. However heat gain due to solar radiation is an important part of cooling load in Thailand.

Solar Heat Gain Coefficient (SHGC) measures how much heat from the sun is blocked. It is the fraction of incident irradiance that enters through the window and becomes heat gain. It includes both the directly transmitted portion and the absorbed and reemitted portion^{1,2}. The SHGC and the U values are significant factors for rating of fenestration² and also used for building design and rating^{3,4}.

The results of Klems and Warner⁵ confirmed that the SHGC for fenestrations incorporating venetian blinds depends strongly on the incident direction of beam solar radiation. Using a single value of SHGC to characterize window with blind systems would lead to nonsensical energy choices. However, the study was conducted only at few slat angles.

Therefore, in this study an investigation of thermal performance of the window system was evaluated and the effective SHGC and the effective U values were developed and analysis in detail based on weather of Thailand.

Thermal Performance of Venetian Blind Window System

The heat transfer through venetian blind window system can be written as⁶

¹ Joint Graduate School of Energy and Environment, King Mongkut's University of Technology Thonburi, Bangkok, Thailand
E-mail: vichuda.mettanant@gmail.com

$$q = SHGC \times I + U \times \Delta T \tag{1}$$

Where q is the heat gain (W/m^2). SHGC is the solar heat gain coefficient. U is the overall heat transfer coefficient ($W/(m^2 \cdot K)$). ΔT is the temperature difference between the indoor and outdoor condition (K). I is the incident solar radiation (W/m^2). The solar heat gain coefficient for a venetian blind window system can be divided into the solar heat gain coefficient in the shortwave part and the solar heat gain coefficient in the longwave part.

In this analysis the effect of the slat reflectance, slat angle and solar profile angle on the SHGC of the direct solar radiation of the system of glass window and blind are investigated. The solar profile angle is the relationship between the solar altitude angle and the solar azimuth angle. The solar profile angle can be written as

$$\phi_s = \tan^{-1} \left(\frac{\tan(\alpha_s)}{\cos(\gamma_s - \gamma_w)} \right) \tag{2}$$

Where f_s is the solar profile angle. a_s is the solar altitude angle. g_s is the solar azimuth angle. g_w is the window azimuth angle. The solar heat gain coefficient (SHGC) and the solar heat gain coefficient in the shortwave part (ShW SHGC) for the fenestration system are calculated from the developed mathematical model as presented in⁷.

(Figure 1) to 3 show the variations of SHGC for venetian blind at 0° , 45° and -45° , respectively. The SHGC of the single pane clear glass window is also shown for comparison. The results show that the SHGC of the clear glass window and window with venetian blind are dependent on the solar profile angle. The dotted lines in (Figure 1-3) represent the shortwave transmittance for the direct radiation indicated as solar heat gain coefficient in the shortwave part (ShW SHGC). The differences between the solid and dotted lines in (Figure 1 to 3) are the values of longwave transmittance for the direct radiation which are shown as the values of the solar heat gain coefficient in the long wave part.

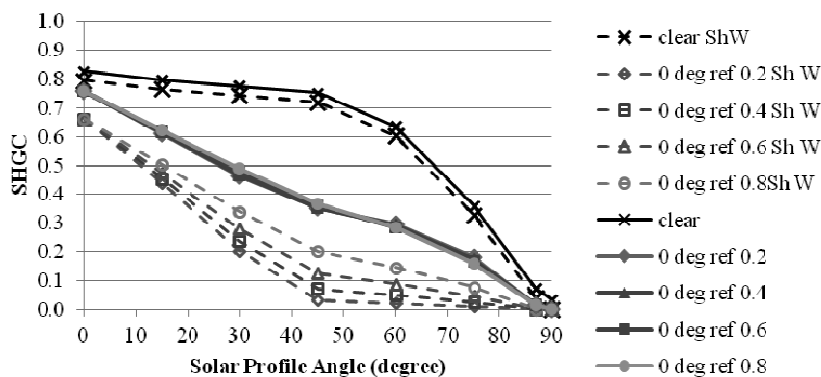


Figure 1 SHGC and ShW SHGC of the window with blind in different slat reflectance when the slat is set at 0° . ref = slat reflectance. Clear = clear glass window.

From the results the SHGC values of clear glass pane are higher than the window with blinds. For single pane clear glass window, the values of solar heat gain coefficient in the shortwave part are dominant and the values of longwave part of SHGC are small when it is compared to the window with blind. The ShW SHGC is high when the slat is in the position that the slats are able

to reflect radiation into the room. In any case, the values of ShW SHGC are low at the low slat reflectance values because the slat can reflect lower ration into the room.

The effect of slat reflectance on SHGC is low when the slat is in position that solar radiation do not incident on the slat or at the slat position that most of the solar radiation is blocked by the slat.

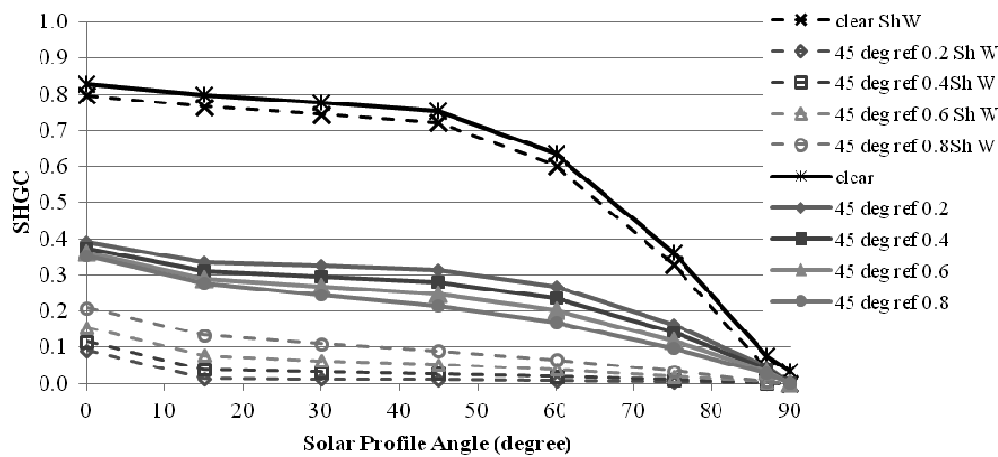


Figure 2 SHGC and ShW SHGC of the window with blind in different slat reflectances when the slat is set at 45°. ref = slat reflectance. Clear = clear glass window.

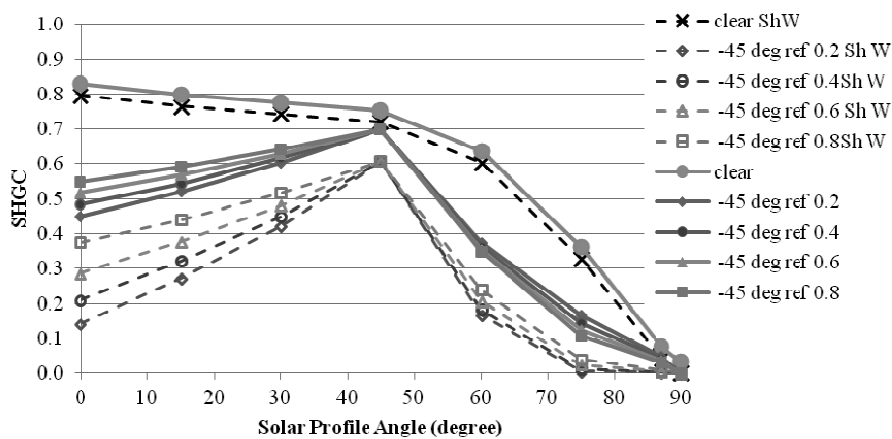


Figure 3 SHGC and ShW SHGC of the window with blind in different slat reflectances when the slat is set at -45°. ref = slat reflectance. Clear = clear glass window.

Effective SHGC and Effective U-value

The one year weather data of Bangkok are used for the simulation. Wind speed is set as 1.5 m/s. The type of window system used in this section is double glazing window filled with air in the gap using green glass as exterior window and clear glass as interior window with venetian blind in between. The properties of glazing are summarized in (Table 1 and 2). For simulation the configuration of the room is as shown in (Figure 4). The walls, roof and ceiling are well insulated.

Thermal properties of glass pane and blind slat are shown in (Table 1). Thermal properties include of thermal conductivity (k), specific heat capacity (c_p), density (r) and thickness. (Table 2) shows properties of glass panes, and blinds including transmittance (t), absorptance (a) and reflectance (r) as solar and visible properties and also emissivity (e). The properties of front and back sides of glasses are the same.

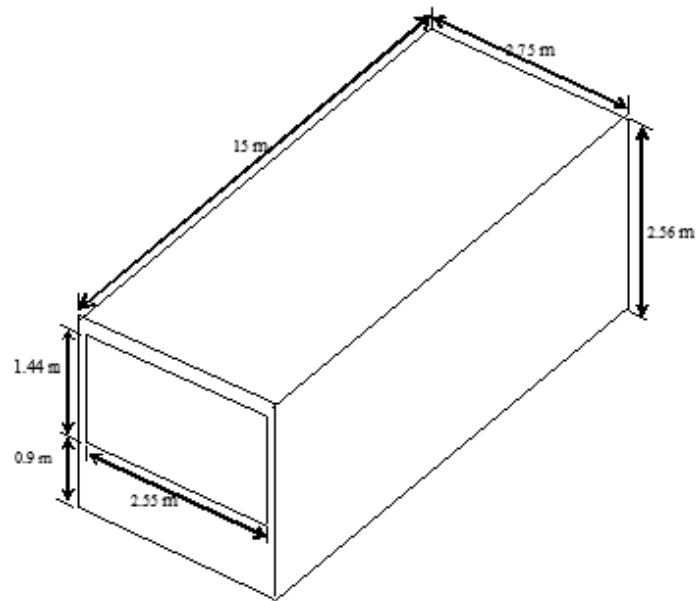


Figure 4 Building configuration

Table 1 Thermal properties of glass panes and blind slat

Material	k W/m.K	c_p kJ/kg.K	ρ kg/m ³	Thickness m
Glass pane	1.05	0.840	2500	0.006
Blind slat	-	0.870	2700	0.001

Table 2 Solar and visible properties of glass panes and blind slat

Section	t	α	ρ	ϵ
Clear glass (solar)	0.80	0.13	0.07	0.85
Clear glass (visible)	0.80	0.12	0.08	-
Green glass (solar)	0.26	0.68	0.06	0.85
Green glass (visible)	0.67	0.21	0.12	-
Blind slat(solar)	0	0.316	0.684	0.316
Blind slat (visible)	0	0.266	0.774	-

The blind chosen for this study is a 50 mm venetian blind. The distance between the between two glass panes is 100 mm. (Figure 5) shows the position of blind when the slat angle is positive with slat tilt angle

b. (Figure 5) also illustrates slat width and distance between each slat (slat separation) which are 0.05 m and 0.042 m, respectively.

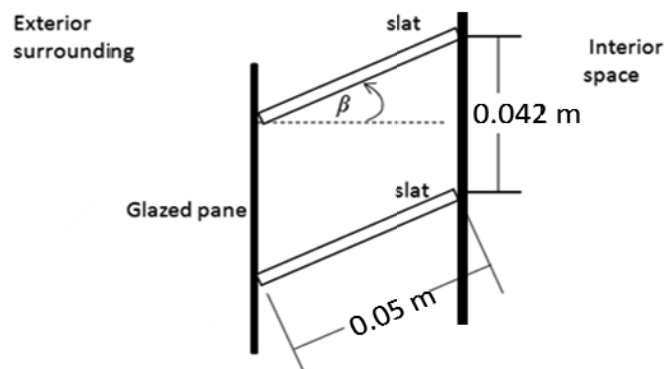


Figure 5 Side view of two adjacent slats

The developed computer program was used to calculate heat transfer through double-pane window with blind. The values of monthly average of the window heat gain are shown in (Figure 6). At high degrees of blind angles such as -50, -60, 50, and 60 degree, heat gain through window reduces because the blind slats are almost close and beam radiation cannot penetrate through

the gaps between blind slats. It is found that there are the higher values of heat gain through the window system in the cases of positive slat angles when comparing to the cases of negative slat angles. When blind angles are negative, there are higher chances that blind slats tilt parallel to the direction of beam solar radiation so higher heat passes through the window system.

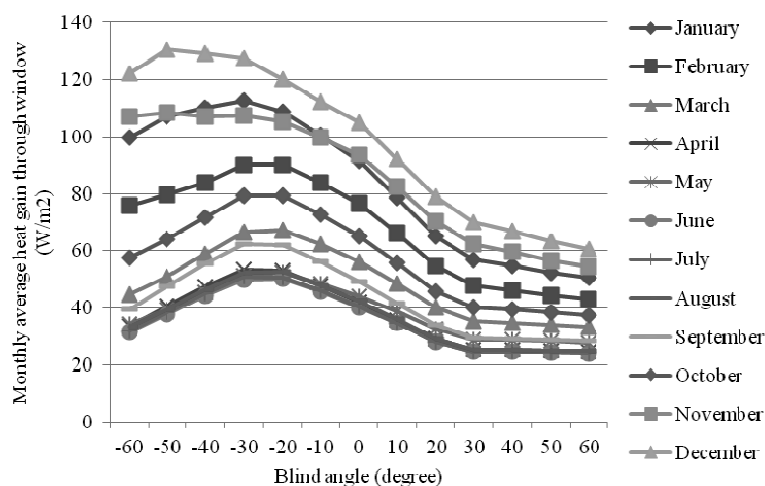


Figure 6 Monthly average heat gain through window (south orientation)

The effective SHGC and U-value are calculated by using Equation 1 divided by the solar radiation incident on window in vertical direction (*I*):

$$\frac{q}{I} = SHGC + U \times \frac{\Delta T}{I} \tag{3}$$

(Figure 7) shows the plot of the ratio between heat gain through window and the solar radiation incident on window in vertical direction and the ratio between the

temperature difference between the indoor and outdoor air and the solar radiation incident on window. Each dot in the graph represents the data at a particular hour. The slope of the data in (Figure 7) is the U-value and the intercept of the graph is the SHGC. One set of data in the case of 0 degree blind angles in October is shown as an example. Each graph provides the SHGC and the U-value for a particular month and a particular slat angle.

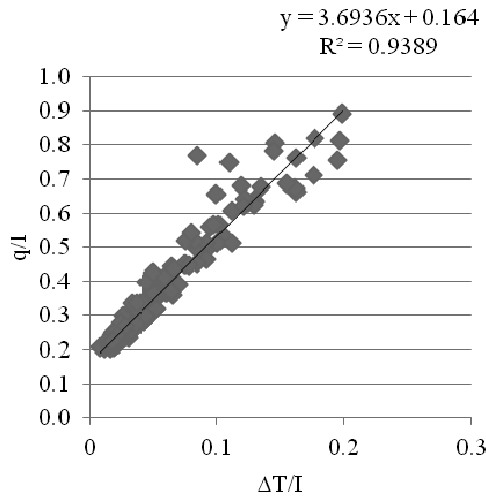


Figure 7 q/l and DT/l in October at 0 degree slat angle

The effective SHGC values and the effective U-value of each month and each blind angle are shown in (Figure 8 and 9), respectively. The results are analyzed for the data during the daytime (8 a.m. to 7 p.m.) and the profile angles are in the range of 22-90 degree. The

yearly average profile angle during daytime is 63 degree. It was found that the results were high when the blind angles were negative which is in agreement with the results shown in (Figure 1 to 3).

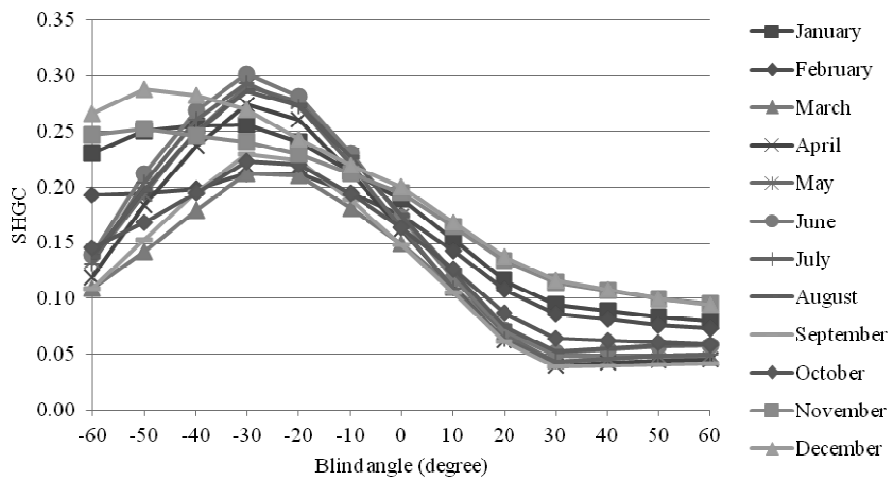


Figure 8 The monthly effective SHGC of the double-pane window with blind

When blind angles are negative, the shortwave part of SHGC is dominant. When blind angles are positive, the longwave part of SHGC is dominant because most of the solar radiation is blocked by the slat.

During the daytime (8 a.m. to 7 p.m.), an average temperature difference between the indoor and outdoor conditions is 7.3 °C when the indoor temperature is set

as 25°C. When slat angles are positive, the effective U-values are highest at 0° blind slat angle and decrease when the blind angle increases. As the blind closes, increasingly it blocks the direct exchange of longwave radiation between the glass panes. This is probably the dominant effect that causes the decrease in U-value as the blind is closed.

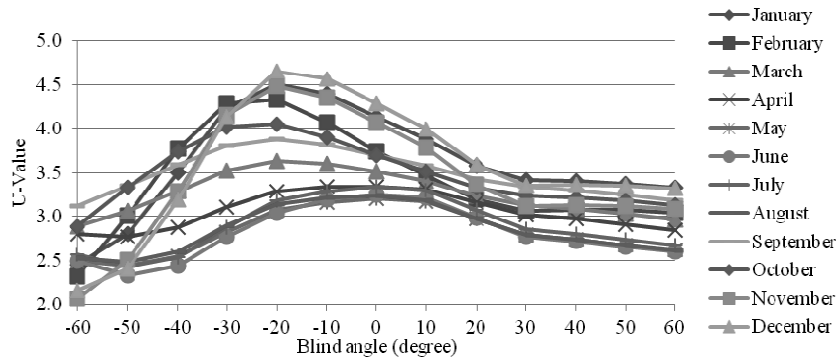


Figure 9 The monthly effective U-value of the double-pane window with blind

Applications of Effective SHGC and U-value

The results of the effective SHGC and the effective U-value in the previous section can be used to calculate the heat gain through window (W/m^2) by Equation 1. The case of January 1st when blind angle is -30° is selected as an example. The effective SHGC and the effective U-value for January are 0.256 and 4.233, respectively. The room air temperature is set as $25^\circ C$. The ambient air temperature and solar radiation incident

on window on the selected day are shown in (Figure 10). The heat transfer through window on the selected day is shown in (Figure 11). The heat transfer through window calculated by the computer program that is based on the heat balance equation, and the radiative exchange equation is also shown in (Figure 11) as a dotted line. The results from Equation 1 show good agreement with the results from the computer simulation program at maximum 7.8% error.

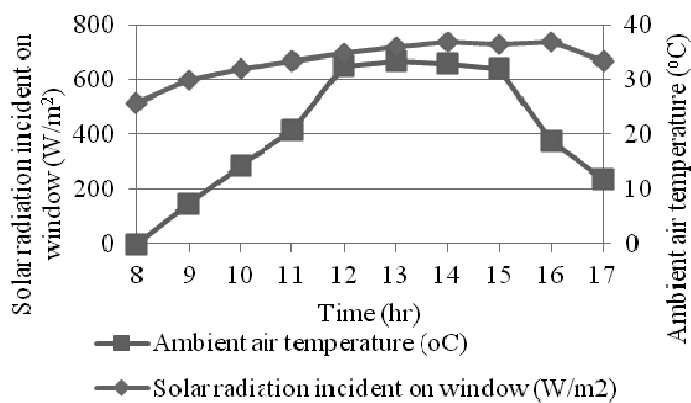


Figure 10 Ambient air temperature and solar radiation incident on window of the example date

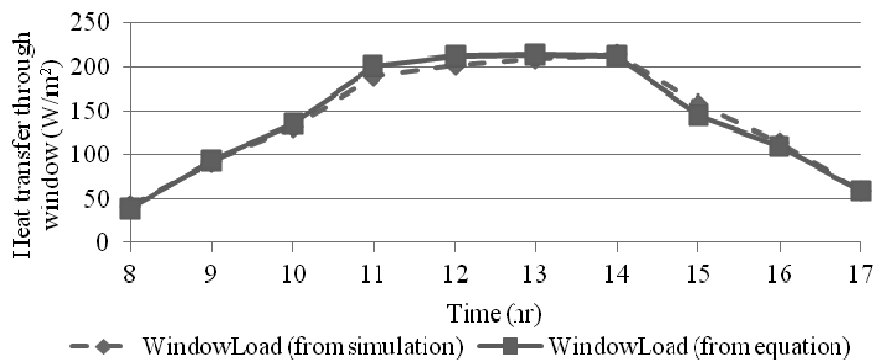


Figure 11 The heat transfer through window on the example date

The effective SHGC and the effective U-value in (Table 3 and 4) can also be used for calculation of the Overall Thermal Transfer Value (OTTV) in the building energy code of Thailand. The terms of the total thermal transmittance (U_f) and the solar heat gain coefficient (SHGC) of the OTTV equation can be calculated when double-pane windows with venetian blind are used.

Conclusion

The SHGC and U-value for calculation of heat transfer through window systems was developed.

The directly transmitted portion of Solar Heat Gain Coefficient (SHGC) and the SHGC that includes the both directly transmitted portion and absorbed and reemitted portion of SHGC were analyzed. The results show that the SHGC are dependent on the solar profile angle and blind reflectance. The monthly effective SHGC values and the monthly effective U-value of white aluminum blind are developed. The heat transfer through window estimated from the developed effective SHGC and effective U-value show well agreement with the heat transfer through window calculated by the computer program that is based on the heat balance equation and the radiative exchange equation at maximum 7.8% error. These SHGC and U value can be used to calculate the Overall Thermal Transfer Value (OTTV) of Thailand's building energy code for a building that use the double-pane glassed window with enclosed venetian blind.

References

- [1] ASHRAE, ASHRAE Handbook Fundamentals, American Society of Heating, Refrigerating and Air-Conditioning Engineers, Inc. Atlanta, Georgia, 2005.
- [2] The National Fenestration Rating Council, Energy Rating, Retrieved from www.nfrc.org, 2015.
- [3] Li, D. H.W., Lam, J. C., Solar heat gain factors and the implications to building designs in subtropical regions, *Energy and Buildings*, 2000; 32(1): 47-55.
- [4] Chirattananon, S. and Taveekun, J, An OTTV-based Energy Estimation Model for Commercial Buildings in Thailand, *Energy and Buildings Journal*, 2004; 26: 680-689.

- [5] Klems, J. H. and Warner, J. L., Solar Heat Gain Coefficient of Complex Fenestrations With a Venetian Blind for Differing Slat Tilt Angles, *ASHRAE Transactions*, 1997; 103(1): 1997.
- [6] Chaiyapinunt, S. and Khamporn, N., Heat transmission through a glass window with acurved venetian blind installed, *Solar Energy*, 2014; 110: 71-82.
- [7] Fathoni, A.M., and Chaiwiwatworakul, P (2011) Double-Pane Window with Internal Fixed-Angle Slats for Daylight Application in the Tropics, Master-degree Thesis, Joint Graduate School of Energy and Environment, King's Monkut University of Technology, Thonburi.

Instruction for Authors

Research manuscripts relevant to subject matters outlined in the objectives are accepted from all institutions and private parties provided they have not been preprinted elsewhere. The context of the papers may be revised as appropriate to the standard. Vol.1 (January-February) Vol.2 (March-April) Vol.3 (May-June) Vol.4 (July-August) Vol.5 (September-October) Vol.6 (November-December)

Preparation of manuscripts:

1. Manuscripts can be written in either Thai or English with the abstract in both Thai and English. Papers should be specific, clear, concise, accurate, and consistent. English language manuscripts should be checked by an English language editor prior to submission.
2. Manuscripts should be typed in MS word ".doc" or ".rtf" (Rich Text) on standard size paper, A4 or 8.5x11 inches, and arranged in two columns: single space for English, double space for Thai language.
3. Browallia font type is required with font size as follows:
 - Title the article: 18 pt. Bold
 - Name(s) of the authors: 16 pt.
 - Main Heading: 16 pt. Bold
 - Sub-heading: 14 pt. Bold
 - Body of the text: 14 pt
 - Footnotes for authors and their affiliations: 12pt.
4. The number of pages to 15, including references, tables, graphs, or pictures.
5. Types of manuscripts accepted: research articles and review articles.
6. Organization of research articles.

Title: denoted in both Thai and English, must be concise and specific to the point, normally less than 100 characters. Name(s) of the author(s) and their affiliation must be given in both Thai and English.

Abstract: This section of the paper should follow an informative style, concisely covering all the important findings in the text. Authors should attempt to restrict the abstract to no more than 250 words.

Keywords: Give at least 4-5 concise words.

The body of the text comprises the following headings:

Introduction: A summary of who is doing what, why where, and when?

Materials and Methods: A discussion of the materials used, and a description clearly detailing how the experiment was undertaken, e.g., experimental design, data collection and analysis, and interpretation.

Results: Present the output. If the information is complicated, add tables, graphs, diagrams etc., as necessary.

Discussion and Conclusion: Discuss how the results are relevant to the objectives or former findings, why? Finally state what recommendations could be drawn.

Tables, figures, diagrams, pictures: should be screened for those important to support the findings, and separated from the text. Captions should be placed above the tables but under the figures.

Acknowledgement: the name of the persons, organization, or funding agencies who helped support the research are acknowledged in this section.

References: listed and referred to in vancouver style.
(<http://www.library.uq.edu.au/training/citation/vancouv.html>)

7. Authors of review articles should follow the typical format style. This includes an introduction, the body of content, conclusion, and references.

Submission of manuscripts

Manuscripts can be submitted to the Editorial Board, Department of Research Support and Development, Mahasarakham University, Khamriang Subdistrict, Kantarawichai District, Maha Sarakham Province, 44150. Tel: 0-43754416 or 0-43754416 ext. 1339. Fax: 0-43754416.
The author should submit the original paper and one copy together with a written disc.

Review of manuscripts:

1. The editorial board will review all manuscripts for format compliance. Manuscripts formatted incorrectly will be returned to the author for correction.
2. Following submission of the corrected manuscript, the Peer Review Committee will review and offer comments
3. Manuscripts receiving the approval of the Peer Review Committee may be returned to the author for revision as advised by the Committee. Manuscripts failing to adopt the Committee's suggestions will not be published.



Membership Application Form

Journal of Science and Technology Mahasarakham University

Date.....

Name (Last).....(First).....

Mailing Address.....

.....

Sub-district..... District.....

Province (City/state)..... Country.....

Postal Code..... E-mail Address.....

Telephone No..... Fax No.....

One-Year membership (400 Baht)

Two Year Membership (800 Baht)

Please send your personal check or money order to the following address:

Mrs.Chaweewan Akkasesthang, Division of Research Supprt and Development, Boromarachakumaree
Building, Khamriang Sub-district, Kantharawichai District, Maha Sarakham Province 00033